

LOW WEAR METAL SLIDING ELECTRICAL CONTACTS

By

NICOLAS ARGIBAY

A DISSERTATION PRESENTED TO THE GRADUATE SCHOOL
OF THE UNIVERSITY OF FLORIDA IN PARTIAL FULFILLMENT
OF THE REQUIREMENTS FOR THE DEGREE OF
DOCTOR OF PHILOSOPHY

UNIVERSITY OF FLORIDA

2011

© 2011 Nicolas Argibay

*Para Alfonso, poeta, consejero, fuente de sabiduría;
Ofa, maestra, artista, compañera de juego;
Tito, generoso, aventurero, pilar de fortaleza;
Blanca, rayo de sol, fuente de alegría,
proveedora de alimento para el cuerpo y el alma;*

Abuelos, amigos, inspiración.

ACKNOWLEDGMENTS

I would like to thank the members of my committee – Prof. W. Gregory Sawyer, Prof. David Hahn, Prof. Scott Banks, and Dr. Gerald Bourne – for their support over the years and for numerous fruitful discussions. I would especially like to thank Prof. Sawyer for providing invaluable advice and a memorable and rewarding graduate research experience. I would also like to thank the members of the University of Florida Tribology Lab, past and present, for many years of friendship and enjoyable collaboration which I can only hope to continue to foster. I owe a special debt of gratitude to Dr. Jason A. Bares, James H. Keith, and Dr. Daniel J. Dickrell, all of whom contributed immensely to this scientific effort.

I would like to thank my parents, Jorge L. Argibay and Maria I. Sencion, whose tremendous support and love over my lifetime is impossible to properly acknowledge in writing, and without whom none of this would have been possible. I would also like to thank my brothers and sister – Federico, Andrew, Andres, and Laura – for their love and support.

Above all, I would like to thank my joy, my inspiration, my partner in life, my best friend, Camila.

TABLE OF CONTENTS

	<u>page</u>
ACKNOWLEDGMENTS	4
LIST OF TABLES	8
LIST OF FIGURES	9
LIST OF ABBREVIATIONS.....	12
ABSTRACT.....	13
CHAPTER	
1 INTRODUCTION	16
Sliding Electrical Contacts and Tribology.....	16
Evolution of Current Collection Technology	17
Design Challenges and Modern Technology: A Return to Metal Brushes?.....	20
2 THEORETICAL AND EXPERIMENTAL BACKGROUND	23
Chapter Summary	23
Extended Summary	23
Contact Area, Contact Resistance, and Wear	28
Contact Area.....	28
Contact Resistance.....	34
Constriction Resistance	35
Film Resistance	39
Wear Regimes	43
Abrasive and Adhesive Wear	44
Wear Rates.....	45
Electrochemical Effects as a Result of Electric Field Strength	50
Cabrera-Mott Oxidation Model.....	50
Polarity, Current Density, and Oxidation Rates for Copper Sliding Electrical Contacts.....	53
Fatigue Strength, Delamination, and Surface Films	57
Contact Stresses and the Mechanism of Delamination	59
Surface Film Thickness and Dislocation Trapping	60
Oxide Films and Fatigue Strength.....	62
Experimental Evidence of Delamination and the Correlation between Oxidation and Wear Rates in High Current Density Copper Sliding Electrical Contacts.....	64
Experimental Investigation with a High Fatigue Strength Copper Alloy	71
End of Chapter Summary and Proposed Research.....	74

3	DESCRIPTION OF EXPERIMENTS.....	77
	Chapter Summary	77
	Microtribometer.....	77
	Summary of Microtribometer Capabilities.....	77
	Applying and Measuring Contact Forces	79
	Prescribed Gas/Liquid Environments.....	81
	In Situ Voltammetry Experiments.....	82
	Electrical Current Transport Experiments.....	84
	Quantifying the Wear Rate of a Toroidal Metal Fiber	85
	Data Acquisition.....	88
	Experimental Setup and Procedures	88
	Sample Preparation: Polishing and Cleaning	88
	Alumina on Copper Sliding Contacts Submerged in Oxidation Dissolving (2M Acetic Acid Solution) and Promoting (3wt% Hydrogen Peroxide) Liquid Mediums	90
	Alumina on Copper Sliding Contacts with In Situ Voltammetry (in 0.1M Sodium Carbonate).....	91
	Sliding Experiments with Sapphire on Single Crystal Copper: Surface Deformation and the Origin of Low Friction and Wear Behavior of Sliding Metal Contacts in the Absence of Oxides/Surface Films.....	93
	Experimental Investigation of the Role of Electrochemically Enhanced Oxidation on the Wear Rate of Copper Sliding Electrical Contacts at High Current Density	94
4	EXPERIMENTAL RESULTS	97
	Chapter Summary	97
	Alumina on Copper Sliding Contacts in Oxidation Enhancing (3wt% Hydrogen Peroxide) and Inhibiting (2M Acetic Acid Solution) Liquid Mediums.....	97
	Summary of Results	97
	Friction Coefficient of Alumina on Copper in 3wt% Hydrogen Peroxide.....	98
	Friction Coefficient of Alumina on Copper in 2M Acetic Acid and 1M Sodium Chloride.....	101
	Alumina on Copper Sliding Contacts with In Situ Voltammetry (in 0.1M Sodium Carbonate).....	101
	Summary of Results	101
	Friction Behavior at Varying Electric Potential	104
	Friction Coefficient and Cyclic Voltammetry	104
	Sliding Experiments with Sapphire on Single Crystal Copper: A Possible Correlation between Surface Grain Refinement and the Low Friction Behavior of Observed for Sliding Metal Contacts in the Absence of Passivating Films	106
	Experimental Investigation of the Role of Electrochemically Enhanced Oxidation on the Wear Rate of Copper Sliding Electrical Contacts at High Current Density	110
	Metal Fiber Wear Rates.....	110
	Friction and Contact Resistance	111

5	DISCUSSIONS.....	114
	Chapter Summary	114
	Interpretation of Measured Data and Remarks	114
	Sliding Experiments with Alumina on Copper	114
	Subsurface Frictional Deformation of the Copper Single Crystal Counterface	116
	Sliding Experiments with a Beryllium Copper Single Fiber on Copper Substrates.....	118
	Electrochemically Enhanced Delamination Wear	120
	Proposed Conceptual Model.....	120
	Regime of Applicability, Limitations, and Implications	123
	Discussions of Interaction Mechanisms and Interfacial Phenomena	123
	Dislocations, Passivation Films, and Cyclic Stresses.....	123
	Low Friction Metal Contacts, Surface Grain Refinement, and the Inverse Hall- Petch Effect.....	126
6	CONCLUSIONS AND REMARKS ON CONTINUING RESEARCH.....	135
APPENDIX		
A	DERIVATION OF AN APPROXIMATE EXPRESSION FOR THE VOLUME OF A TOROIDAL CAP	138
B	GRAIN BOUNDARY SLIDING.....	142
C	DESCRIBING A METAL FIBER SLIDING ELECTRICAL CONTACT AS A PERIODICALLY DISCHARGING CAPACITOR	147
	LIST OF REFERENCES	153
	BIOGRAPHICAL SKETCH	160

LIST OF TABLES

<u>Table</u>	<u>page</u>
3-1 Properties of the Hydrofluoroether Novec™ 7500.....	95
B-1 Values of pre-exponential factor D_0 and activation enthalpy Q for copper self-diffusion through a nanocrystalline volume, a bulk lattice, along a grain boundary, and along a free surface.....	143

LIST OF FIGURES

<u>Figure</u>	<u>page</u>
1-1 Illustration of a simplified unipolar motor, a diagram of the current flow, magnetic field orientation, and torque direction produced by Lorentz force interactions.	17
1-2 Illustration of wind turbine power system components.....	21
2-1 Examples of delamination wear.....	25
2-2 Illustration of the Shen conceptual model describing accelerated fatigue wear.....	26
2-3 Phase contrast micrographs showing deformation of one surface of a nominally flat silver steel interface	30
2-4 Electrical resistance through a circular constriction	35
2-5 Illustration of asperity distributions and the Holm radius	37
2-6 Contact resistance and contact area as a function of asperity geometry	38
2-7 Copper oxidation kinetics	40
2-8 Change in tunneling resistivity as a function of oxide film thickness for various metal-oxide junctions.....	42
2-9 Illustration of abrasive wear.....	43
2-10 Wear and friction map.	49
2-11 Cabrera-Mott oxidation model and electron energy diagram for a metal-oxide junction	51
2-12 Electron energy diagram for a metal-oxide junction and the effect of adsorbed oxygen.....	52
2-13 Illustration of the Cabrera-Mott and modified Cabrera-Mott oxidation model.....	55
2-14 Model of the process of fatigue induced delamination wear	58
2-15 Example of a delamination event on the surface of a solid iron solution	58
2-16 Illustration of subsurface fatigue induced crack propagation due to an asperity contact	59
2-17 Dislocation zone width, friction coefficient, and microrelief height as a function of the oxide film thickness due to sliding on the basal plane of a zinc single crystal.....	61
2-18 Illustration of the Shen-Wood dislocation trapping model.....	63
2-19 Fatigue life data for nickel-based superalloy	64

2-20	Diagram of the major components of a two brush sliding electrical contact tribometer	65
2-21	Experimental data from a multi-fiber copper brush sliding electrical contact.....	66
2-22	Photographs and SEM micrographs illustrating copper brush wear.....	68
2-23	SEM micrograph of wear debris extracted from between the metal fibers of a positive copper fiber brush after a sliding experiment in humid carbon dioxide	70
2-24	SEM micrograph of wear debris from a silver multi-fiber brush sliding experiment on a gold slip-ring	71
2-25	Copper-beryllium UNS C17200 fiber brush.....	72
2-26	Plots of friction coefficient as a function of sliding distance for copper beryllium multi-fiber brushes sliding on an electrical grade copper slip-ring in humidified carbon dioxide with DC current transport	73
2-27	SEM micrographs of worn and unworn copper-beryllium brush fiber tips.....	74
3-1	Photographs of a custom-built environmental microtribometer	79
3-2	Photographs of the double-leaf flexure cantilever assembly	80
3-3	Photographs showing experimental setup and a cross-sectional illustration of the microtribometer configured for friction experiments with in situ voltammetry	83
3-4	Photographs showing the microtribometer configured for sliding experiments with electrical current transport	84
3-5	Illustrations and SWLI images of wear volume measurement for a single metal fiber.....	86
3-6	Photograph of the experimental setup for sapphire on single crystal copper experiments	94
4-1	Friction coefficient data for alumina on copper in 3wt% hydrogen peroxide and 2M acetic acid + 1M NaCl.	98
4-2	Graph of copper oxide film growth kinetics in 1wt% hydrogen peroxide and photographs of copper substrates from experiments in 3wt% hydrogen peroxide	100
4-3	Graph of friction coefficient data for alumina on copper as a function of prescribed oxidation potential (versus SCE)	100
4-4	Plot of friction coefficient as a function of external electrical potential (versus SCE)	105
4-5	Graph of friction coefficient data for sapphire on single crystal copper in HFE.....	107

4-6	SEM micrograph of subsurface friction damage on a single crystal copper substrate sliding against alumina in HFE.....	109
4-7	Graph of wear rate data for experiments using a copper-beryllium fiber sliding on copper in HFE, water, and 3wt% H ₂ O ₂ with and without electrical current transport.....	111
4-8	Graphs of friction coefficient and contact resistance (Ohms) data for experiments using a copper-beryllium fiber sliding on copper in HFE, water, and 3wt% H ₂ O ₂ with and without electrical current transport	112
5-1	Cross-section of a copper single crystal specimen after a single uni-directional pass with a sapphire ball showing subsurface deformation due to frictional sliding	117
5-2	Illustration of a proposed conceptual model describing wear of lightly loaded metal sliding electrical contacts.....	121
5-3	TEM micrographs of fatigued freestanding copper thin film cross-sections.....	124
5-4	Numerical results of principal stress and dislocation distribution for three films of 1 μm thickness consisting of eight grains each, passivated on both sides, passivated on one side, and unpassivated.....	125
5-5	Friction data plots from silicon nitride balls sliding on electrodeposited nickel films at varying load and sliding speed in a nitrogen cover gas	128
5-6	Annular dark-field STEM micrographs showing a sub-surface cross-section of worn nickel substrates from sliding contact experiments	129
5-7	Illustration of a 2D cross-section of a sliding contact showing multi-zone grain recrystallization behavior.....	132
A-1	Geometry of a toroid segment or cap corresponding to the sliding wear geometry observed on the metal fibers	138
B-1	Plots of strain rate accommodation by grain boundary sliding as a function of temperature and grain size at a constant shear stress of 100 MPa.	144
B-2	Plots of the maximum theoretical surface speed that can be accommodated by grain boundary sliding for a 100 MPa surface shear stress.....	145
C-1	Visual representation of a metal fiber sliding electrical contact at increasingly magnified scale	149
C-2	Drift velocity as a function of radial distance from the center of a circular asperity contact area for a contact diameter $2a \sim 1 \mu\text{m}$ and a current of $I \sim 30 \text{ mA}$	150

LIST OF ABBREVIATIONS

FIB	focused ion beam
GBS	grain boundary sliding
HFE	hydrofluoroether
SEM	scanning electron microscope
TEM	transmission electron microscope
XRD	x-ray diffraction

Abstract of Dissertation Presented to the Graduate School
of the University of Florida in Partial Fulfillment of the
Requirements for the Degree of Doctor of Philosophy

LOW WEAR METAL SLIDING ELECTRICAL CONTACTS

By

Nicolas Argibay

August 2011

Chair: Wallace Gregory Sawyer

Major: Mechanical Engineering

The efficiency and performance of modern brushed DC electric motors, generators, and communication slip-rings are typically limited by the tribological behavior of the sliding contacts designed to transport current between the components in relative motion. It is argued that metal fiber brushes may provide unprecedented performance gains, along with complex design challenges, that are the source of ongoing multi-disciplinary research in the search for novel alternatives in current transfer applications.

This work describes an experimental study of copper as a design material for sliding electrical contacts, in the process providing fundamental insight on the mechanisms of wear, friction, and contact resistance governing metal sliding electrical contacts at high current density. A conceptual model correlating wear, electrochemically enhanced oxidation, and dislocation trapping near a passivated sliding surface is described. Perhaps the most remarkable experimental result presented is the demonstration that a beryllium copper fiber sliding on a rotating copper disk immersed in an oxidation inhibiting liquid medium, a hydrofluoroether (HFE), was able to reliably sustain more than 400 A/cm^2 of electrical current transport across a lightly loaded sliding contact while maintaining relatively low wear ($K_{vol} \sim 2 \times 10^{-5} \text{ mm}^3/\text{N-m}$) and friction ($\mu \sim 0.18$). The wear rate was insensitive to current density up to a maximum tested

value of 440 A/cm^2 , corresponding to 50 mA through a $120 \text{ }\mu\text{m}$ diameter fiber cross-section, in contrast with equivalent sliding conditions in an oxidative medium (water) where the system showed current dependent degradation of the tribological and electrical properties. The wear rate of the metal fiber at 400 A/cm^2 operating in an HFE was equivalent to the wear rate without current flow. These results highlight the importance of electrochemically enhanced oxidation at high current density and identified in numerous publications on the subject as a primary challenge in the design of increasingly efficient and inexpensive electrical machinery.

Sliding experiments were performed on copper substrates using alumina as the countersurface material, where a liquid cell used for contact immersion was engineered into a potential controlled three electrode cell for in situ measurement of friction as a response to a prescribed electric field across the copper disk surface. In this way it was possible to decouple current transport from electrochemically enhanced oxidation and to study tribological behavior as a function of oxide composition and rate of formation. Sliding experiments with alumina on copper were also performed in oxidation enhancing electrolytic solutions without the aid of an externally supplied electric field by immersing the sliding contact in 3wt% hydrogen peroxide (oxidation enhancing) and in 2M acetic acid (oxide reducing/dissolving). Three distinct friction regimes were observed. The results of these experiments with copper reveal a high friction response for alumina on copper when the principal reaction byproducts actively forming on the surface are CuO , Cu(OH)_2 , and CuCO_3 of $\mu \sim 0.9$. When the primary species was Cu_2O , the native copper oxide, the friction coefficient was $\mu \sim 0.4$. When sliding in 2M acetic acid, nominally in the absence of a passivating oxide, friction was $\mu \sim 0.2$.

Subsurface sliding damage on unpassivated copper ($\mu \sim 0.2$) was characterized at the completion of a sliding experiment for a sapphire ball sliding on a single crystal copper disk

immersed in an oxidation inhibiting medium. Focused ion beam (FIB) milling was used to mill cross-sections from inside the wear tracks which were extracted and characterized using scanning and transmission electron microscopy. These experiments focused on establishing the role of grain refinement near the surface of a copper disk due to friction damage.

CHAPTER 1 INTRODUCTION

Sliding Electrical Contacts and Tribology

The manipulation of electromagnetic interactions to achieve conversion between electrical and mechanical energy has its origins in the invention of the earliest form of a unipolar motor by Michael Faraday in 1832, known as the Faraday Disc [1]. Ironically, the unipolar motor is not easily described by *Faraday's law of induction* (“*the Faraday paradox*”). The driving mechanism of a unipolar motor is typically described by the closely related *Lorentz force law* given by the simplified expression of Equation 1-1. It states that a charged particle traversing a magnetic field at an angle will experience a force (\mathbf{F}) proportional to the charge magnitude of the particle (q) and the cross-product of charge velocity (\mathbf{v}) and magnetic field (\mathbf{B}) vectors.

$$\bar{F} = q(\bar{v} \times \bar{B}) \quad (1-1)$$

Figure 1-1 depicts a simplified diagram of a unipolar motor and the principles governing its operation. The unipolar motor relies on a direct current (DC) supply to the slip-ring by means of sliding electrical contacts to generate a charge flow. Stationary magnets of various designs are placed along the periphery of the slip-ring so as to generate a magnetic field that will interact with the charge carriers moving through the slip-ring. The layouts of magnets, current flow paths through the slip-ring, and sliding electrical contacts are generally intricate so as to optimize operation and the production of torque while minimizing undesirable effects such as lateral deflection of the current delivery brushes due to Lorentz force interactions.

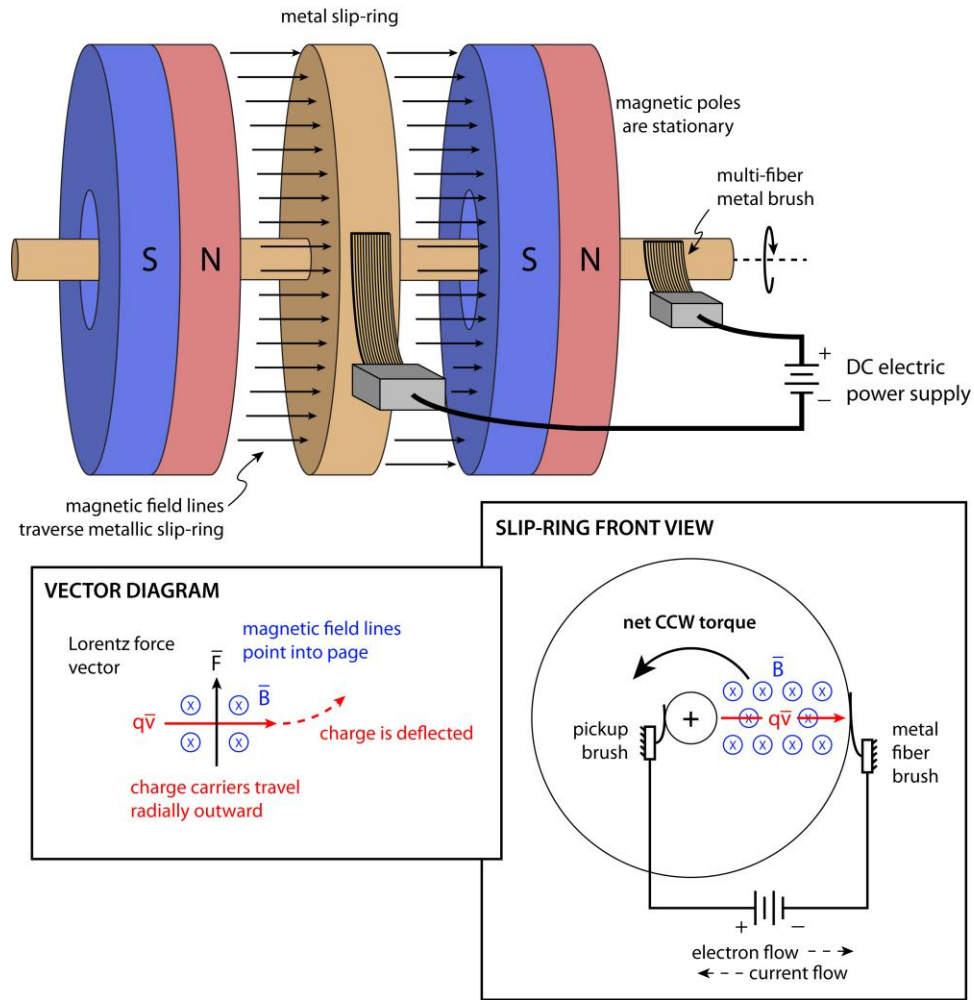


Figure 1-1. Illustration of a simplified unipolar motor, a diagram of the current flow, magnetic field orientation, and torque direction produced by Lorentz force interactions, and a vector diagram of the Lorentz force on a charge carrier traveling through a magnetic field.

Unipolar motor technology achieved limited success in the middle to late 1800s due to the relatively poor tribological performance of metal brush current collection [2]. Although these systems exhibited low electrical resistance, long term operation was not possible due to high friction and wear of the sliding elements.

Evolution of Current Collection Technology

In a 1979 review paper on state of the art current collection technology McNab [3] suggests that construction of metal fiber brushes is one of the primary technical challenges in

designing current collectors capable of long term extreme performance in regard to current density. The term brush as referring to a sliding electrical contact has its origin in some of the first commercial designs of electric motors where current collection was achieved by means of bundled copper fibers resembling painter's brushes [3]. These early designs implementing metal-metal contacts were plagued with high friction, wear, and heat generation due to electrochemical corrosion and arcing. A paradigm shift in current collection technology occurred at the end of the 19th century with the advent of the carbon brush. The use of blocks of carbon as an alternative brush material was first mentioned and patented by George Forbes in 1883, though the first practical use of carbon brushes was pioneered by van Depeole in the late 19th century as a means of current transfer for electric railway systems [4]. Further improvements in carbon brush technology came with the invention of electrographite and metal-graphite composite brushes, both of which are still used today in a host of applications like fuel pumps, wind turbines, electric railways, domestic appliances, etc. The main disadvantages of carbon brushes remain the low system compliance of a monolithic brush and the inherently higher resistance to conduction, in both cases in contrast to multi-fiber metal brushes. Monolithic brushes are limited in the ability to track an inherently rough slip-ring surface, particularly at high speed. Kuhlmann-Wilsdorf estimates that typical graphite brushes sliding on metal slip-rings will exhibit an order of magnitude higher drop in electrical potential compared to metal-metal sliding electrical contacts [2]. However, graphite and metal-graphite brushes provide low wear and friction over a wide range of contact stresses, sliding speeds, and operating environments, making them a suitable and inexpensive choice in many applications. The benefits of metal sliding electrical contacts have not yet justified the system complexity required to maintain such high performance.

It is informative to provide a brief description of the evolution and nature of graphite based lubrication as a motivation for continuing current collection research. The lubricating nature of graphite, first reported by Bragg in 1928 [5], is described by the lamellar structure of the solid form of the material where basal planes of sp^2 bonded carbon atoms form into hexagonal crystal sheets held together by relatively weak van der Waals interactions. The crystalline structure of the carbon sheets renders them thermodynamically stable in many environments and the weak bonding between sheets provides low interfacial shear strength producing low friction coefficients. In the 1940s the critical role of moisture and oxygen in graphite lubrication became apparent with the failure of aircraft actuators at high altitude [6, 7]. Effort was devoted to understanding the role of the environment on the lubricating properties of lamellar lubricants like graphite. In the 1950s, Deacon and Goodman [8] published a theory explaining the observed increase in friction and wear of graphite in the absence of surfactants. They postulated that the edges of graphite lamellae exhibit free (dangling) carbon bonds that in the absence of bond termination by a second species (e.g. water) will result in bonding between adjacent lamellae, inhibiting the low shear stress sliding behavior and exacerbating wear. This mechanism may also explain why graphite tends to transition to a high wear regime at high current density as Ohmic heating of a graphitic brush eventually causes moisture to desorb. As previously mentioned, an additional drawback of monolithic type graphite and metal-graphite brushes is the relatively high stiffness of the brush. Slip-ring runout, surface roughness, and the possibility of vibration are likelier to cause a monolithic brush to lose contact with the slip-ring, if only momentarily, often leading to catastrophic wear events due to arcing. In contrast multi-fiber brushes present a more mechanically compliant alternative with a substantially more stable current transfer behavior, particularly at high sliding speed (10-100 m/s) [2]. The lack of

compliance of monolithic brushes requires the use of high normal loads to ensure an uninterrupted large area of contact between brush and slip-ring, exacerbating wear.

Design Challenges and Modern Technology: A Return to Metal Brushes?

As described in ample detail by authors like Shobert [9] and Holm [10], the same surface films (oxides, moisture, and carbonaceous compounds) responsible for desirable friction and wear behavior of metal systems play a detrimental role in the contact resistance in the form of *film resistance*. As will be shown in the following chapters, one of the defining features of metal sliding electrical contacts is that for all practical purposes the overall system performance of a large scale device will be intimately tied to the few micrometers describing the surfaces of the sliding elements. A fundamental understanding of microscale interactions is crucial to making informed design decisions at the macroscale.

Image Source: Henry & Siegler, Carbone-Lorraine Co. (now Mersen)

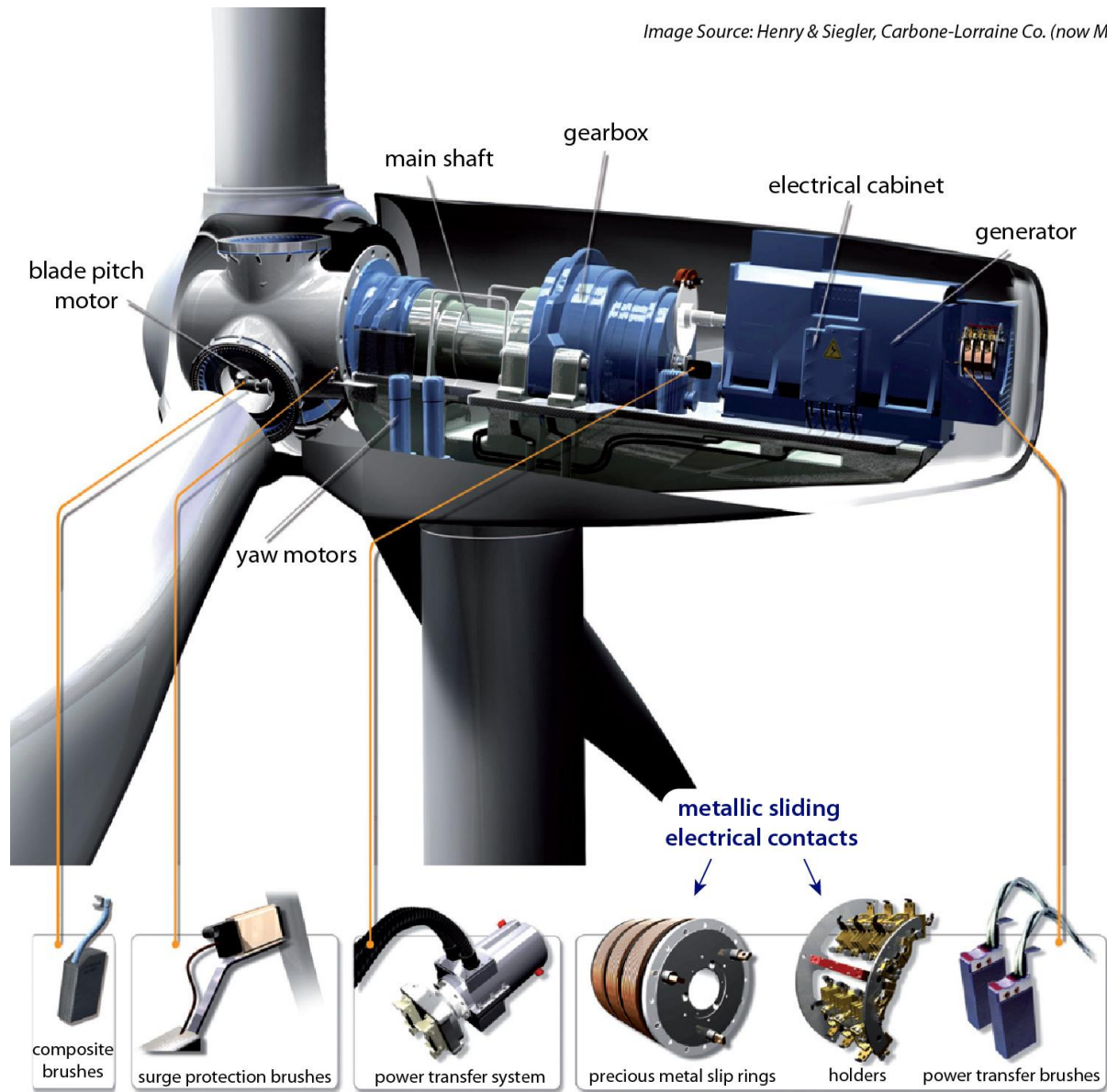


Figure 1-2. Illustration of wind turbine power system components; Photo courtesy of Henry & Siegler of Mersen Corporation, France.

One of the surprising consequences of this research has been the realization that under the right conditions metal sliding electrical contacts are quite robust and capable of sustaining extreme density of current transport with minimal energy loss, in particular, at a small scale. A deep understanding of the fundamental origins of wear of these systems prompted a deviation from long standing engineering criteria when designing current collection devices for electrical

motor applications. It is now apparent that metal sliding electrical contacts should not be relegated to expensive and complex large scale applications, but rather to the drastic reduction in scale of more ordinary applications. With the ability to sustain ten or one-hundred fold greater current density than a carbon brush while maintaining reasonably low wear with relatively inexpensive materials (e.g. copper wire) it is possible to build commutation devices proportionately smaller. An order of magnitude reduction in the size of a rotating commutator or current collector would also enable a reduction in the linear sliding speed of the contact, and consequently the rate of wear. A recently explored example where this research may have substantial impact is in the power generation industry. More specifically, design of wind turbine generators (Figure 1-2).

CHAPTER 2 THEORETICAL AND EXPERIMENTAL BACKGROUND

Chapter Summary

This chapter provides a condensed survey of select topics spanning more than a century of research devoted to understanding the interactions between contacting bodies from the atomistic to the macroscopic level. It is by no means an exhaustive description and is better described as an ambitious summary. The subsections are organized so as to guide the reader in a logical progression to an understanding of the numerous and complex interactions governing the wear and friction of metal sliding electrical contacts. Section 2.1 focuses on the concepts of contact area, contact resistance and wear, and lays the groundwork for the more complex discussions of Sections 2.2 and 2.3 correlating the oxidation and fatigue of metals to wear of metal sliding electrical contacts.

The hypothesis proposed and investigated in this work is that substantial improvements in the wear and current carrying ability of non-noble metal sliding electrical contacts are achievable by ensuring adequate cooling of the contact while inhibiting the formation of surface films and oxides. Given the convoluted and generally broad nature of phenomena described in support of this hypothesis, the first subsection titled *Extended Summary* was included as a type of prologue, and intended as a condensed summary of the summary, though in a more manageable handful of pages.

Extended Summary

Self-mated copper sliding electrical contacts tend to exhibit low friction, wear, and contact resistance when operating in a high humidity carbon dioxide environment [2, 11-14]. Fundamentally, these are lightly loaded non-noble metal contacts sliding in a humid, carbonaceous gas medium with a relatively high voltage potential applied across the sliding

interface to drive the flow of electrical current. At high enough current density the externally applied voltage generates electric fields across surface films and oxides which are great enough to drive electrochemical processes. These factors present a complex electro-tribo-corrosion problem. Recent research has shed insight into the lubricating mechanism of humid carbon dioxide for the case of copper sliding electrical contacts [15, 16]. The water saturated carbon dioxide cover gas provides a slightly acidic, thin film lubricant consisting of adsorbed water and dissolved carbonic acid and other carbonate species. X-ray analysis of the worn-in copper surfaces revealed the presence of copper carbonates and copper oxides on the running surfaces [15, 17]. It is now understood that the formation and presence of copper carbonates plays a role in the low friction and wear characteristics of these systems. However, one observed phenomenon lingered. Above some threshold of current density there is a reported bifurcation in the tribological behavior of metal brushes that is dependent on the direction of current flow; an approximately two-fold higher wear rate is observed for positively biased metal brushes (anodic brush; current travels from brush to slip-ring) [11, 18, 19]. Boyer, Noel, and Chabrerie suggested a mechanism to explain the origin of this phenomenon [11] based on a theoretical model of metal oxidation postulated by Cabrera and Mott [20]. Briefly, when the sliding contact is under a high localized electric field, such as the case of a high current density sliding metal contact, the external electric potential used to drive current across the contact produces large voltage gradients across surface oxides and films and electrochemically inhibits or promotes further oxide growth.

In an unpublished study by Irwin Singer in 2006, wear debris from a series of copper brush/copper slip-ring high current density experiments run in a humid carbon dioxide cover gas

was collected and analyzed using X-ray diffraction. A photograph of the debris is shown in Figure 2-1.

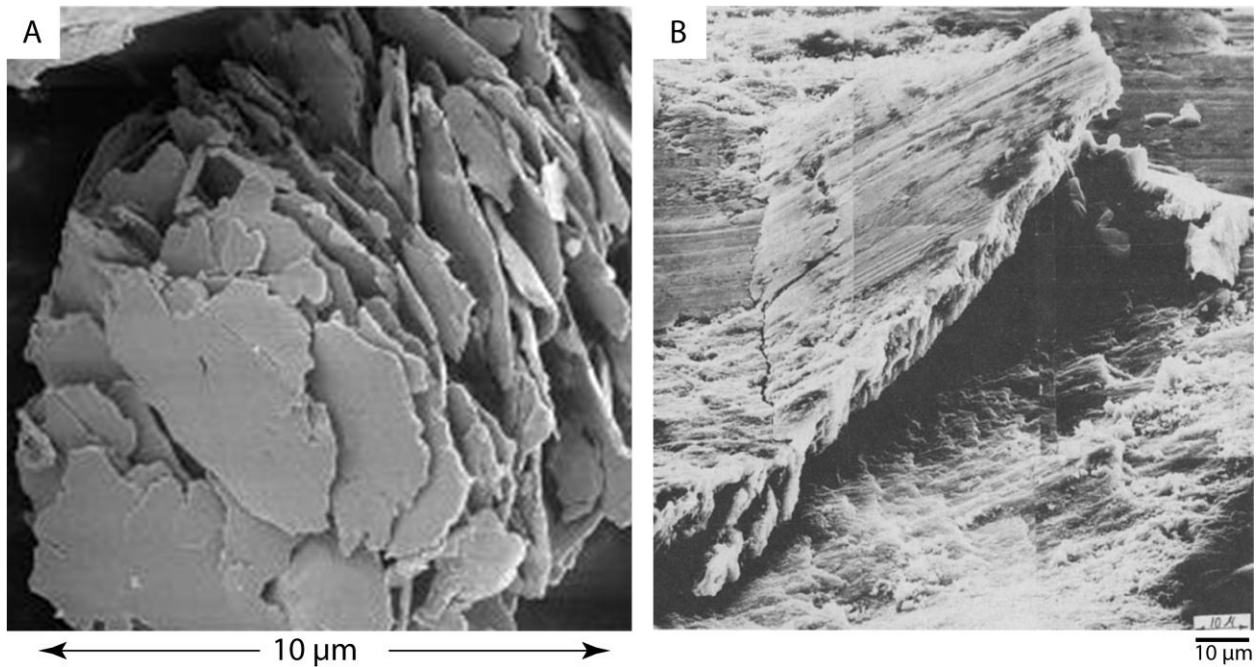


Figure 2-1. Examples of delamination wear. (A) Flake-like wear debris collected from a worn anodic brush after a month long high current density copper brush on copper slip-ring experiment in a humid carbon dioxide environment analyzed using XRD by Irwin L. Singer (Naval Research Lab) and (B) an example of fatigue induced delamination wear debris formation from a 1977 publication by N. P. Suh [21]. Figure 2-1 B was reprinted from *Wear*, Vol. 44, Issue 1, Suh, N. P., *An Overview of the Delamination Theory of Wear*, pp 1-16, © 1977, with permission from Elsevier.

Notably, the wear debris taken from an anodic brush is uniformly flake-like and predominately composed of copper. That is, the debris is not simply comprised of oxide but is due to a bulk material delamination off the surface of the copper brush. The morphology of the debris and the fact that it is mostly bulk metal suggests that the originating wear event was fatigue induced delamination, a phenomenon thoroughly described by Suh, et al. in numerous publications [21-24]. This concept is elaborated in the ensuing sections. Briefly, fatigue induced subsurface cracks are generated near the surface due to friction between the lightly loaded copper brush and the copper slip-ring. Eventually, these localized dislocations tend to coalesce resulting

in the nucleation and propagation of a crack, creating a wear event manifested as the bulk delamination of a flake of metal debris.

There is evidence to suggest a correlation between fatigue induced delamination wear as described by Suh and the inhibition/promotion of oxide growth as described by Cabrera and Mott. The missing link may exist in a mechanism of dislocation formation and trapping under metal oxides and surface films first described in the 1960s by Shen, et al. [25], and the notion that trapped dislocations lead to the formation of voids and cavities by Wood, et al. [26]. Figure 2-2 provides an illustration of the Shen model.

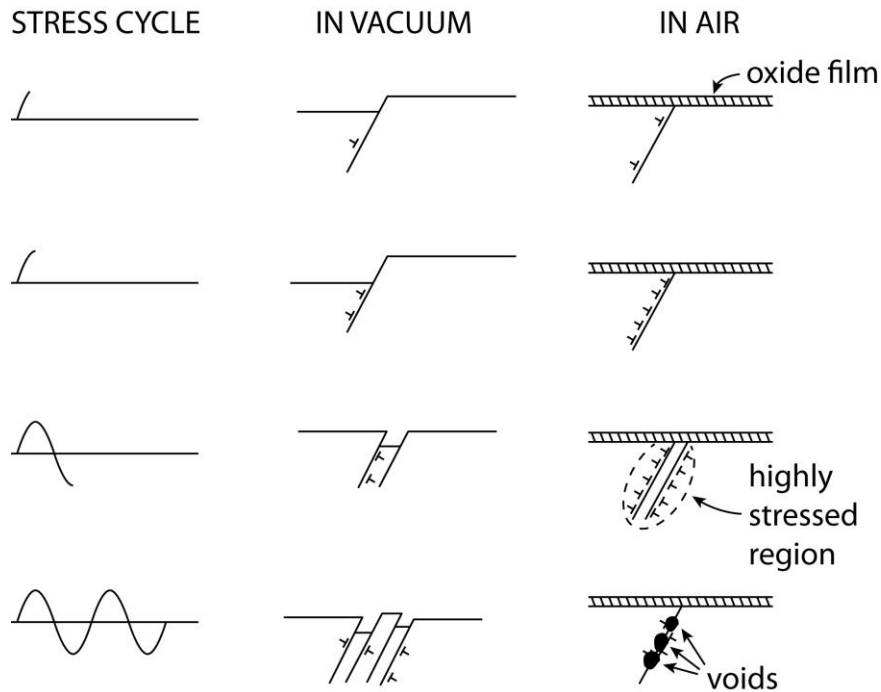


Figure 2-2. Illustration of the Shen conceptual model [25] describing accelerated fatigue wear of non-noble metals in the presence of an oxidizing environment adapted from Duquette [25].

Independent experimental studies published by Nazarenko & Korolenko [27], Duquette [28], and Buckley [29] suggest that the presence of a surface film or oxide results in localized surface hardening and reduced fatigue life of a metal specimen. In one experimental

demonstration Buckley was able to show friction induced fatigue cracks on the surface of a gold specimen with a halide surface film [29]. Nazarenko & Korolenko observed a greater sub-surface dislocation density under zinc single crystals specimens with thicker oxides after friction testing, which they attributed to the trapping of dislocations under the surface oxide [27]. Duquette performed high cycle fatigue testing on single crystal nickel specimens and showed a decreased fatigue life in the presence of an oxidative environment [28]. More recent efforts by Nicola, et al. [30, 31] have provided a mathematical framework describing the effect of surface films on the pile-up of dislocations at the metal-oxide interface of copper single crystal specimens and the localized strength and hardness of the bulk material.

This evidence supports the concept that the wear and contact resistance behavior of metal sliding electrical contacts are intimately tied to the electrochemical effects of oxidative environments and the high electric fields imposed in typical high current density power generation applications. More specifically, high electric fields and oxidative environments lead to promotion or inhibition of oxide and film growth rates on the surface of metal contacts. Consequently, the growth rate of surface films and oxides is correlated to the fatigue life of a sliding metal contact, whereby localized dislocations generated due to friction are trapped more readily at the metal-oxide interface under increasingly thicker films or oxides, leading to accelerated fatigue induced wear events manifested as bulk metal delamination events. Thus, it should be possible to substantially increase the current carrying ability of a non-noble sliding metal contact by controlling the formation rates of oxide and surface films. A possible and exciting consequence of this hypothesis is the potential ability to decouple wear and current density through non-noble metal sliding electrical contacts. This concept was central to the experimental work described in the chapters that follow.

Contact Area, Contact Resistance, and Wear

Contact Area

A fundamental concept in contact mechanics is that for contacting rigid bodies there is a substantial difference between the apparent and actual or real area of contact. This disparity stems from the fact that surfaces, even polished ones, are still imperfect and can be visualized as having microscopic scale roughness, called asperities, superimposed on macroscopic scale waviness. That is, for typical surfaces roughness persists from the macroscopic to the atomistic scale.

It is insightful to preface a description of the real area of contact by providing some historical perspective on the evolution of contact mechanics and the intricacies that arise when observing contact at the smallest scale. Since the early days of contact mechanics, originating with Hertz's 1882 publication [32] describing the elastic deformation of two contacting solid spheres as a function of applied force, the relationship between applied force and contact area between two elastically loaded bodies was assumed to have a proportionality of $A_r \propto F_n^{\frac{2}{3}}$.

Amontons's experimentally derived law of friction, Equation 2-1, states that the friction force is directly proportional to the applied normal force scaled by a constant, the coefficient of friction (μ).

$$\mu = \frac{F_f}{F_n} \quad (2-1)$$

A publication by Adam [33] was perhaps one of the earliest to point out the consequence that, in light of the 2/3 proportionality in normal force and contact area of the Hertzian contact theory for elastically deforming bodies and the linear relationship between friction and normal

force of Amontons's law, the unlikely relationship between friction force and contact area of $F_f \propto A_r^{3/2}$ is implied.

Based on extensive experimental evidence on the contact resistance of mated metal specimens, summarized in his own textbook [10], Holm offered a solution to the controversial argument proposed by Adam suggesting that there was a substantial difference between the real and apparent areas of contact. He suggested that real areas of contact are limited to a few dispersed points of contact which, crucial to overcoming the dilemma, must plastically deform upon contact. That is, even though there may be a nominally elastic contact pressure over the apparent area of contact, the distribution of force is concentrated at a handful of plastically deformed contacting asperities comprising the real area of contact. Extensive work on the mechanics of sliding contacts during the 1950s led to a publication by Archard [34] refuting the validity of the concept that contact between surfaces invariably results in the plastic deformation of asperities. In this publication he provided experimental evidence that, in some instances, lightly loaded metal surfaces in sliding will wear and become smoother, eventually resulting in a great enough real area of contact and load distribution so as to achieve predominately elastic deformation of the asperities in contact. In the same publication Archard also demonstrated the validity of Amontons's law under this assumption, and further proposed that surfaces could be considered as a series of Hertzian type spherical asperities (microscopic roughness) superimposed onto a macroscopic surface waviness. He published a mathematical model [35] following these assumptions where such an idealized rough surface was brought into contact with a nominally flat surface (a rigid half-space), and as the load was increased the asperities in contact would deform elastically in the process bringing more asperities into contact, resulting in a linearly proportional relationship between the applied force and real contact area as predicted

by Amontons's law. Archard's model managed to tie together the observed linear relationship between applied load and contact area for nominally flat contacting bodies. It also provided the insight that at the asperity level plastic deformation will dominate the contact of rough surfaces while elastic contact can be achieved with sufficiently smooth surfaces.

In a 1939 publication on the *Area of Contact between Stationary and Moving Surfaces*, Bowden and Tabor [36] experimentally determined through electrical resistance measurements that the area of contact between two nominally flat metal surfaces was anywhere between 10^2 and 10^5 times smaller than the apparent area, as a function of load. In a 1954 publication by Dyson and Hirst [37], using phase contrast microscopy and varying degrees of contact force between metal balls of 3/16 inch diameter and a metallized glass window, they provided direct observation of the real area of contact between nominally flat bodies (Figure 2-3). They were able to show that contact between nominally flat bodies is relegated to a handful of clustered microscopic contact points. Their work also hinted at the role of macroscopic roughness (waviness) and microscopic roughness on the number and position of clusters and microcontacts.

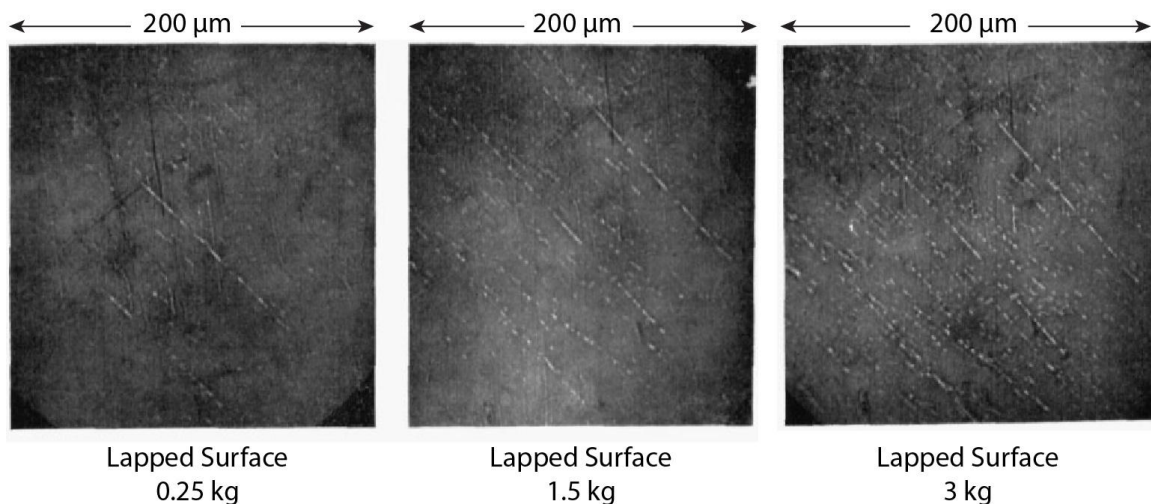


Figure 2-3. Phase contrast micrographs showing deformation of one surface of a nominally flat silver steel interface as a function of the applied load, reproduced from Dyson and Hirst [37]. Figures are reprinted from the Proceedings of the Physical Society

B, Vol. 67, Dyson, J., Hirst, W., *The True Contact Area between Solids*, pp 309-312, © 1954, with permission from IOP Science (DOI: [10.1088/0370-1301/67/4/305](https://doi.org/10.1088/0370-1301/67/4/305)).

Greenwood and Williamson [38] expanded this idea and proposed a refined model of nominally flat contacts where they introduced the use of statistical surface roughness parameters derived from measurements of surface topography as a means of quantifying and predicting the transition from elastic to plastic behavior. In this same publication they also presented experimental evidence that typical surface roughness distributions are Gaussian in nature. Greenwood and Williamson developed an expression for a non-dimensional parameter, which they called the *index of plasticity* (Ψ), correlating the material properties of both surfaces and statistical surface topographical data as a predictor of the boundary of elastic-plastic behavior (Equation 2-2) [38].

$$\Psi = \frac{E'}{H} \sqrt{\frac{\sigma}{\beta}} \quad (2-2)$$

Values of $\Psi < 0.6$ correspond to predominately elastically deformed asperity contacts at all but extremely high contact pressures. Values of $\Psi > 1.0$ indicate that contact will consist of plastically deforming asperities even at negligibly low contact pressures. The range $0.6 < \Psi < 1.0$ corresponds to a transition region where deformation is not clearly predictable, and where the contact pressure applied will have a critical role in the predominance of elastic or plastic deformation behavior. The index of plasticity is a function of the combined elastic modulus of the two bodies (E'), the hardness of the softer of the two surfaces (H), the standard deviation in the relative height distributions of asperities or peaks (σ), and the average radius of curvature of the asperities (β). The combined elastic modulus is shown in Equation 2-3, where the subscripts 1 and 2 refer arbitrarily to the two contacting bodies, and is a function of their elastic modulus (E) and poisson ratio (ν).

$$E' = \left(\frac{1-\nu_1^2}{E_1} + \frac{1-\nu_2^2}{E_2} \right)^{-1} \quad (2-3)$$

Based on the refined contact model proposed by Greenwood and Williamson describing the contact between relatively flat surfaces as a mix of elastic and plastic contacting asperities Holm proposed a simple expression [10] (Equation 2-4) describing the proportionality between applied load and real area of contact as a function of a parameter (ξ).

$$F_n = \xi H A_r \quad (2-4)$$

In this expression the actual load-bearing area (the real area of contact A_r), representing the sum of the asperities in contact, is linearly proportional to the applied normal force and inversely proportional to the corrected hardness of the material (taking into account work hardening) and a constant of proportionality, ξ . The constant of proportionality has a theoretical range of 0 to 1 and is related to the relative smoothness of the contacting surfaces. As two nominally flat surfaces are brought into contact and asperities begin to deform, often plastically, more asperities will come into contact and begin to share the load. The extreme case where $\xi = 1$ refers to the condition that no additional asperities come into contact as the load is increased, and that all the asperities (or single asperity) in contact deform plastically until a sufficiently high enough area is achieved to bear the load. Values of ξ below 1 indicate that as load is increased and the initial asperities begin to deform, more asperities come into contact to share the load, a fraction of them only deforming elastically, causing an overall reduction in the average contact pressure, or an increase in the actual area of contact. Typically, values of ξ are in the range of 0.1 to 0.3 [10] with, for example, values as low as 0.02 reported for extensively polished carbon-carbon contacts. This relatively simple expression is useful in accurately describing experimentally observed trends in many typical metal contacts.

The hardness of a material is effectively a measure of its resistance to flow as a function of an applied normal stress, and takes into account the phenomenon of strain hardening. As described by Holm in [10] (page 374-375) it is insightful to consider the case of Equation 2-4 where $\xi = 1$ and only one asperity is in contact, which is the practical description of a ball indentation on a flat surface at a high enough pressure to achieve plastic deformation. The hardness of a material is then equivalent to the nominal applied pressure. Tabor [39] provides a useful approximation of the hardness (H) as a function of the tensile strength of a material (σ_Y) based on an analysis of stress distributions for a simple ball on flat indentation; $H \sim 3\sigma_Y$ is calculated for the case where work hardening is neglected and $H \sim 4\sigma_Y$ to $5\sigma_Y$ with the inclusion of work hardening.

The following is a summary of fundamental concepts derived from a century of contact mechanics research having significant value in describing and designing metallic sliding electrical contacts.

- 1) The real area of contact for a nominally flat, macroscopic metal contact is a function of material properties, surface roughness, and applied force, and will typically be on the order of 1% of the apparent area of contact.
- 2) The real area of contact of a nominally flat metal contact consists of a number of dispersed asperities in contact, and will vary linearly with the applied force; for single asperity contacts the relationship between force and real area of contact is nonlinear and can be approximated as $A_r \propto F_n^{\frac{2}{3}}$.
- 3) The index of plasticity provides a useful prediction of the deformation regime of contacting asperities, and is a function of material properties and surface topography, not applied force.

- 4) Rough surfaces tend to smoothen in light contact sliding, causing the contact of rough nominally flat surfaces to tend toward an increasing real area of contact and a lower contact pressure; on the other extreme, very smooth surface will tend to roughen with sliding due to the presence of debris.
- 5) Surface films, lubricants, and oxides play a significant role in the reduction of adhesion between sliding metal surfaces by inhibiting bonding

Contact Resistance

Accurate models and predictions of contact resistance are only possible for relatively simple systems, although the general trends and lessons may be scaled to achieve some element of predictability in large scale systems where myriad complexities arise, such as irregular pressure distributions, sliding and friction, evolving topography due to wear, complex and changing oxidation layers, and the presence of solid and liquid lubricant or contaminant films. This section builds on the previous discussion of contact mechanics and contact areas.

As described by Holm [10], the contact resistance (R) across a metal junction is primarily a function of the constriction resistance (R_C) and the film resistance (R_F), Equation 2-5.

$$R = R_C + R_F \quad (\Omega) \quad (2-5)$$

When two electrical conductors are brought into contact and an electrical load is applied, the flow of electric current is constrained at the interface to the real area of contact (asperities), giving rise to what is known as a *constriction resistance*. The *film resistance* is attributed to the presence of electrically insulating oxides and surface films. The film resistance becomes a dominant factor in metallic junctions where relatively thick oxides or contamination films are present.

Constriction Resistance

The contact resistance across a metal interface is intimately tied to the real area of contact. It was in fact the measurement of contact resistance that first hinted at the vast difference in apparent and real area of contact. Bowden and Tabor [36] attribute one of the earliest successful demonstrations highlighting the discrepancy in the contact resistance across metal junctions based on the apparent area of contact to a 1912 publication by Binder [40]. The author showed that the contact resistance was higher than expected if the entire apparent area was indeed in contact.

Timsit [41] provides an in depth overview of the fundamentals of electrical contact resistance that serves as a useful reference for the topics described in this section. A simple model of constriction resistance is illustrated in Figure 2-4 and consists of a single asperity contact between two cylindrical conductors.

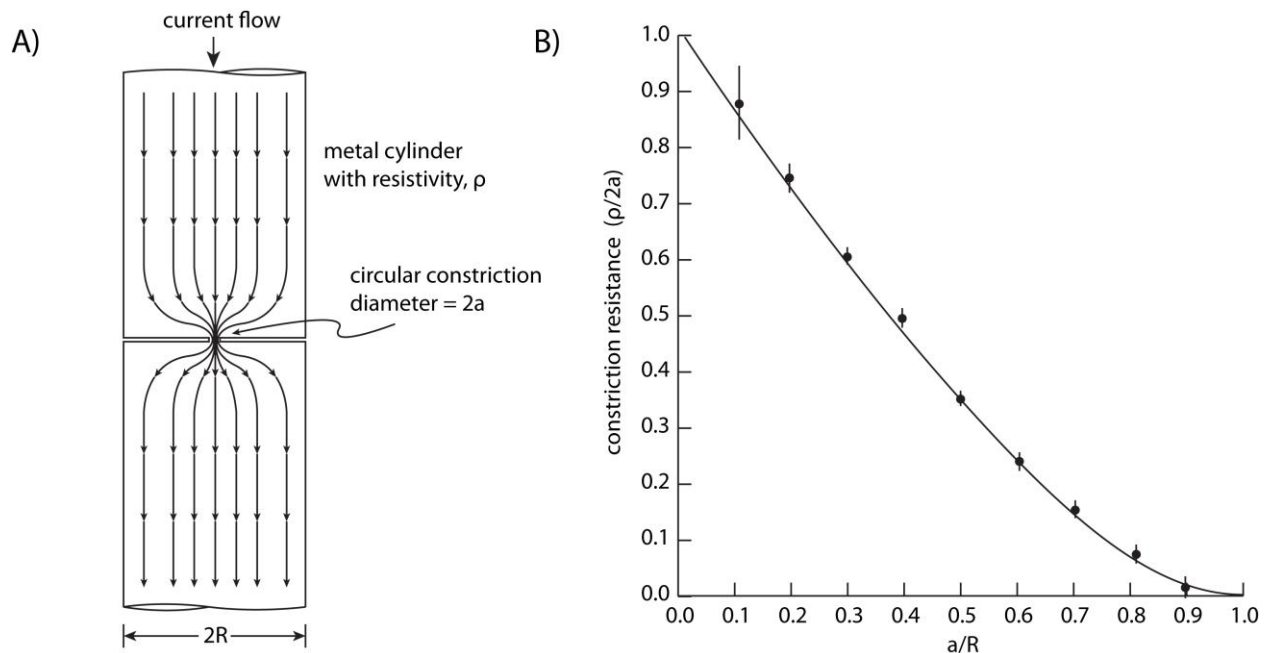


Figure 2-4. Electrical resistance through a circular constriction. (A) Single circular asperity electrical contact between cylindrical conductors and (B) a plot of experimental

data and calculated trend based on a solution to the Laplace equation for the constriction geometry described in (A), adapted from Timsit [41] (pp 3-5).

The case of an isolated circular constriction zone with the assumption that the constriction is much smaller than the conductors (that is, semi-infinite half-spaces in contact at one circular constriction) enables the derivation of a simple and commonly implemented expression for the constriction resistance as a function of the radius of the constriction (a) and the resistivity of the materials in contact (ρ_1 and ρ_2 in units of $\Omega\text{-m}$), Equation 2-6.

$$R_c = \frac{\rho_1 + \rho_2}{4a} \quad (\Omega) \quad (2-6)$$

As an example, for a self-mated copper conductor ($\rho \sim 1.7 \times 10^{-8} \Omega\text{-m}$ [42]), a constriction of 1 μm in radius results in a constriction resistance of 8.8 $\text{m}\Omega$, and a constriction with a 10 μm radius in a resistance of 0.88 $\text{m}\Omega$. In contrast, the resistance of a single 100 μm diameter copper wire 10 mm in length (similar to a single copper fiber implemented in the multi-fiber brushes of [43]) is approximately 20 $\text{m}\Omega$. A 5,000 copper fiber brush (assuming that all fibers are parallel conductors) should have bulk resistance of 4 $\mu\Omega$. Continuing the order of magnitude analysis, assuming that 1/3 of the 5,000 fibers are in contact at any instant of sliding and that one contact point exists per fiber in contact, the average contact spot radius for a brush contact resistance of 0.5 $\text{m}\Omega$, based on Equation 2-5, is $a \sim 10 \text{ nm}$. This analysis neglects the effect of film resistance (copper oxidation and carbonate formation attributed to the humid carbon dioxide environment [15]) and is only intended as a rough order of magnitude approximation of the minimum expected dimension of the asperity contacts in such a system.

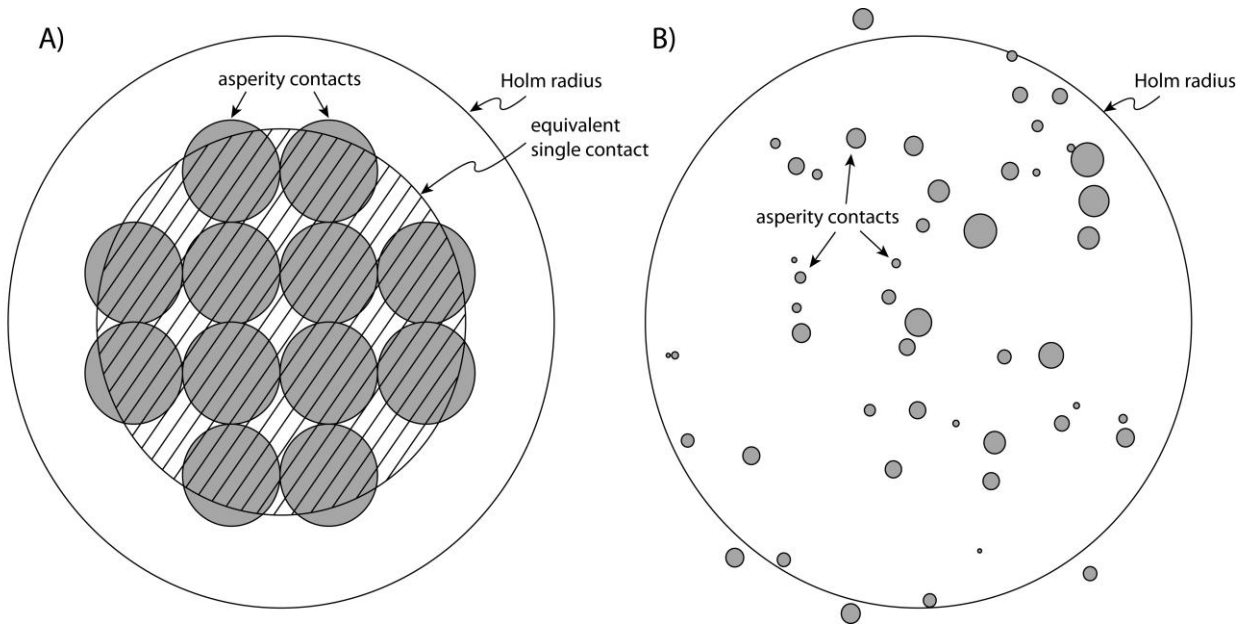


Figure 2-5. Illustration of (A) a uniform distribution of asperities of equal diameter, the equivalent area for a single asperity, and the Holm radius of the cluster; (B) a statistical distribution of asperity contacts and the corresponding Holm radius used to validate the Greenwood-Williamson model for constriction resistance, both figures adapted from Greenwood and Williamson [44].

Holm expanded the model of constriction resistance [10] by analyzing the case of clusters of multiple asperity contacts under the assumption that the asperities are separated by distances much greater than their contact radius. Based on the experimental and theoretical work of Holm [10] and Dyson and Hirst [37], among others, Greenwood and Williamson [44] developed an expression (Equation 2-7) based on classical electrostatics for the constriction resistance of a cluster of statistically distributed asperity contacts of varying diameter, taking into account the proximity of neighboring asperities within the cluster (Figure 2-5).

$$R_c = \rho \left(\frac{1}{2n\bar{a}} + \frac{16}{3\pi^2\alpha} \right) \quad (\Omega) \quad (2-7)$$

In this expression, the constriction resistance (R_c) is a function of the average resistivity of the conductors in contact (ρ), the number of asperities (n), the average asperity radius (\bar{a}), and

the Holm radius (α). The Holm radius, given by Equation 2-8 is a measure of the interaction between neighboring asperities in a cluster.

$$\alpha = \left[\frac{3\pi}{16} \sum \sum \frac{1}{s_{ij}} \right]^{-1} \quad (2-8)$$

In this expression, s_{ij} is the distance between asperity i and j . Greenwood and Williamson further showed [44] that as the separation between asperities in a cluster approaches the average asperity radius ($a \sim s_{ij}$), the expression of Equation 2-7 approaches the value of the simplified expression previously proposed by Holm [45], to account for inter-asperity interactions (Equation 2-9).

$$R_c = \rho \left(\frac{1}{2n\bar{a}} + \frac{1}{2\alpha} \right) \quad (\Omega) \quad (2-9)$$

Based on the distribution of Figure 2-5 B, where they incrementally added more asperity contacts to the model based on a statistical distribution of asperities, Greenwood and Williamson also showed that although there is a relationship between the real area of contact and contact resistance, it is not a predictable and clear trend (Figure 2-6).

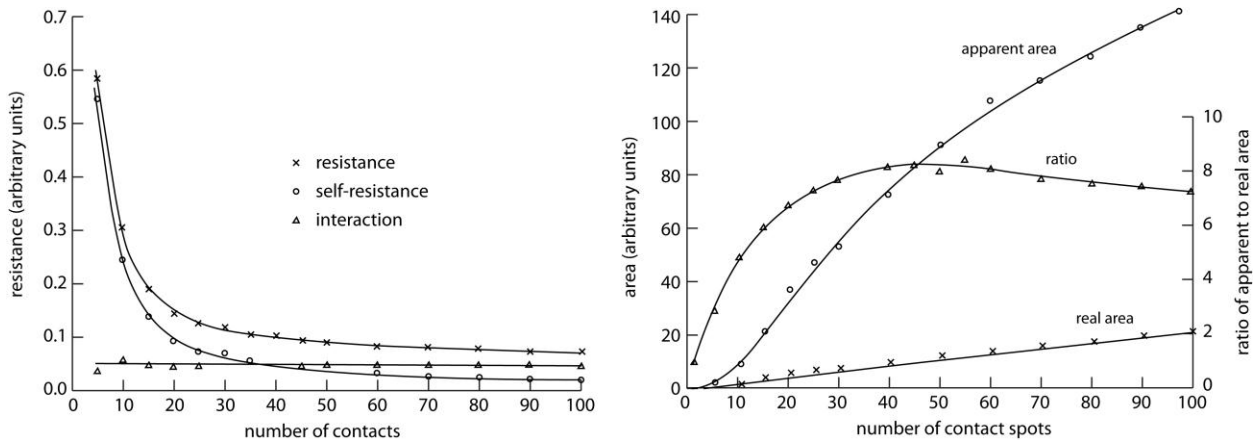


Figure 2-6. Plots of calculated resistance and area as a function of the number of contacting asperities based on the statistical distribution of asperity diameters and relative locations shown in Figure 2-5 B, adapted from Greenwood and Williamson [37].

Film Resistance

The second major source of resistance in typical sliding metal contacts is due to the presence of oxides and surface films. The effect of oxides and films on the contact resistance of macro-scale systems is perhaps the more difficult of the two to model and predict, and is consequently one of the central themes of this thesis. As discussed in the following sections the composition and growth rate of surface films is crucial to the wear, friction, and contact resistance of many sliding metal contact systems, and is intimately related to the electric fields generated at the constrictions previously described, as well as the lubricating environment. Much like the contact pressure and contact resistance depend on the real area of contact, so does the magnitude of electric fields generated with the transport of current. It is arguable that at high enough nominal current density, the electric fields across metal asperity junctions becomes a driving factor in the inhibition or promotion of oxide growth on typical metal conductor materials (covered in Section 2.2).

The bulk resistivity of oxides is generally orders of magnitude greater than that of the metal. For example, for an ideal non-noble metal electrically conductive material like copper, with a bulk resistivity of $\rho \sim 1.7 \times 10^{-8} \text{ } \Omega\text{-m}$ [42], and its more readily formed low temperature oxide Cu_2O (cuprous oxide) has a bulk resistivity of $\rho \sim 5 \times 10^4 \text{ } \Omega\text{-m}$ [46], or 12x orders of magnitude greater. Based on experimental values of contact resistance, this observation hints that conduction is not the primary source of electron transport through typical passivating oxide films. Although copper oxide films are ubiquitous in practice, it is their relatively thin passivation thickness and the phenomenon of electron tunneling that governs the overall contribution to contact resistance of mated copper conductors. A recommended reference for a detailed discussion of electron tunneling through contact films is Holm [10] (section 26). A brief

discussion of the role of electron tunneling through typical metal oxide films on sliding electrical contacts is given in this section.

As postulated by Mott [47] in a seminal 1947 publication, the growth rate of metal oxide films is logarithmic at relatively low temperatures and parabolic at elevated temperatures. Figure 2-7 A shows the rate of copper oxidation at room temperature and 0.01 to 1 Pa of oxygen partial pressure measured using a quartz crystal microbalance (QCM) by Garforth in [47]. As noted by Mott in the same publication, the partial pressure of oxygen has little effect on the oxidation rate above a relatively low threshold. In 1956 Young et al. [48] published extensive experimental data on the oxidation of copper single crystals as a function of crystallographic orientation in a purified oxygen atmosphere obtained at 70°C (Figure 2-7 B).

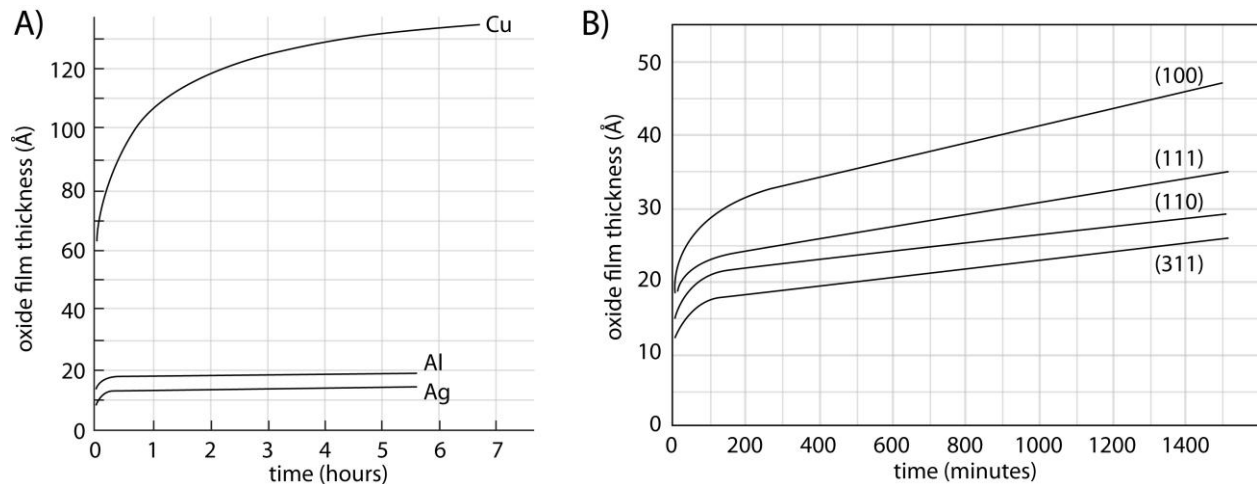


Figure 2-7. Copper oxidation kinetics. (A) Experimental data illustrating logarithmic behavior of oxidation kinetics for copper, aluminum, and silver at room temperature and oxygen partial pressures of 0.01 to 1 Pa measured with a QCM adapted from Garforth [47], and (B) copper oxidation curves for single crystal copper at 70°C adapted from Young et al. [48].

As described in the following section, typical linear wear rates for copper multi-fiber brushes for sliding electrical contacts exhibit wear rates on the order of 10^{-10} m/m, or a loss of one nanometer of fiber brush for every 10 meters of sliding. At typical linear sliding speeds on

the order of 1 m/s this implies a sliding distance of 3.6 km per hour. After one hour of sliding at 10^{-10} m/m the copper fiber brush should have worn 360 nm, or about an order of magnitude more wear than the expected oxidation rate of the copper surface. Given the logarithmic nature of growth rate, this argument merely implies that typical sliding electrical contacts considered in research and power applications tend to operate with oxide thicknesses below about 100 angstroms. Electron microscopy has been used to verify that the passivating oxide thickness on a typical copper fiber brush is below 1 nm.

When two metal asperities with relatively thin oxide films make contact there are two likely paths for electrical conduction. The oxide film may fracture due to contact stress thereby exposing bare metal, or conduction may occur by tunneling through relatively thin films. Tunneling should dominate in lightly loaded sliding electrical contacts. The film resistance or tunneling resistance (σ in units of $\Omega\text{-m}^2$) is a function of several parameters including film thickness, the work function for the metal-oxide-metal junction, and the dielectric constant of the film [10]. Figure 2-8 is adapted from Timsit [41] and shows the variation in tunneling resistance with increasing oxide thickness for various metals, including copper.

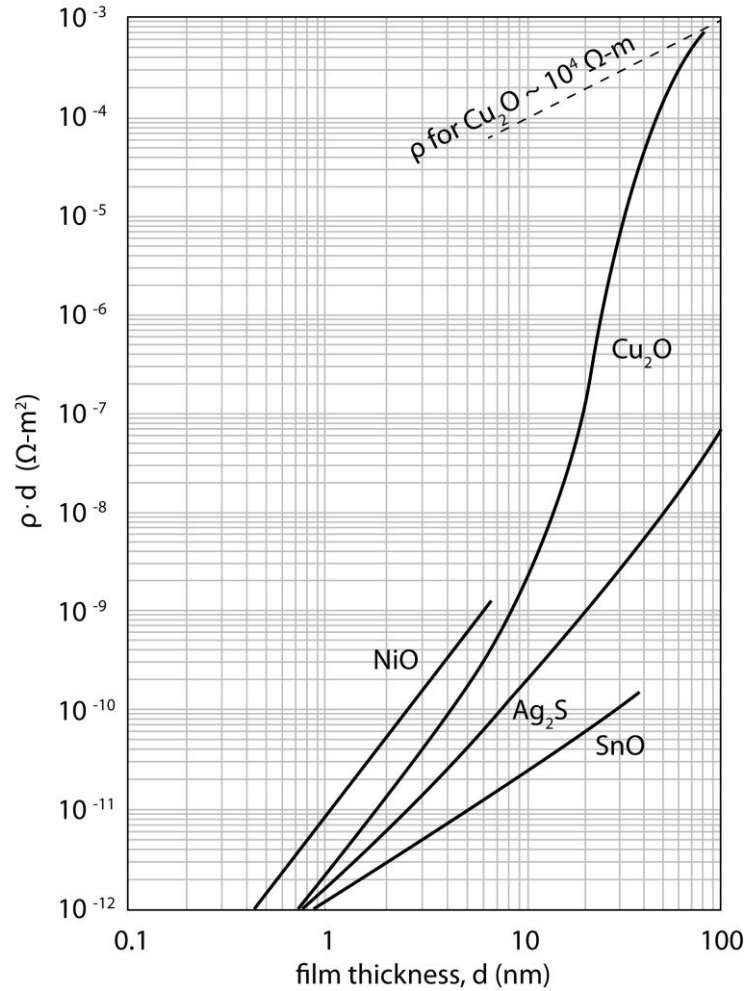


Figure 2-8. Change in tunneling resistivity (σ) as a function of oxide film thickness for various metal-oxide junctions adapted from Timsit [41] (p. 44).

Equation 2-10 from [10] provides an model of the contact resistance through a metal-oxide-metal junction as a function of constriction and film resistances.

$$R_c = \frac{\rho}{2a} + \frac{\sigma}{\pi a^2} \quad (\Omega) \quad (2-10)$$

The contact resistance (R_c) is a function of the bulk metal resistivity (ρ), the tunneling resistivity (σ), and the radius (a) of a circular asperity contact. Then for a copper asperity contact with a radius $a = 1 \mu\text{m}$, assuming a copper resistivity $\rho \sim 1.7 \times 10^{-8} \Omega \cdot \text{m}$ and a uniform 1 nm thick oxide (with a tunneling resistivity $\sigma \sim 2 \times 10^{-12} \Omega \cdot \text{m}^2$ from Figure 2-8), the total

calculated contact resistance is $R_c \sim 0.65 \Omega$. The tunneling resistance contribution to overall contact resistance constitutes approximately 98.7% of the total resistance.

Wear Regimes

As described by Antler [49], wear of a contact may be described not only as the mechanically induced separation of material from a rigid body, but also in some cases as the plastic flow or dimensional change of a body due to a contact event. For example, in the event that material flows due to a contact stress, sometimes fracturing surface films or oxides and exposing bare metal, it may be considered wear. In the absence of a rigorous definition, wear may be generalized as the outcome of a set of well-defined physical processes. For the case of metal-metal sliding electrical contacts the list may be shortened to the processes of abrasion, adhesion, oxidation, and fatigue. There are volumes of text dedicated to the exhaustive description and review of all known wear mechanisms. A recommended textbook is Stachowiak's *Engineering Tribology 3rd Ed.* [50]. The following paragraphs summarize those topics relevant to the ensuing discussion of tribo-electro-corrosion interactions correlating wear and electrochemistry of metal sliding electrical contacts. Fatigue and oxidation wear are treated more in-depth in the last two sections of this chapter.

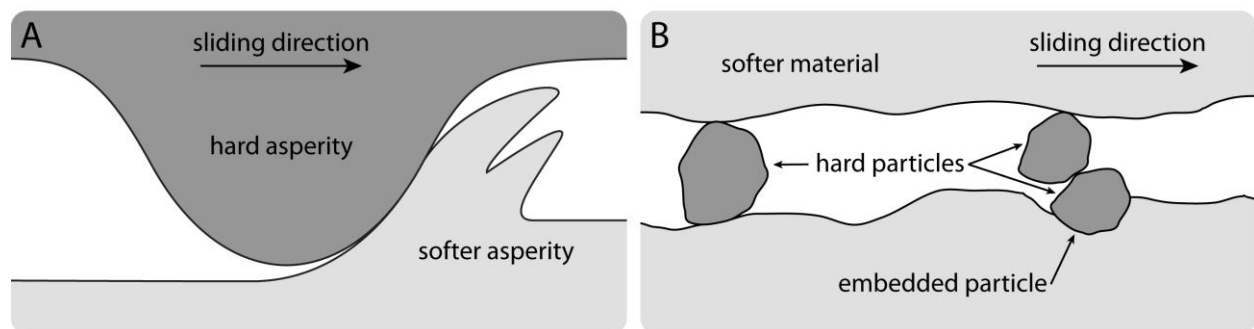


Figure 2-9. Illustration of abrasive wear from a cross-sectional point of view. A) Two-body asperity contact. B) Three-body abrasive wear due to work hardened wear debris or hard foreign bodies. Both figures are adapted from Stachowiak [50].

Abrasive and Adhesive Wear

Abrasive wear occurs when a relatively hard asperity (or particle) comes into contact with a softer asperity or surface, resulting in deformation of the softer material (Figure 2-9). The case of a hard loose particle, commonly occurring from debris generation, is considered third-body abrasion. In sliding, asperities or particles may shear or fracture the more ductile surface, in some instances referred to as ploughing. Third body particles may also embed themselves into softer surfaces rendering them abrasive. The fatigue induced cracking of a surface may sometimes be considered abrasive wear, but it is generally restricted to the case of brittle materials. Fatigue wear of relatively ductile materials is generally treated as a separate mechanism. A notable exception may exist in the abrasion induced fatigue wear of relatively brittle surface oxides, but this should be restricted to fracturing of the oxide rather than a bulk metal delamination event due to fatigue generated sub-surface cracks. Delamination wear is covered in more detail in the section on fatigue and delamination. Abrasion is ubiquitous and inherently unavoidable in sliding metal contacts.

Metal to metal adhesion (or cohesion) may occur at relatively low temperature, resulting from the metallic bonding of contacting asperities. This is typically referred to as “cold welding”. A distinction is made [10] (pages 154-159) for adhesion in sliding between hard metals (e.g. tungsten) and soft metals (e.g. copper), where hard metals have a tendency to cold weld predominately by covalent bonding and soft metals by metallic bonding. Extensive experimental evidence of an inverse trend between hardness (correlated to crystal structure) and the strength of adhesion between various metals was published by Buckley [29]. Holm suggested [10] (page 154) that in sliding the process of covalent bonding is unlikely due to the need for atomic rearrangement to successfully create covalent bonds, leaving metallic bonding as the primary source of cold welding between sliding contacts. An implication of this line of reasoning is that

cold welding will, for example, more likely occur between relatively soft sliding copper contacts than relatively harder sliding tungsten contacts. As described by Antler [49], adhesive wear of sliding metal contacts occurs when the cohesive strength of the bulk material is lower than the adhesive strength at the interface of bonded asperities. The presence of oxides and surface films affects the likelihood of an adhesive event between sliding metal surfaces by introducing a separating layer. As described by Buckley [29], strong adhesion between metals and ceramics (e.g. metal-oxides) may occur where bonding between, for example, a nascent metal surface exposed due to plastic deformation comes into contact with the metal-oxide covered surface of a the second body. Likewise, the presence of oxygen at the interface of two oxidation prone metal surfaces may result in high friction due to bonding across the interface as metal-oxide is formed [51]. In general, however, the presence of an oxide on both metal surfaces serves to minimize adhesive wear as it prevents metal to metal contact or the less likely event of metal to metal-oxide interaction.

Wear Rates

Reported wear rates in sliding electrical contacts publications focusing on fiber metal brush systems will generally only refer to the wear of the brush, neglecting the slip-ring, and appear either as a volume loss or more typically as the dimensionless ratio of change in the brush length over sliding distance (meter/meter) [2, 13, 14, 49, 52, 53]. The justification for neglecting slip-ring wear is that during sliding the coverage of fiber brushes on the slip-ring is only fractional, such that the brushes are always wearing while any given location on the slip-ring surface will only experience wear intermittently. Also, and more pertinent to large scale applications of brushed motors, the brushes are generally less voluminous than the slip-ring such that brush wear sets the life of the motor.

Mass loss is generally considered impractical as a measurement of metal fiber brush wear due to uncertainty in the transfer of material to and from the brush. Similarly, embedding of wear debris between the metal fibers of a multi-fiber brush is a common occurrence, introducing a difficult to predict error in the measurement of brush mass as a measure of wear. The *dimensionless wear rate* (or *linear wear rate*, K_{lin}) of a metal fiber brush is a ratio of the change in length of a brush operating in a steady-state condition (Δh) divided by the linear sliding distance traversed by the brush on the slip-ring (s) (Equation 2-11).

$$K_{lin} = \frac{\Delta h}{s} \quad (\text{m/m}) \quad (2-11)$$

As an example a value of linear brush wear rate of 1×10^{-11} corresponds to a change in brush length of 1 \AA for every 10 m of sliding distance. An immediately obvious consequence of reporting such low wear rates, typical of metal fiber brush sliding electrical contact experiments, is the need for long test durations to achieve a reasonably low error in measurement of brush wear, in particular when taking into consideration the tendency of multi-fiber brushes to splay, conform, and creep. A simple uncertainty evaluation of the linear wear rate is considered in [43] where, assuming negligible error in the measurement of sliding distance over very large distances, the approximation of Equation 2-12 is achieved. The value $u(h)$ corresponds to the uncertainty in measurement of the position of the brush with respect to the slip-ring surface at any instant (in units of length).

$$u(K_{lin}) \cong \frac{\sqrt{2}}{s} u(h) \quad (\text{m/m}) \quad (2-12)$$

A more commonly reported wear rate measurement in Tribology publications is the *specific wear rate* (or *volumetric wear rate*) described by the expression in Equation 2-13 [50] (pages 493-494).

$$K_{vol} = \frac{V_{loss}}{F_n \cdot s} \quad (\text{mm}^3/\text{N-m}) \quad (2-13)$$

The specific wear rate is a ratio of the volume of material removed to the applied normal force multiplied by the sliding distance. The specific wear rate is a variation of the dimensionless *wear coefficient* (K_A), Equation 2-14, proposed by Archard [54]. Archard postulated that the volume of material removed after a given sliding distance, all other things being equal (environment and lubrication), should be linearly proportional to the product of real area of contact and sliding distance. The wear coefficient is also interpreted as the fraction of asperity contacts (or of the real area of contact) that produced a wear event over a given sliding distance.

$$K_A = \frac{V_{loss}}{A_{real} \cdot s} \quad (2-14)$$

As was previously discussed, for macroscopic contacts where the load is distributed over many asperities, the real area of contact is approximately the ratio of applied normal force to material hardness. The expression of Equation 2-14 can then be rewritten as Equation 2-15, correlating the wear coefficient to material hardness, the applied normal force, and the volume loss over a sliding distance.

$$K_A = \frac{H \cdot V_{loss}}{F_n \cdot s} \quad (2-15)$$

For large scale multi-fiber sliding electrical contact experiments, such as described in Section 2.3 and Chapter 3, it is possible to relate the linear wear rate and the specific wear rate (or Archard wear coefficient). The merit in doing so is to provide a means of comparison between typical material wear rates (traditionally reported as specific wear rates) and the wear rates of metal fiber brushes.

For example, the copper multi-fiber brushes used in [43] and discussed in section 2.3 were loaded radially onto the slip-ring (that is, the length of the fibers were oriented orthogonal to the slip-ring surface) with a nominal contact area for the 5,000 fiber brush bundle of about $A_{nom} = 0.5 \text{ cm}^2$, a fiber packing fraction $f = 0.5$, and a nominal contact pressure $p_{nom} = 14 \text{ kPa}$ (0.7 N normal force). Equations 2-16 provide the expressions correlating linear and specific wear rates.

$$K_{vol} = \frac{V_{loss}}{F_n \cdot s} = \frac{(f \cdot A_{nom}) \cdot \Delta h}{F_n \cdot s} = \frac{f \cdot \Delta h}{P_{nom} \cdot s} \quad \text{or} \quad K_{vol} = \frac{f}{P_{nom}} \cdot K_{lin} \quad (2-16)$$

Then, for a reported linear wear rate of $K_{lin} = 7 \times 10^{-11}$ the approximate specific wear rate becomes $K_{vol} \sim 2.5 \times 10^{-6} \text{ mm}^3/\text{N}\cdot\text{m}$. The hardness of the copper fibers was measured using a micro-force hardness tester (CSM Instruments, Switzerland) to be approximately $H \sim 800 \text{ MPa}$. The corresponding Archard wear coefficient is then, after rearranging units, $K_A \sim 2 \times 10^{-6}$.

It is illustrative to conclude the section on wear with a wear and friction map for typical materials compiled by Shobert [55] and adapted to include high performance metal brush sliding electrical contacts by Kuhlmann-Wilsdorf [2] (Figure 2-10). It provides a useful reference to ground the reader on the order of magnitude behaviors required for design of efficient metal sliding electrical contacts.

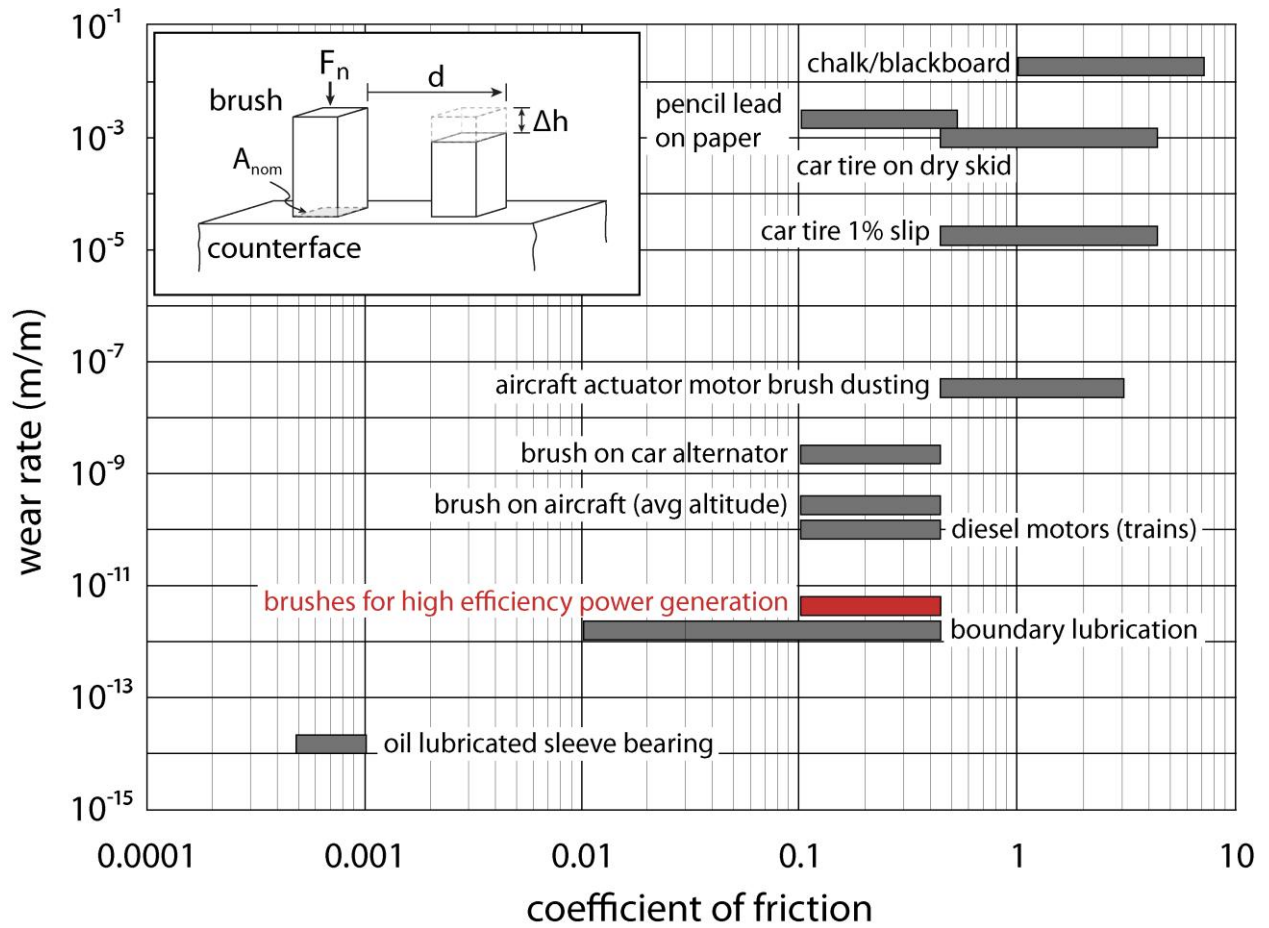


Figure 2-10. Wear and friction map adapted from Shobert [55] and Kuhlmann-Wilsdorf [2] in Slade's [42] Sliding Electrical Contacts textbook.

Electrochemical Effects as a Result of Electric Field Strength

This section is dedicated to the discussion of oxide growth kinetics and the correlation to the electric fields generated at metal-oxide-metal interfaces typical of sliding electrical contacts at high current density. As described by the Cabrera-Mott oxidation model for metals, such as copper, at relatively low temperature the rate of oxidation depends on the chemically induced electric potential across the forming oxide layer originating from the chemisorption of oxygen ions on the surface. The chemical potential will then drive ion and electron diffusion across the oxide film, resulting in the continuous formation of oxide as the M^+ and O^{2-} ions bond. The rate of diffusion decreases as the film thickens, typically obeying a logarithmic trend at low temperatures and a parabolic trend at high temperatures. For copper oxide films the diffusion potential is on the order of 700 millivolts. For metal sliding electrical contacts, like copper multi-fiber brushes sliding on copper slip-rings, there is a threshold depending on the nominal current density, real area of contact, and oxide film thickness at which point the externally applied electric potential across the oxide film driving current transport will achieve a magnitude on the order of the Cabrera-Mott potential. The growth rate of further oxide on the surface of the metal brush is then either enhanced (anodic or positive brushes) or inhibited (cathodic or negative brushes).

Cabrera-Mott Oxidation Model

In a series of seminal publications in the 1940s Mott and Cabrera proposed a general theory describing metal oxide film growth [47, 56]. Based on extensive experimental data, the Cabrera-Mott oxidation theory classifies metal oxidation into different temperature regimes, each with its own dominant physical process. At low temperatures (effectively a function of the melt temperature of a particular metal) the growth rate of an oxide film is a function of the rate of ion diffusion through the growing film, which is a function of the electric field generated by ionic

adsorbates (such as oxygen) on the surface and the bulk metal. The electric field alone, that is, without the aid of temperature, is enough to drive oxide growth obeying a logarithmic rate. The films characteristic of low temperature oxidation typically exhibit a passivation thickness of 20 – 100 Å. At elevated temperatures the role of thermal energy becomes increasingly the dominant factor driving ion diffusion, particularly as films become increasingly thicker, and the rate of growth becomes parabolic. Figure 2-11 illustrates the model proposed by Cabrera-Mott for the case of a copper surface with a cuprous oxide (Cu_2O).

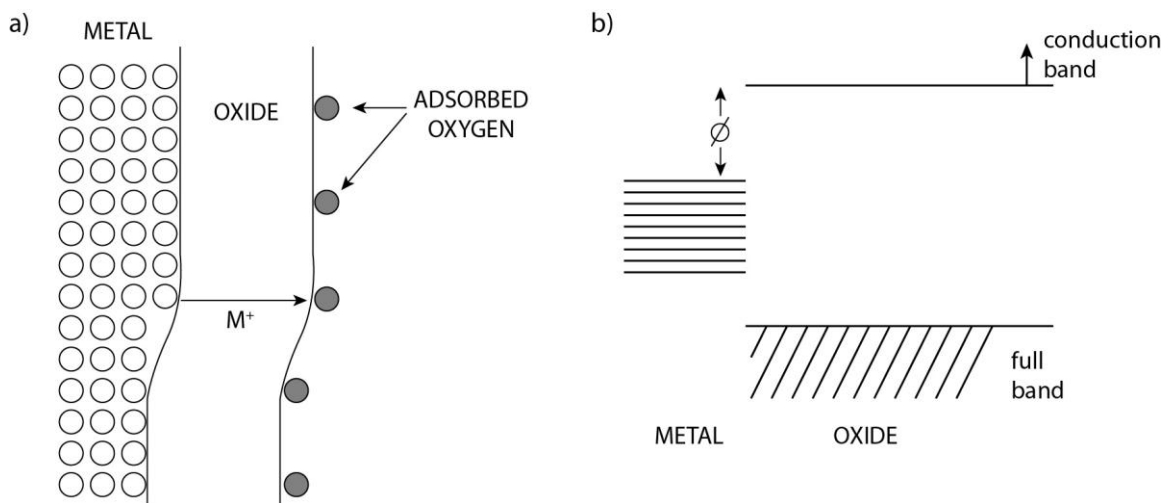


Figure 2-11. Cabrera-Mott oxidation model and electron energy diagram for a metal-oxide junction. (A) Illustration of the Cabrera-Mott oxidation model and (B) the electron energy diagram for a metal-oxide junction illustrating the energy needed to release an electron from the metal conduction band to the oxide conduction band, adapted from Cabrera et al. [56].

Copper and iron oxides are examples of defect semiconductors, where oxygen diffuses into the film and forms vacant cation sites. Based on experimental work on copper oxidation using radioactive tracers, Bardeen [57] showed that it is primarily the copper ions that diffuse toward the gas-oxide interface. The transport of electrons through relatively thin oxides is attributed to tunneling. Figure 2-12 shows the electron energy diagram for a metal-oxide junction with the adsorption of oxygen at the surface, before and after electron diffusion from the

metal-oxide interface to the oxide-gas interface where oxygen ions are converted to ions [56]. It is this process which originates the ion diffusion potential driving oxide growth in an oxygenated environment. The presence of an electrolytic solution with oxide ions will further enhance ion diffusion.

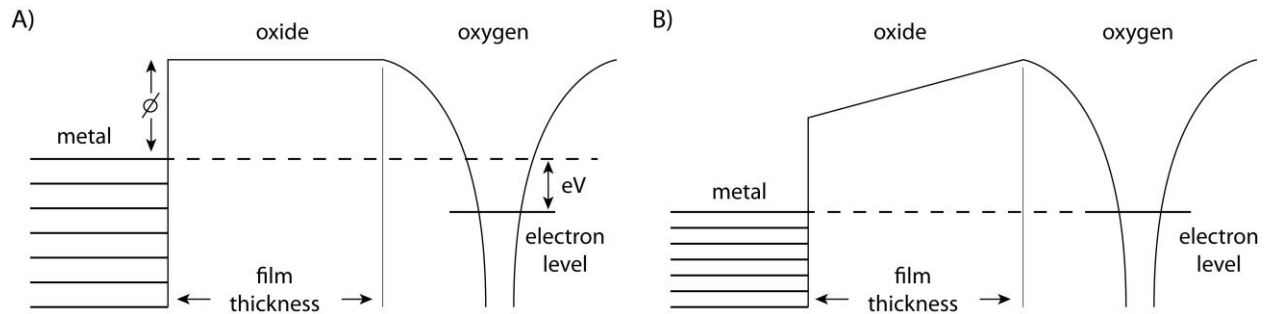


Figure 2-12. Electron energy diagram for a metal-oxide junction and the effect of adsorbed oxygen (A) before and (B) after an electron has moved from the metal to the surface, adapted from Cabrera et al. [56].

Reiterating, the growth rate of thin oxide films is dependent on the diffusion rate of metal ions through the oxide film. Cabrera and Mott derive a relatively simple expression [56] for approximating the formation rate of thin metal oxide films (Equation 2-17) as a function of various physical constants and system properties.

$$\frac{dX}{dt} = av \exp\left(\frac{-W}{kT}\right) \exp\left(\frac{qaF}{2kT}\right) \quad (2-16)$$

The expression relates the rate of change in oxide thickness (dX) with respect to time (dt) as a function of the distance between interstitial positions in the oxide film (a), the charge of a metal ion (q), the Boltzmann constant (k), temperature (T), ion mobility (v in interstitial positions per second), the heat of solution of an ion (W), and the field strength (F in volts/meter). The range of validity for equation 2-16 is for oxide thicknesses $X \leq 10$ -100 nm. The field strength can be written as Equation 2-17.

$$F = \frac{\Delta V}{X} \quad (\text{V/m}) \quad (2-17)$$

The field strength is then a ratio of the ion diffusion driving potential (ΔV) and the oxide film thickness (X). The driving potential may be simply the natural potential originating from oxygen adsorption, or a sum of the natural potential and an *externally applied potential*. It is this electric voltage term that governs the effect of externally applied potentials used to drive current transport across oxide films in sliding electrical contacts. As shown before, the electric potential across a metal contact will depend on the role of film resistance. For increasingly thicker oxides the film resistance will be the dominant component of contact resistance, implying that the voltage drop (and thus electric field) across the oxide film will increase accordingly. Should the externally applied potential across an oxide film approach the order of magnitude of the chemically induced ion diffusion potential, the rate of oxide growth would be inhibited or enhanced depending on the direction of the applied potential (i.e. the direction of current flow through the sliding electrical contact, or the brush polarity).

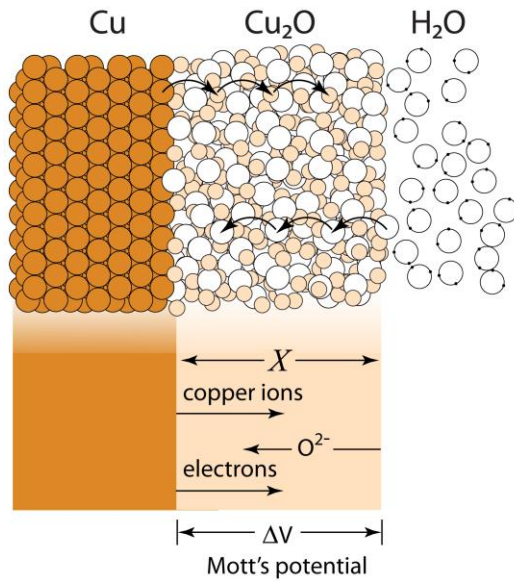
Polarity, Current Density, and Oxidation Rates for Copper Sliding Electrical Contacts

Boyer et al. [11] proposed a modified Cabrera-Mott oxidation model to explain the asymmetry in wear of metallic brush sliding electrical (direct current) contacts at high current density observed by several authors [2, 11, 14, 18, 43, 53]. They correlate their experimental data with copper systems to the work of Cabrera and Mott, in part also with copper, and propose the following analysis based on the assumption that low wear copper sliding electrical contacts in weakly oxidizing environments (e.g. humid nitrogen or even carbon dioxide) exhibit relatively thin oxide films (based on contact resistance measurements) thus validating the use of Cabrera-Mott oxidation theory for thin films. They are able to approximate the voltage drop due to film resistance for their multi-fiber copper brushes. They were using Cu-Cd (99% Cu) fiber brushes

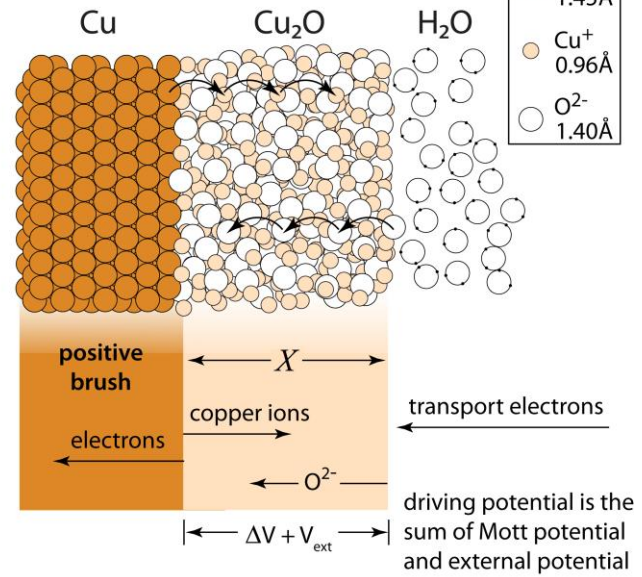
(3,000 fibers of 50 μm diameter, mechanically crimped) radially loaded onto a 15 cm diameter Cu-Cr slip-ring, with approximately 40 A per brush, and a linear sliding speed of 40 m/s.

Using the contact mechanics theory described in the preceding sections they calculate a voltage across the oxide film, accounting for constriction resistance, of $V \sim 50\text{-}100$ mV (+ or – depending on brush polarity). They comment that this is a conservative value as it depends on the assumption that current is evenly distributed through each fiber in the brush. The value of the electric potential across the oxide film is likely higher due, for example, to the probability that not all fibers are in contact with the slip-ring at any given time and variations in contact pressure due to variation in load distribution between fibers, as well as variable oxide film thickness on the moving slip-ring surface. Figure 2-13 illustrates the modified model proposed by Boyer, Noel, and Chabrerie [11].

A) Cabrera-Mott oxidation model



B) modified model (Boyer, Noel, Chabrierie)



activation energy for a metal ion to jump into the oxide

$$\frac{dX}{dt} = av \exp\left(\frac{-W}{kT}\right) \exp\left(\frac{qa\Delta V}{2kTX}\right)$$

rate of oxide formation

in the absence of an externally supplied potential this is the ratio of the limiting film thickness and the current film thickness

an externally supplied potential

$$\frac{dX}{dt} = av \exp\left(\frac{-W}{kT}\right) \exp\left(\frac{qa\Delta V}{2kTX}\right) \exp\left(\frac{qaV_{ext}}{2kTX}\right)$$

$$\left. \frac{dX}{dt} \right|_{\text{positive brush}} > \left. \frac{dX}{dt} \right|_{\text{negative brush}}$$

Figure 2-13. Illustration of the (A) Cabrera-Mott [56] and (B) modified Cabrera-Mott oxidation model proposed by Boyer [11]; the modified model predicts an enhanced rate of oxidation on the positive brush surface and an inhibited oxidation growth rate on the negative brush surface.

An informative example is given by Cabrera and Mott [56] where they suggest that for copper exposed to oxygen at relatively low temperature with relatively thin cuprous oxide films (less than approximately 10 nm thick) the voltage driving ion diffusion should be equal to the Schottky barrier for a Cu-Cu₂O rectifier, or $V \sim 0.7$ V. The modified Cabrera-Mott expression is shown in Equation 2-18.

$$\frac{dX}{dt} = av \exp\left(\frac{-W}{kT}\right) \exp\left(\frac{qa \Delta V}{2kTX}\right) \exp\left(\frac{qaV_{ext}}{2kTX}\right) \quad (2-18)$$

Boyer [11] proposes that the difference in oxide rate of formation between an anodic and cathodic brush may be found by analyzing the ratio of Equation 2-18. For simplicity the case of two identical brush surfaces is considered, including a given initial oxide thickness (X), but where the externally applied voltage ($V_{ext} \sim \pm 50 \text{ mV}$) is positive for one and negative for the other, reducing the ratio expression to Equation 2-19.

$$\frac{\dot{X}_{+brush}}{\dot{X}_{-brush}} = \exp\left[\frac{qa(V_+ - V_-)}{2kTX}\right] \quad \frac{\dot{X}_{+brush}}{\dot{X}_{-brush}} \cong 2x - 20x \quad (2-19)$$

Boyer [11] calculates the ratio to be $\sim 3.8x$, based on values for ion charge $q \sim 1e$, the experimentally derived value $a/2X \sim 0.33$, $kT \sim 0.025 \text{ eV}$ (room temperature), and an externally applied voltage difference of $\sim 100 \text{ mV}$. It is important to note the importance of temperature. Boyer calculates that for a 15°C increase in surface temperature, again for a voltage difference of 100 mV , the ratio grows to $18.5x$. The implication of these calculations is that a substantial difference in the rate of oxide growth may occur if, all things being equal, two brushes with opposing current flow directions are exposed to large electric fields across the film resistance (that is, high enough current density).

Fatigue Strength, Delamination, and Surface Films

The delamination theory of wear was first proposed by Suh in a 1973 publication [58]. In the decade that followed Suh and colleagues expanded the concept by supplying models describing the mechanics of delamination and providing substantial experimental evidence [21-23, 59, 60]. Their model predicts that, in the absence of gross wear between two sliding (or rolling) metal bodies, the more subtle wear mechanism of fatigue driven delamination will dominate. The theory can be summarized as consisting of five progressive steps (paraphrased from Suh [58]):

1. Due to the nature of stress distribution near a region of contact between two metal bodies and the presence of inclusions and other defects within the metal matrix, dislocations will tend to nucleate, prevalently sub-surface, as a result of sliding
2. As sliding continues these dislocations will pile up and lead to the generation of voids at some distance below the surface, again enhanced by defects and inclusions, where the prevalent depth is predictable and dependent on material properties and ultimately sets the thickness of generated wear particles
3. Further sliding will lead to the deformation of voids
4. These voids will eventually coalesce and form a crack parallel to the surface
5. Upon reaching a critical length the crack will propagate and find a path toward the surface, effectively delaminating a section of the body and generating a wear particle; these particles first peel off the surface near the trailing edge of the slider

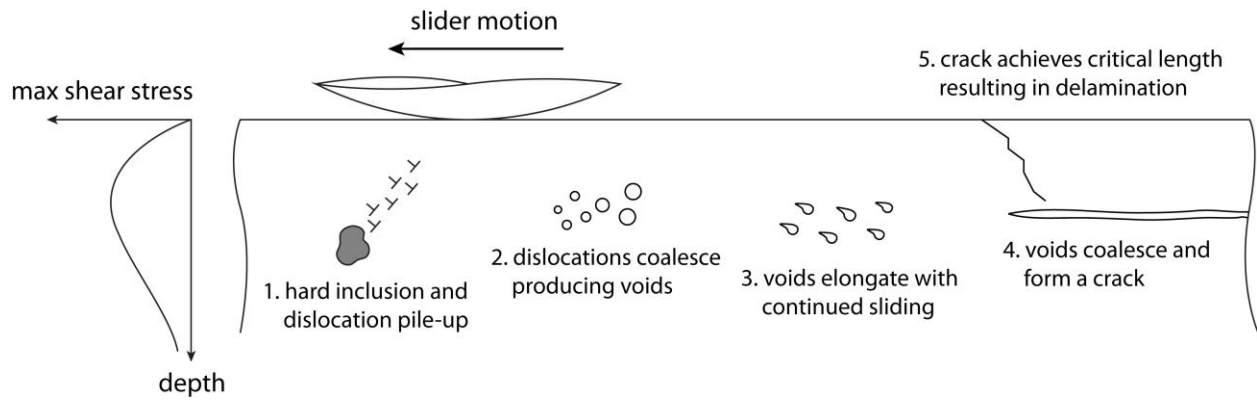


Figure 2-14. Model of the process of fatigue induced delamination wear, adapted from Suh [58] and Stachowiak [50].

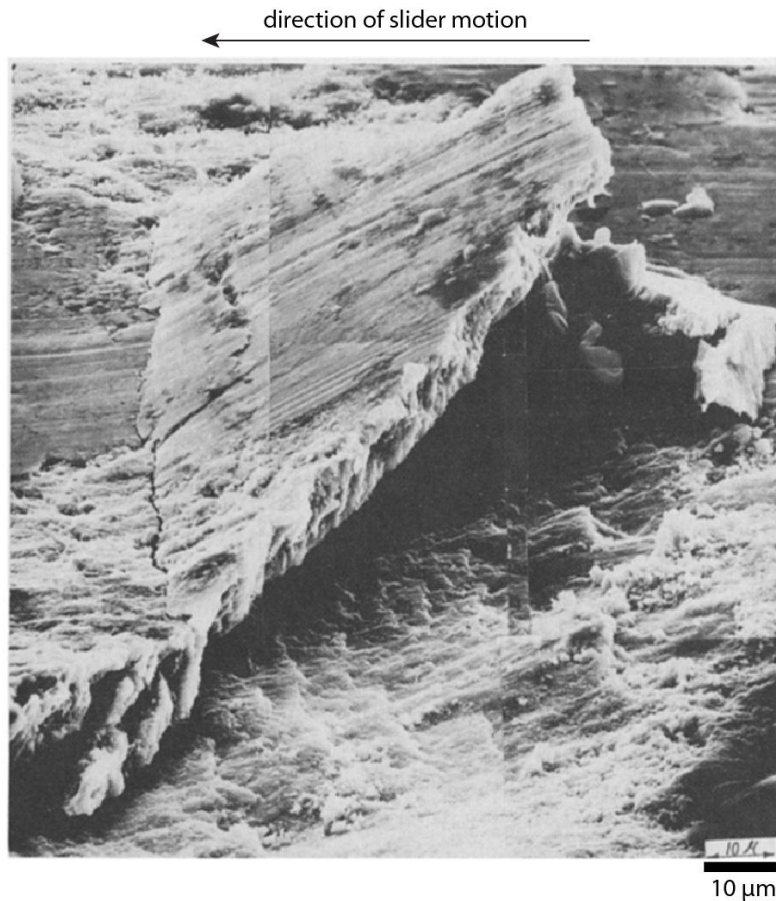


Figure 2-15. Example of a delamination event on the surface of a solid iron solution observed after sliding, reproduced from a 1977 publication by Suh [21]; note that the slider moved from right to left, such that the delaminated particle peels near the trailing edge of the moving slider as it passes. Reprinted from *Wear*, Vol. 44, Issue 1, Suh, N. P., *An Overview of the Delamination Theory of Wear*, pp 1-16, © 1977, with permission from Elsevier.

Contact Stresses and the Mechanism of Delamination

Fluctuation in the localized sub-surface stress distribution of a sliding contact is the driving factor for surface fatigue related wear. As described by Suh [24], the subsurface nucleation and coalescence of dislocations in sliding metal contacts leads to crack formation and propagation, resulting in a delamination wear event. Classical contact mechanics models are insightful in understanding the driving mechanism for this phenomenon. Following the approach of Fleming and Suh [22], and recalling that contact stresses arise from the distribution of applied load over a real area of contact often consisting of tens or hundreds of isolated asperities, the model of Figure 2-16 presents a fair approximation of the local stress distribution near an asperity contact. Figure 2-16 also illustrates a cross-sectional view of how an asperity brought in contact with an elastic half-space may be modeled, to a first approximation and for qualitative purposes, as a point load under the condition of plane strain. This model reveals one of the major consequences of continuously sliding metal contacts: the alternating tensile-compressive stress below the area of contact that is the driving cause of crack propagation leading to fatigue wear.

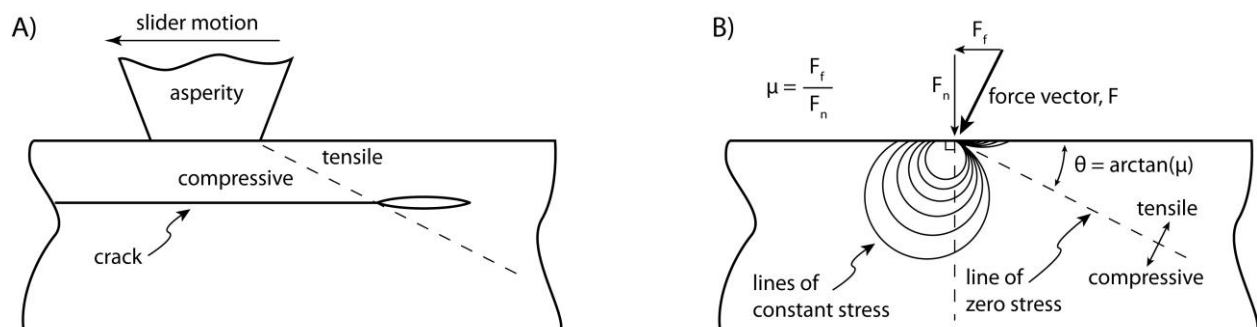


Figure 2-16. Illustration of subsurface fatigue induced crack propagation due to (A) an asperity contact with an elastic half-space and (B) approximate model for a point load with force vector F applied to an elastic half-space, adapted from Fleming and Suh [22]. Vector F represents the combination of a frictional and a normal component of load and μ is the friction coefficient.

More complex contact mechanics models remove the limitation of point loads, modeling instead the cases of distributed loads. These models reveal an additional consequence relevant to the study of fatigue induced wear, and that is that the maximum sub-surface stress generally occurs at some distance below the region of contact, typically at a depth of approximately one-third the contact diameter [61] (pages 202-210, for the case of a cylinder on an elastic half-space with a friction coefficient of 0.2). The presence of a surface shear stress component (due to friction) tends to move the point of maximum stress nearer to the surface and in the direction opposite that of the shear stress. Jahanmir [23] provides a description and model for the process whereby nucleation of dislocations will occur at a predetermined depth (a function of material properties, friction coefficient, and contact pressure) and tend to localize near harder inclusions in the metal matrix. Briefly, for an elliptical stress distribution on an elastic half-space the triaxial state of stress just below a contacting asperity will be highly compressive and tend to close cracks or voids, though at increasing depth there will be a region where the stress field promotes the generation of defects. Coupled with Fleming's work [22] modeling the stress inversion that occurs below the surface as an asperity traverses, the correlation between contact stress and the generation of lamellar wear particles through delamination is achieved.

Surface Film Thickness and Dislocation Trapping

Experimental evidence was published by Nazarenko and Korolenko [62] revealing a correlation between the thickness of a surface film or oxide layer on a metal friction surface and the density of dislocations observed in the matrix in the vicinity of the film. They postulate that progressively thicker films or oxides on the surface of metal crystals experiencing cyclic stress due to friction will inhibit the ability of dislocations to relieve themselves at the surface (or at the metal-oxide interface) resulting in a relative increase in dislocation density near the interface of

the metal and oxide or film. In summary, thicker metal-oxides will cause dislocation trapping near the friction surface.

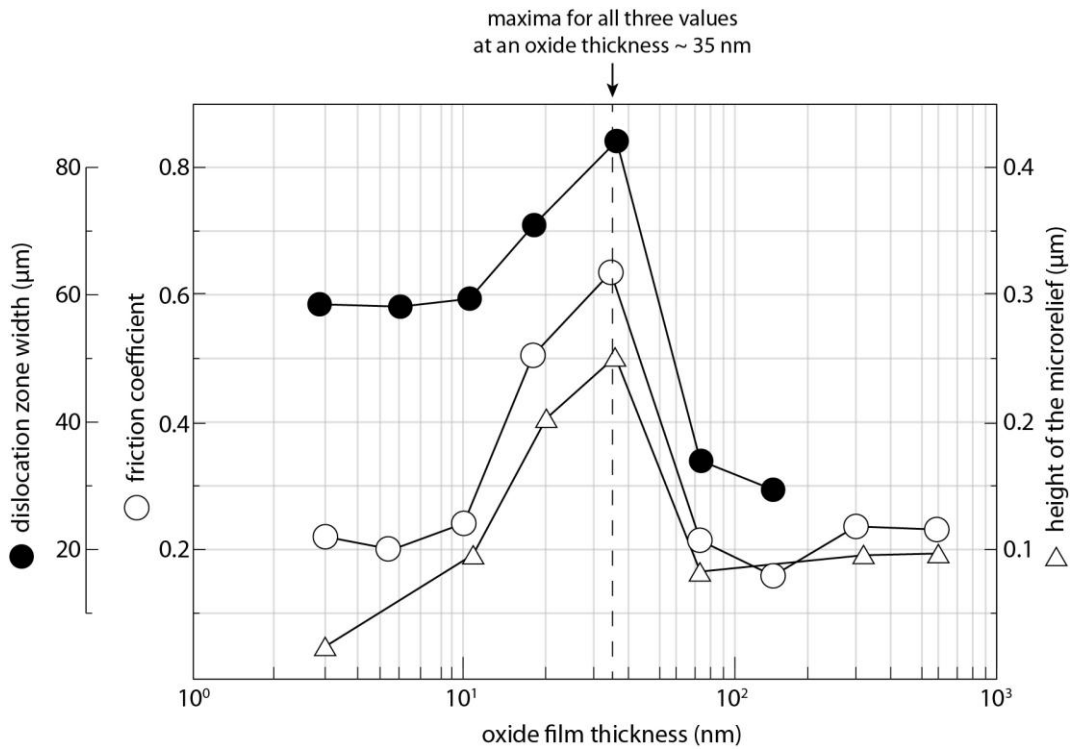


Figure 2-17. Dislocation zone width, friction coefficient, and microrelief height as a function of the oxide film thickness due to sliding on the basal plane of a zinc single crystal with a 700 μm diameter spherical steel indenter at 30 grams of applied load, taken from Nazarenko and Korolenko [62] (Figure 1).

Their friction experiments consisted of a spherical steel indenter sliding on the basal plane of a zinc single crystal, upon which an oxide (ZnO) was grown to a varying degree of thickness prior to each test. At the conclusion of each test the density of dislocations was exposed by chemical etching and observed via optical microscopy. They report the formation of relatively large microscopic steps on the surface of specimens with thicker oxide layers, also observing that the density of dislocations under the oxide was notably higher compared to specimens with a thinner oxide layer. That is, the presence of increasingly thicker oxide films inhibited the formation of dislocations at the surface of the zinc crystal and increased the

dislocation density under the oxide film after a period of sliding. The microsteps were attributed to slip bands which serve as a means of relieving dislocations at the surface of the crystal. They observed that with an increasingly thicker oxide layer the number of slip bands is reduced though the step heights are increased. The trend of increasing dislocation trapping, friction coefficient, and microrelief height as a function of increasing oxide layer thickness reaches a maximum at a thickness of approximately 35 nm. Nazarenko and Korolenko attribute the region of high friction to the markedly greater height of surface microreliefs at a critical oxide thickness of about 35 nm, after which the height of microreliefs decreases, resulting in a smoother surface topography and consequently lower friction coefficient values.

Oxide Films and Fatigue Strength

In 1966, half a decade before the work of Nazarenko and Korolenko [62], Shen, Podlaseck, and Kramer [25] postulated a mechanism of dislocation trapping to explain experimental evidence of an observed reduction in fatigue strength with the presence of an oxide on aluminum specimens (Figure 2-18). The experiments were performed on aluminum 1100 specimens in a partial vacuum, with partial pressures of oxygen in the range 3×10^{-2} to 1×10^{-2} torr. They found that the decrease in fatigue strength was not sensitive to variation in partial pressure of oxygen, a previously suggested origin of the observed phenomenon.

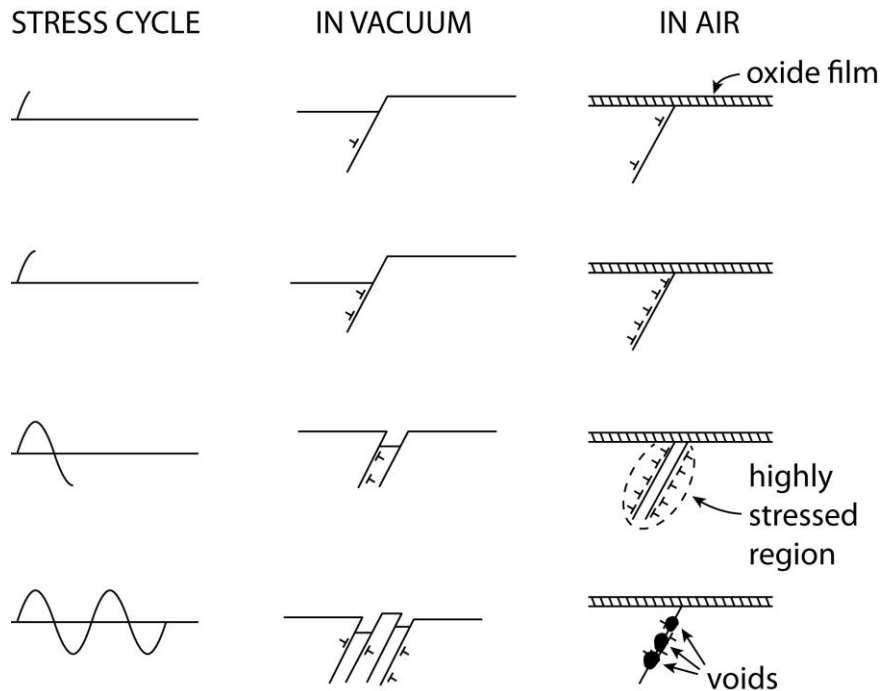


Figure 2-18. Illustration of the conceptual model proposed by Shen [25] to explain the observed reduction in fatigue strength of aluminum specimens with increasingly thicker oxides due to dislocation trapping and pile-up leading to void nucleation and an increase in crack propagation rate adapted from Duquette [25].

Shen's model was influenced by the work of Wood, Cousland, and Sargent [26] where they suggested that the formation of cavities and voids was the source of fatigue crack growth. Shen's model ties the concepts of dislocation trapping due to increasingly thicker oxide films to the increased void formation and crack propagation rates.

Experimental evidence from Duquette [28] supports the model proposed by Shen. Duquette performed high cycle fatigue experiments on single crystal nickel-based superalloys in vacuum and in laboratory air (Figure 2-19), also in dry and humidified laboratory air, where he observed a marked decrease in fatigue life for specimens exposed to oxidative environments.

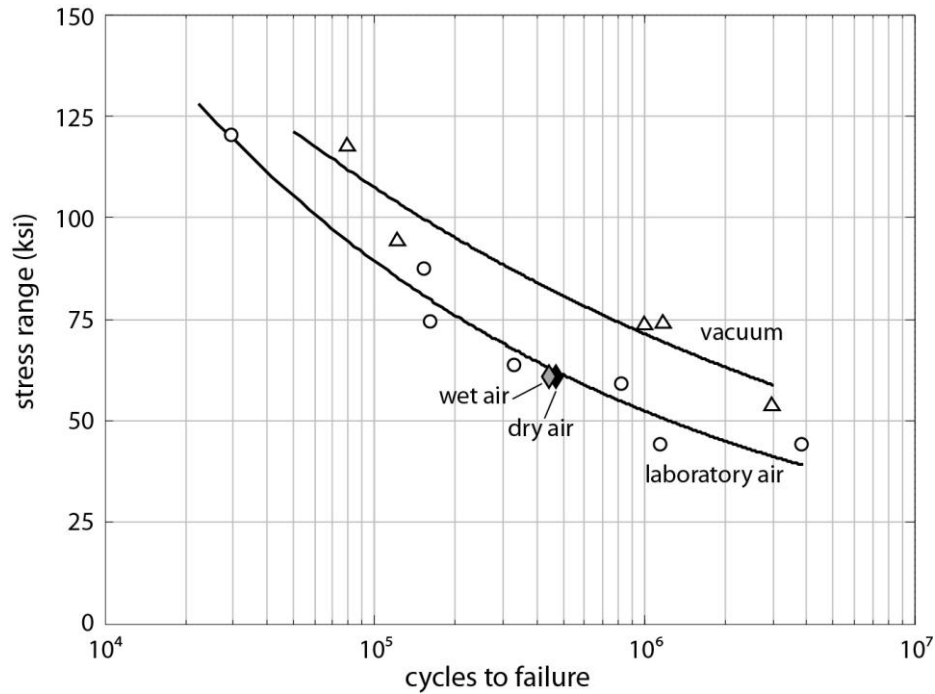


Figure 2-19. Fatigue life data for nickel-based superalloy adapted from Duquette [28]; experiments were conducted in vacuum, laboratory air, dry air, and humidified air.

Experimental Evidence of Delamination and the Correlation between Oxidation and Wear Rates in High Current Density Copper Sliding Electrical Contacts

From the delamination theory of wear it is expected that wear particles will exhibit a sheet-like morphology. Evidence of such flake-like debris was observed by the author and colleagues embedded in between the bristles of multi-fiber copper brushes after long sliding tests against a copper slip-ring in a humid carbon dioxide environment (experimental apparatus described in more detail in [43] and [17]). The tribometer is illustrated in Figure 2-20 and consisted of two multi-fiber copper brushes (also shown in the figure) sliding on independent wear tracks on the periphery of a copper slip-ring operating in a controlled environment (humid carbon dioxide).

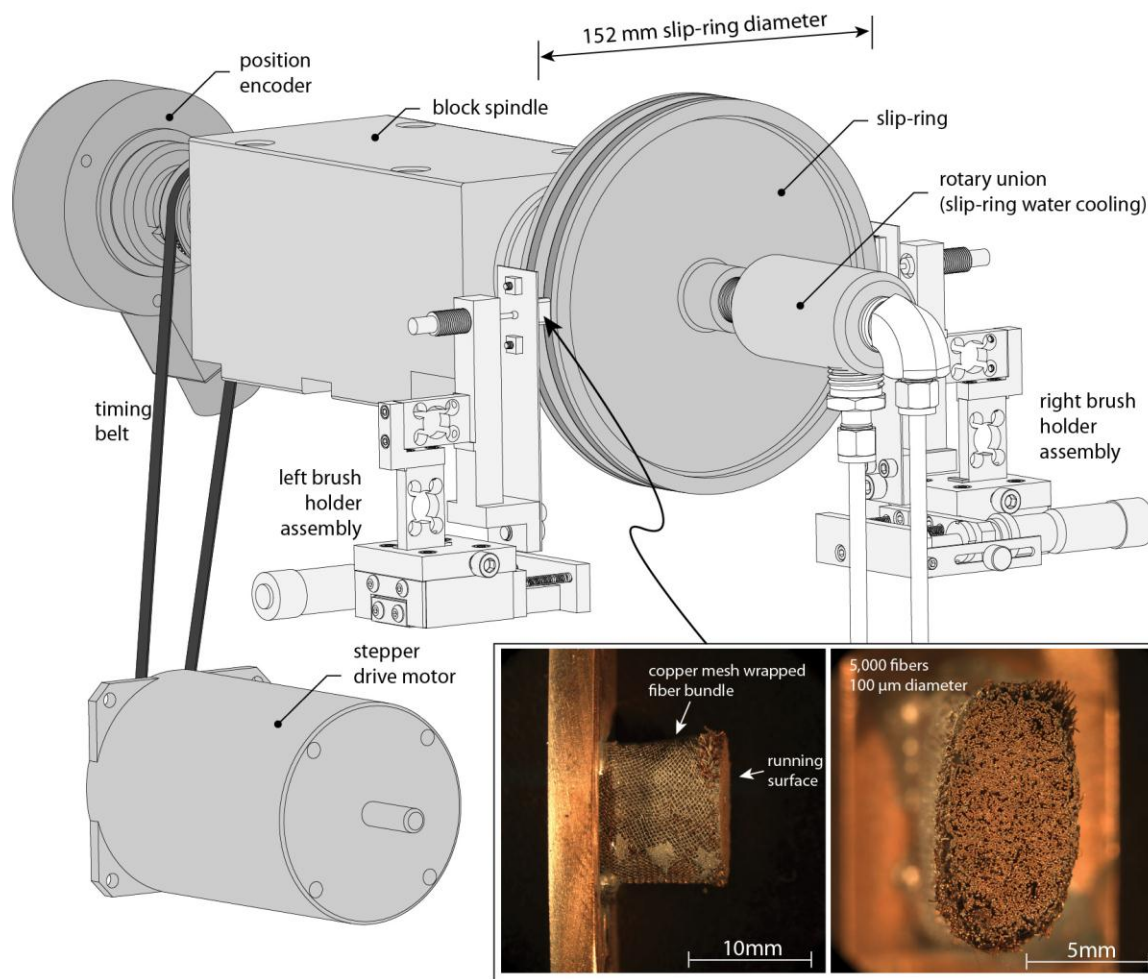


Figure 2-20. Diagram of the major components of a two brush sliding electrical contact tribometer built and operated at the University of Florida Tribology Laboratory, and inset with two photographs of a copper multi-fiber brush; the brush is shown in an unworn state (as new). Photographs courtesy of Nicolas Argibay.

In one experiment the brushes were operated at a nominal brush pressure of 14 kPa for a period of a week (940 km of sliding at a linear brush sliding speed of 2.5 m/s) with a current density as high as 180 A/cm^2 (about 90A DC current). A bifurcation in the linear brush wear rate was evident only at high current density. A summary of the test data is shown in Figure 2-21.

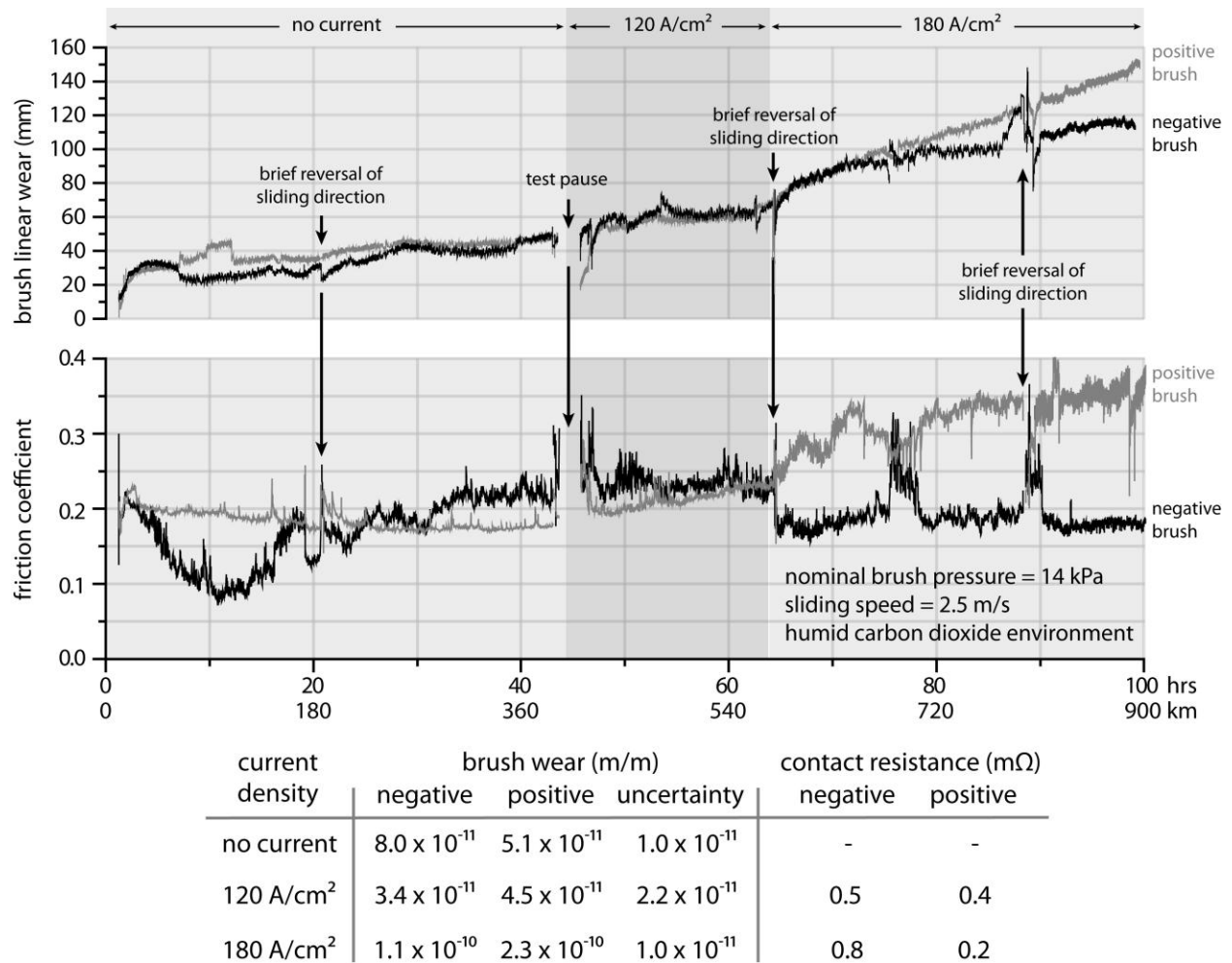


Figure 2-21. Summary of data for a multi-fiber copper brush sliding electrical contact experiment (published in [43]); plots of linear brush wear and friction coefficient vs sliding distance (sliding reversals are performed for a period of 30 minutes at three instances throughout the experiment to measure load cell drift) and a table summarizing brush wear, uncertainty in brush wear, and contact resistance in the various current density regimes.

The following observations were made:

1. The dimensionless (linear) wear rate of the positive brush (that is, the brush into which electrons flow from the slip-ring surface and which exhibits an increased oxide growth rate in the presence of a sufficiently large externally supplied electric field due to the modified Cabrera-Mott oxidation theory proposed by Boyer, et al. [11])

was 2x higher than the negative brush, a phenomenon that only becomes apparent at high enough current density

2. At lower current density this effect was not apparent, where presumably the external electric field applied across the interface as the driving mechanism for current flow is simply not high enough to substantially affect the rate of oxidation with respect to the rate of wear
3. Notably, the friction coefficients and contact resistances are relatively similar for both brushes at lower current density and in the absence of current, only becoming dissimilar once the higher current density was applied

Experimental data published by Boyer in the 1980s [11] using copper cadmium metal fiber brushes of similar design sliding on copper cadmium slip-rings also of similar geometry in a humid nitrogen cover gas resulted in a ~ 3x difference in wear rate based on polarity, where the positive brush wore more. They also report a difference in contact resistance, though in their case the positive brush had a 2x greater resistance than the negative. Reichner [14] observed dissimilar friction coefficients and contact resistances in similar copper fiber brush on copper slip-ring experiments in humid carbon dioxide, though the trends were reversed (higher friction on the negative brush and higher contact resistance on the positive brush). In the same publication, Reichner reports that for the case of copper brushes on a silver slip-ring there was no difference in friction coefficient or contact resistance.

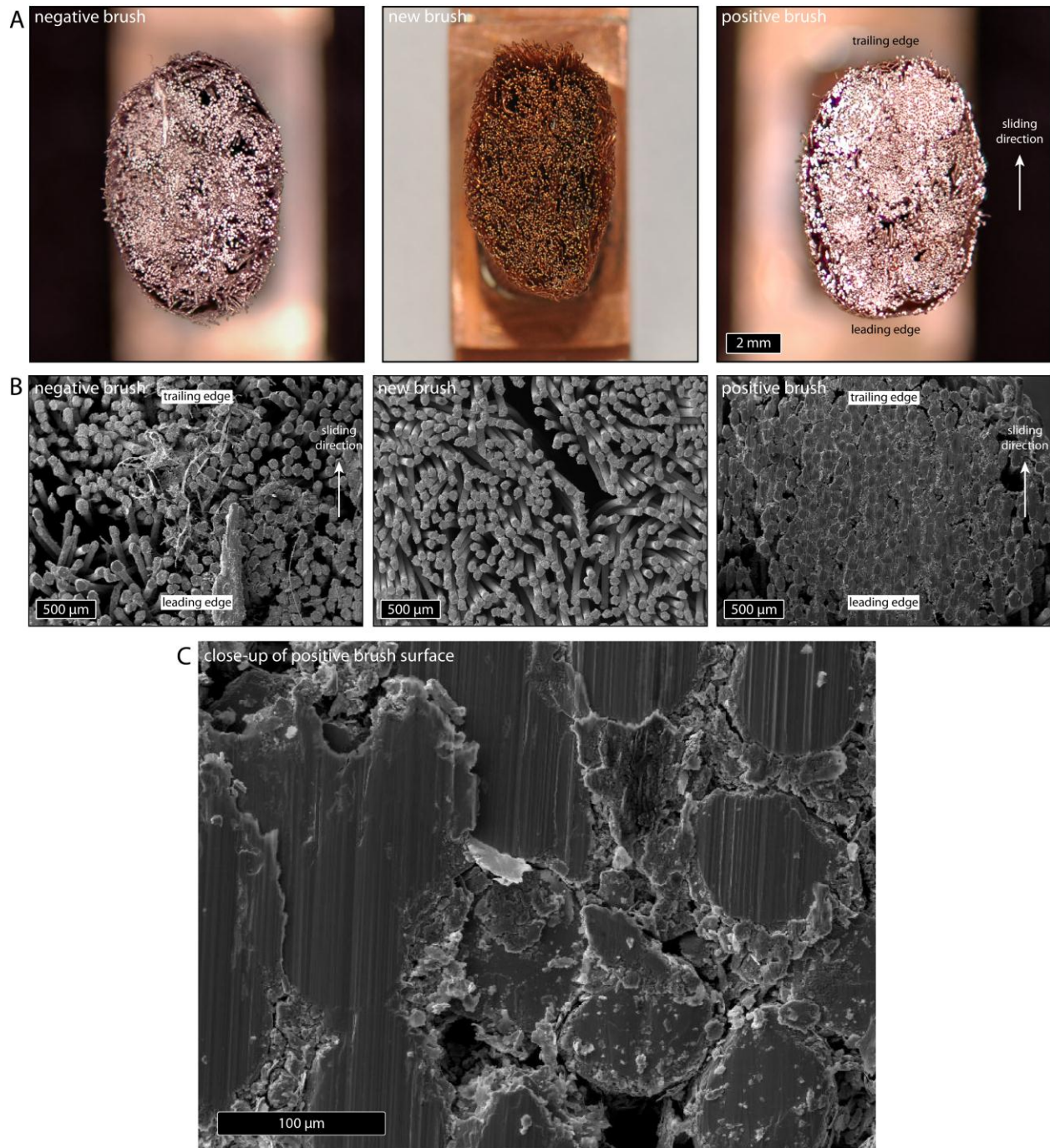


Figure 2-22. Photographs and SEM micrographs illustrating copper brush wear. (A) Photographs of an as new brush, the worn negative brush and worn positive brush, (B) SEM micrographs of the respective brush fiber surfaces, and (C) an SEM micrograph of the worn positive brush showing lamellar, flake-like wear debris compacted between fiber tips (note that the debris is not visible in the worn negative brush). Photographs courtesy of Nicolas Argibay.

The only clear trend is in the approximately 2x higher wear rate of the positive brush. It is apparent that there is a polarity driven effect on the contact resistance and friction coefficient of copper and silver alloy brush and slip-ring systems, even in varying environments. Figure 2-22 presents photographs and SEM micrographs of the worn copper fiber brushes from the experiment described in Figure 2-21, as well as for an unworn brush as reference. SEM micrographs reveal a vastly different evolution of the fiber tips. Upon closer inspection of the positive brush (this is the brush that receives electrons from the slip-ring surface during sliding; bottom micrograph) the presence of flake-like debris is evident on the surface of the fiber tips and in the space between fibers.

Debris from a 2006 experiment collected from a positive brush was imaged using SEM and analyzed using x-ray diffraction (XPS) by Irwin L. Singer (U.S. Naval Research Laboratory). He found that the debris (Figure 2-23) was flake-like in nature and primarily made of copper, rather than copper oxide, indicating that the flakes are not due to a delamination of a very thick oxide film. That is, the enhanced oxide growth rate was not simply resulting in very thick oxides that failed due to strain at the oxide-base metal interface, but indeed was comprised of bulk copper fiber (or slip-ring) material.

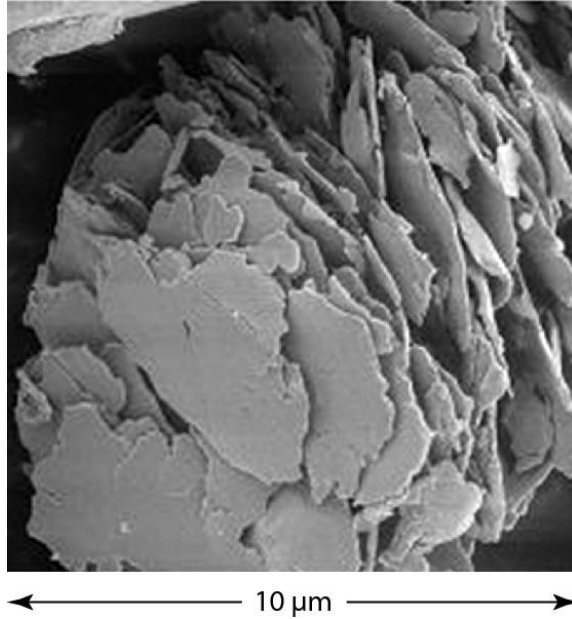


Figure 2-23. SEM micrograph of wear debris extracted from between the metal fibers of a positive copper fiber brush after a sliding experiment in humid carbon dioxide. SEM micrograph courtesy of Irwin L. Singer.

An example of experimental evidence of flake-like morphology of lightly loaded metal sliding electrical contacts appears in a publication by Brown, Kuhlmann-Wilsdorf, and Jesser [63] where they slid silver multi-fiber brushes on a gold coated metal slip-ring at relatively light loads and observed debris of the type shown in Figure 2-24.

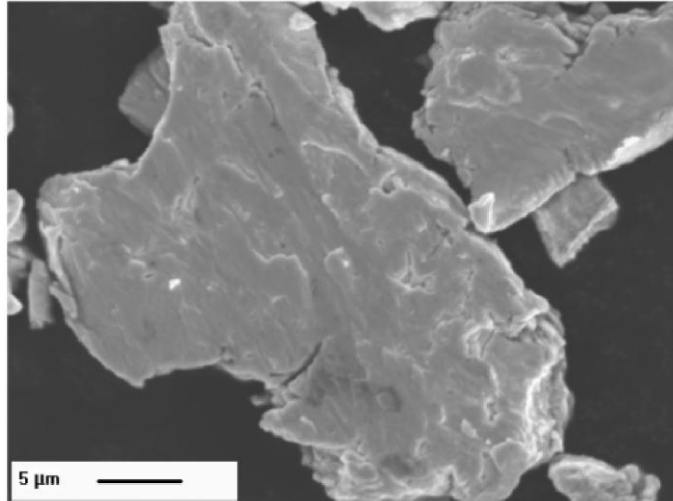
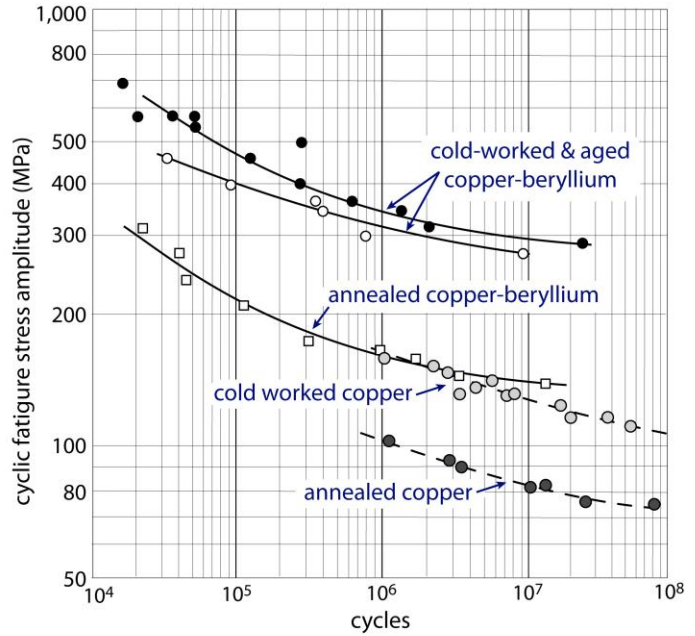
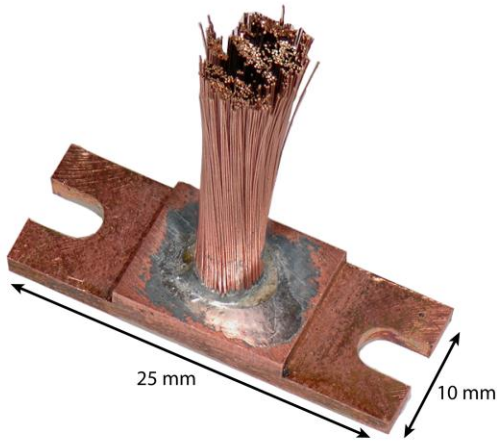
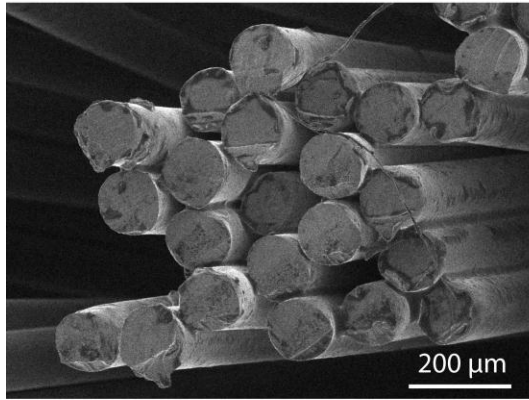


Figure 2-24. SEM micrograph of wear debris from a silver multi-fiber brush sliding experiment on a gold slip-ring exhibiting a flake-like morphology, reproduced from Brown et al. [63]. Reprinted from Transactions on Components and Packaging Technologies, Vol. 31, Issue 2, Brown, L., Kuhlmann-Wilsdorf, D., *Testing and Evaluation of Metal Fiber Brush Operation on Slip Rings and Commutators*, pp 485-494, © 2008, with permission from IEEE.

Experimental Investigation with a High Fatigue Strength Copper Alloy

An attempt was made to provide indirect evidence of the proposed correlation between fatigue strength and electrochemically enhanced delamination wear of low contact pressure, high current density metal sliding electrical contacts. The following is a summary of the work published by the Argibay et al. in [64]. Sliding experiments were performed using multi-fiber metal brushes of a relatively higher fatigue strength copper-beryllium alloy (UNS C17200), shown in Figure 2-25 along with an SEM micrograph of the unworn fiber tips. The experiments were performed on the tribometer shown in Figure 2-20 in equivalent conditions to the copper multi-fiber brush tests described in the preceding sub-section.



*fatigue strength data is from the international copper association. The copper-beryllium alloy is UNS C17200, with a yield strength of approximately 1 GPa.

Figure 2-25. Copper-beryllium UNS C17200 fiber brush comprised of approximately 1,000 metal fibers of 120 μm diameter, an SEM micrograph of the unworn fiber tips, and a plot illustrating fatigue strength for electrical grade copper and copper beryllium adapted from the International Copper Association database. Photograph courtesy of Nicolas Argibay.

Figure 2-26 shows the positive brush linear wear rate as a function of sliding distance and time. The positive brush was previously found to exhibit enhanced wear at high enough current density, as described by the modified Cabrera-Mott model proposed by Boyer et al. [11]. The brushes experienced uninterrupted sliding for 29 days, covering a total sliding distance of 13,000 km. The top plot shows the portion of the experiment conducted at 2.5 m/s sliding speed, and the lower plot the remainder of the experiment conducted at 7.5 m/s. A normal load of 1.0 to 1.25 N was applied. The sliding speed and current density were varied as shown in the figure.

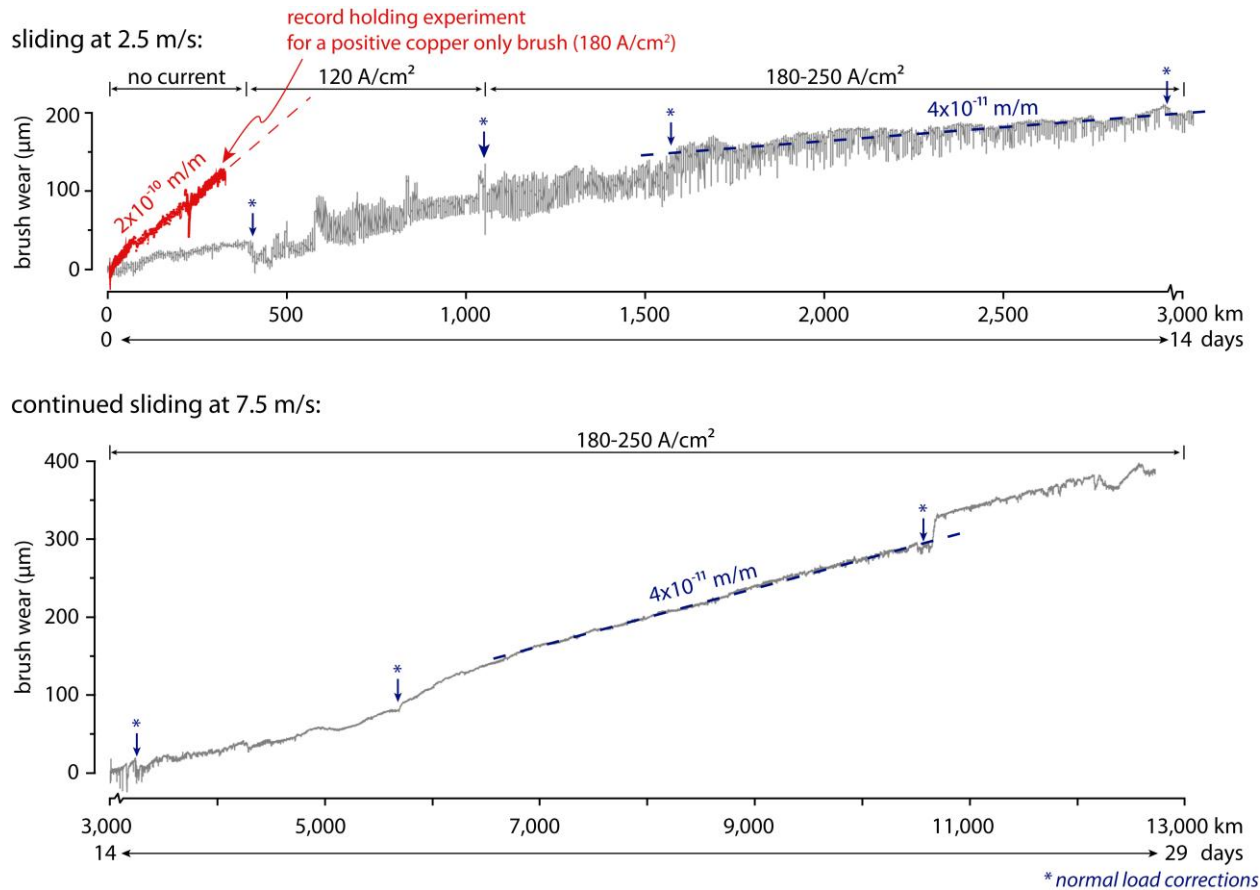


Figure 2-26. Plots of friction coefficient as a function of sliding distance for copper beryllium multi-fiber brushes sliding on an electrical grade copper slip-ring in humidified carbon dioxide at 2.5 m/s for 3,000 km with DC current transport density from 0 to 250 A/cm² and continuing at 7.5 m/s for 10,000 km at constant 180-250 A/cm².

The measured linear wear rate of the positive brush was approximately 4×10^{-11} m/m, an order of magnitude lower than the copper only multi-fiber brushes operating in equivalent conditions. The wear rate was insensitive to current density values as high as 250 A/cm². The steady-state friction coefficient was $\mu \sim 0.15$. The steady-state contact resistance was $R \sim 8$ mΩ, approximately one order of magnitude higher than the copper only brush, in agreement with the order of magnitude higher bulk resistivity of the copper-beryllium alloy implemented. Figure 2-27 shows SEM micrographs comparing the worn and unworn fiber tips, and further evidence of the flake-like debris morphology captured in between the metal fibers.

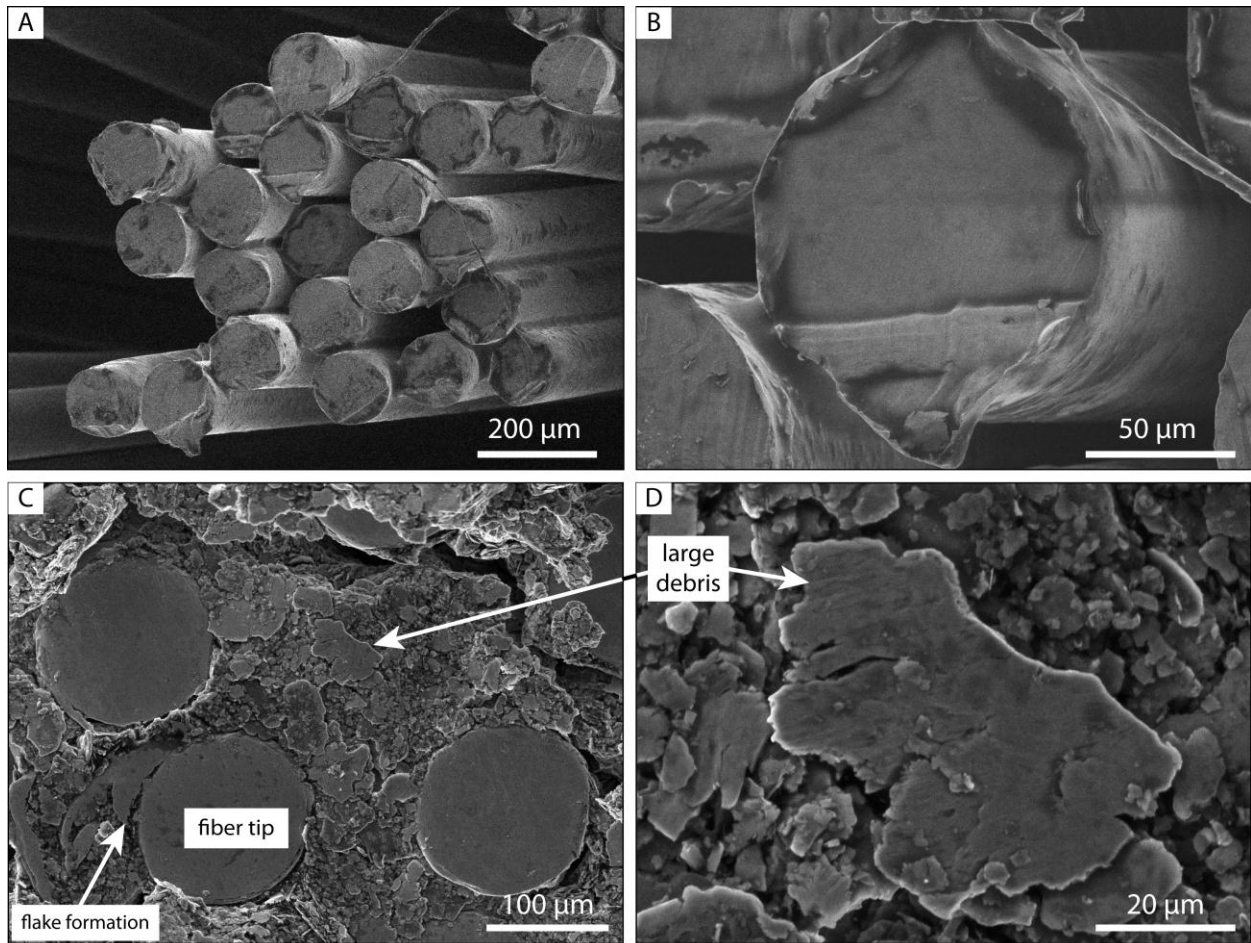


Figure 2-27. SEM micrographs of worn and unworn copper-beryllium brush fiber tips. (A and B) Micrographs of unworn fiber tips appear relatively flat as a result of fracture of the tips during preparation. (C) SEM micrographs of the same fiber tips at the end of the test where the tips appear polished as a result of about 12,000 km of sliding wear. (D) SEM micrograph of plate-like wear debris found between the fiber tips.

End of Chapter Summary and Proposed Research

There is evidence to support the theory that wear of low contact pressure, high current density non-noble metal sliding electrical contacts operating in oxidizing environments will be governed primarily by fatigue wear in the form of delamination. Asymmetry in the wear rate of copper and other oxidizing metal fiber brushes at high current density has been documented in various independent studies [2, 11, 14, 18, 43, 53]. It is postulated that the mechanical origin of

the asymmetry in wear of these systems is explained by a correlation of the modified Cabrera-Mott oxidation model proposed by Boyer, et al. [11], the dislocation trapping mechanism proposed by Shen, et al. [25] and Nazarenko, et al. [62], and the mechanism of fatigue induced delamination wear proposed by Suh [58].

Although various wear processes play a role in the wear of these contacts (e.g. abrasion and electro-migration), the mechanism of delamination appears to be the dominant process for these low wear systems, where at high current density the net electric field through a constantly growing thin oxide film is susceptible to the externally applied voltages used to drive current through the sliding interface. The modified Cabrera-Mott model proposed by Boyer [11] shows how the growth rate of thin oxide films may be affected by the external electric potential, inhibiting (cathodic brush polarity) or enhancing (anodic brush polarity) the growth rate of the films in a weakly oxidizing environment such as with humid argon, nitrogen and carbon dioxide cover gases typically implemented in high performance sliding electrical contact systems to achieve low wear and contact resistance. Nazarenko et al. [62], Shen et al. [25] and Duquette [28] showed that the fatigue life, rate of formation of dislocations, and dislocation trapping near metal surfaces is directly linked to the presence and thickness of oxide films. Suh [58], Fleming et al. [59], and Jahanmir et al. [23, 60] proposed a model to explain how delamination (crack propagation) is a function of the rate of dislocation formation and coalescence in metallic friction surfaces.

These observations suggest a more complete model explaining the origin of wear rate asymmetry observed in non-noble metal sliding electrical contacts in oxidizing environments, and also suggest possible ways of achieving technological improvements. It is proposed that substantial improvements in the current carrying capacity of current collectors may be achieved

using relatively inexpensive materials (e.g. copper multi-fiber brushes) if the process of oxidation is inhibited and if wear, particularly adhesion between similar metal contacts in the absence of a passivation film, is mitigated by implementation of a proper lubricant/coolant without causing separation of the sliding contact (e.g. fluid film separation due to hydroplaning for the case of a liquid lubricant). An example of such a system is proposed and experimentally demonstrated, one with the potential of achieving substantial current density transport ($400+ \text{ A/cm}^2$) while maintaining relatively low wear through immersion of the sliding electrical contact in a stable, electrically insulating, thermally conductive, low viscosity liquid hydrofluoroether medium. The life of metal brush current collectors may also be improved in the absence of a passivating film by implementing relatively hard and high fatigue strength materials for brush construction (e.g. copper-beryllium) and relatively soft materials for the slip-rings (e.g. soft electrical grade copper), sacrificing the more voluminous system component (the slip-ring) and enduring the majority of plastic deformation and wear, prolonging the life of the brush.

CHAPTER 3 DESCRIPTION OF EXPERIMENTS

Chapter Summary

This chapter describes the equipment, procedure, and matrix of experiments performed in the search for a deeper understanding of the tribological behavior of metal sliding electrical contacts and the role of electrochemically enhanced oxidation on wear performance. Section 3.1 describes the various features and capabilities of the custom micro-Newton force tribometer built to study sliding contacts in both prescribed liquid and gaseous media, with and without the transport of electrical current, and with the option of decoupling electrochemical oxidation and transport current by performing *in situ* voltammetry of metal disks while in sliding. Section 3.2 focuses on the procedure, sample preparation, and a description of the various experiments and their respective focus.

Microtribometer

Summary of Microtribometer Capabilities

The tribological experiments described in this document were performed on a modular micro-tribometer (friction testing apparatus with micro-Newton measurement resolution) custom built to acquire these measurements. The tribometer, shown in Figure 3-1, operates in a pin-on-disk configuration. The term modular refers to the possible variations in prescribed testing parameters such as cover gas, submersion of the sliding contact in a liquid medium, electrical current transport through the junction of a conductive pin/disk sliding contact, and *in situ* voltammetry of the metal disk using a potentiostatically controlled three-electrode cell.

The primary purpose of the tribometer was to accurately apply a normal force and linear sliding speed on a pin and disk contact pair of varying material composition while in a prescribed gas/liquid environment and to measure the time varying friction response. The use of copper (of

varying alloy and post-manufacture processing, i.e. poly- and single crystal) as the disk composition was the common thread for all experiments performed.

Two variations in disk geometry and composition were used: the counterface was either (1) the flat end of a polished 20 mm diameter, 30 mm long copper cylinder (McMaster-Carr, UNS C11000), or (2) a copper single crystal disk with an nominally atomically flat $(1\ 0\ 0)$ orientation on the sliding surface (Princeton Scientific Corp) and dimensions of 25 mm diameter and 2 mm thickness.

Three variations in pin material and geometry were used: (1) a non-porous high-alumina ceramic cylinder (95% alumina, shown in Figure 3-1) with a rounded and polished tip radius of approximately 1.75 mm, (2) a highly polished sapphire half-sphere (Edmund Optics) with a 1.59 mm radius, and (3) a circularly bent (toroidal) copper-beryllium metal fiber (UNS C17200, full hard; shown in Figure 3-2) with nominal fiber diameter and bend radius of 120 μm and 3.0 mm, respectively. Details of sample preparation are discussed in Chapter Section 3.2.

The rotating copper disk (also referred to as the countersurface or counterface) was driven by a stepper motor (Schneider Electric Motion, model MDrive 17). The disk was rigidly attached to a pair of three-screw runout correction platens, in turn attached to the motor shaft with a set screw. The motor had a speed range of 10 to 500 RPM. The wear track radius was set by translating the motor/disk assembly using a micrometer driven linear stage, allowing for micrometer precision and repeatability.

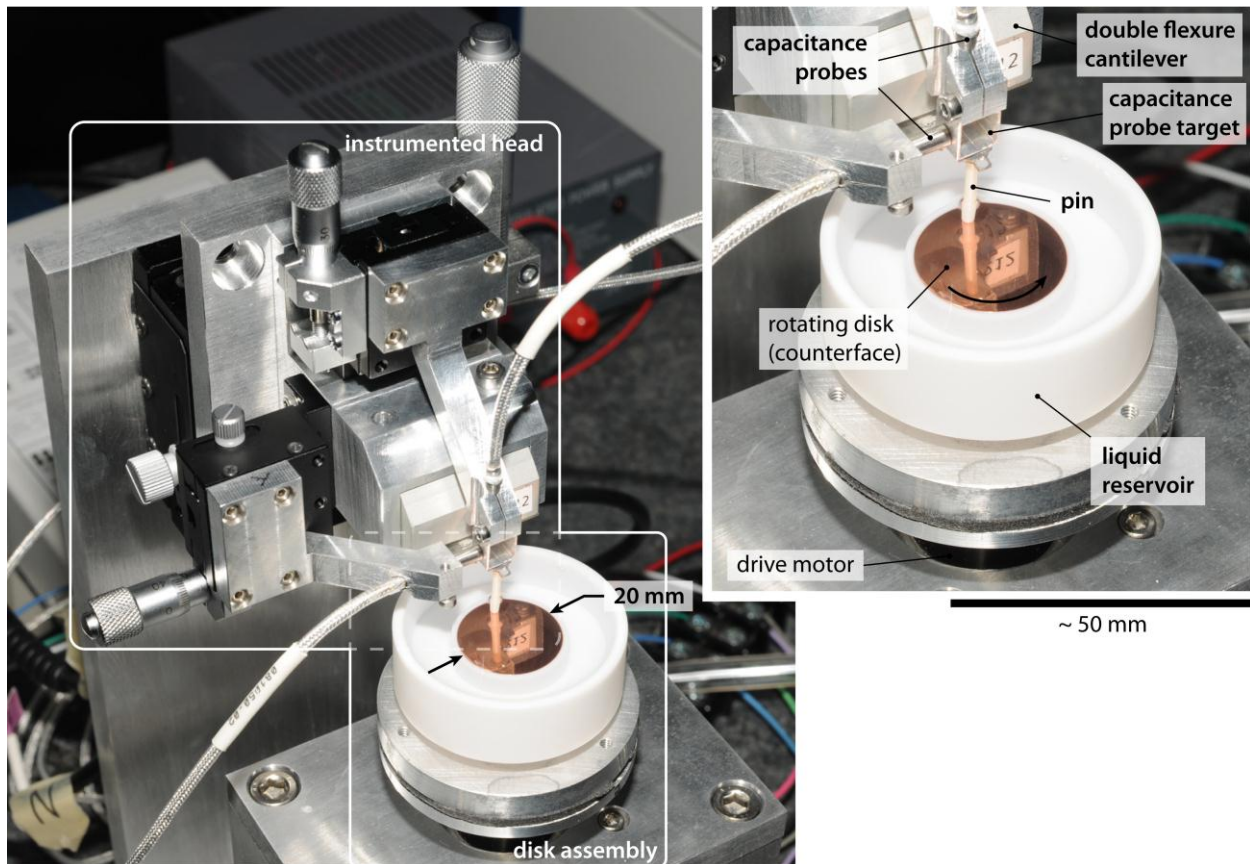


Figure 3-1. Photographs of the custom built tribometer used for microtribological experiments in prescribed gaseous and liquid (fully submerged contact) environments. In these images the sliding pair was a rounded and polished alumina post and a polished 20 mm diameter copper disk; the environmental enclosure used to contain the prescribed cover gas is omitted for clarity. Photographs courtesy of Nicolas Argibay.

Applying and Measuring Contact Forces

The instrumented head includes the flexural cantilever (TETRA GmbH) onto which the pin is adhered by means of an epoxy, two non-contacting capacitance probes (Lion Precision, model C11-E) used to measure displacement of the cantilever tip (providing a calibrated measurement of normal and lateral force as a function of displacement), and coarse and fine micrometer driven linear positioning ball bearing stages. The larger (coarse) positioning stage is used to vertically displace the instrumented head, bring the pin into contact with the disk, and set the normal load by further displacement of the pin into the disk beyond initial contact. Normal

load is then a function of the stiffness of the cantilever and the amount of deflection of the cantilever tip. The two fine positioning stages are used to bring the capacitance probes to the optimal (reference) distance from the aluminum target at the tip of the cantilever prior to applying a load. Figure 3-2 shows a detailed photographic view of the cantilever where the underside of the cantilever and double-leaf flexure is visible. The pin type shown in this figure is a circularly bent metal fiber, with a polyetheretherketone (PEEK) cylindrical spacer acting as an electrical insulator between the metal fiber and the body of the cantilever.

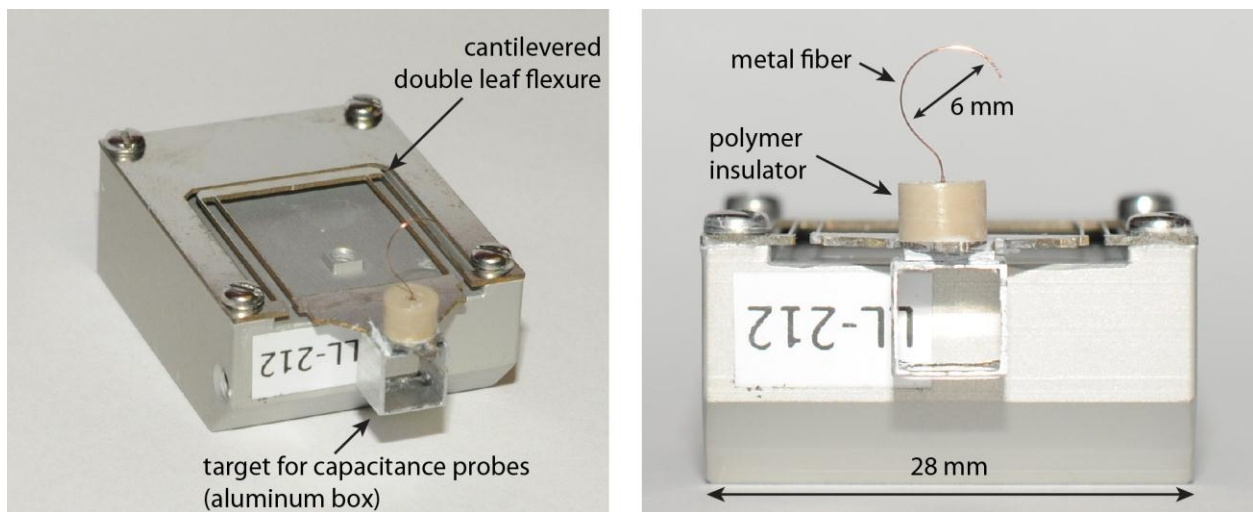


Figure 3-2. Photographs of the double-leaf flexure cantilever assembly with a pin configuration consisting of a curved single copper fiber; the left image shows the cantilevered flexure, designed to provide calibrated lateral and vertical deflections of the pin and rigidly attached capacitance probe target as a response to friction and normal forces during sliding. The S-shaped geometry of the double-leaf flexure inhibits rotation of the pin during lateral deformation. Photographs courtesy of Nicolas Argibay.

Reported friction coefficients are simply the calculated ratio of calibrated cantilever tip deflections in the lateral and normal directions, where calibration refers to the known lateral and normal stiffness of the cantilever in units of force/length. The cantilever implemented for all reported measurements had nominal normal and lateral stiffness values of $k_n \sim 0.038 \text{ mN}/\mu\text{m}$ and $k_t \sim 0.046 \text{ mN}/\mu\text{m}$. The capacitance probe signal conditioner interprets a change in the distance

from target to probe as a calibrated analog voltage; the probes have a measurement range of +/- 50 μm and a nominal spatial resolution of 15 nm or better. Based on the nominal resolution of the probes and the stiffness of the cantilever (neglecting other sources of error such as component misalignment) the optimal force resolution of the system is $\sim 0.6 \mu\text{N}$. In practice, the typical fluctuation in normal force for a stationary loaded contact was on the order of 5 μN . The force range for this system was $\sim 4 \text{ mN}$ in both the lateral and normal directions. A study of force measurement error in low force tribological measurements due to component misalignment was published by Burris, et al. [65]. Details of force/displacement measurement using flexural cantilevers and capacitive probes can be found in references [66, 67] and [68-70], respectively.

Wherever the sliding contact was immersed in a liquid medium it was necessary to account for the contribution to the normal force of the meniscus formed where the pin breaks through the liquid surface (due to surface tension), as well as the component due to buoyancy of the submerged pin. This was done by maintaining a constant liquid level and by performing a software zero of the normal force measurement with the pin submerged to the point just before contact.

Prescribed Gas/Liquid Environments

For sliding experiments in a prescribed cover gas the tribometer was simply sealed in a nylon enclosure and a positive pressure maintained throughout the test to account for slow but unavoidable leaks where the various instrument wirings were fed through. Prior to commencing a sliding test the enclosure was purged until the measured partial pressure of O_2 was below 100 ppm. The O_2 meter was also used throughout the experiment to ensure adequate flow rate of the cover gas. In addition to having a controlled cover gas it was also possible to submerge the sliding contact in a prescribed liquid medium. This was achieved by press-fitting a polymer cup

(polytetrafluoroethylene, PTFE) onto the copper cylinder capable of retaining a liquid volume of approximately 12.5 mL.

In Situ Voltammetry Experiments

It was possible to perform tribo-electrochemical experiments by incorporating the liquid cup and rotating copper disk into a potentiostatically controlled three-electrode chemical cell. Figure 3-3 shows the layout of the various components of the tribometer in the *in situ* voltammetry configuration. Sliding was performed while submerged in a prescribed electrolytic solution and a nominally uniform electric field was applied through the sliding surface of the copper counterface in order to vary the rate of electro-formation/reduction and composition of surface films and oxides. In this way it was possible to correlate friction measurements with the known composition of species on the sliding surface, and to actively vary the species during sliding and observe the transitions in friction response.

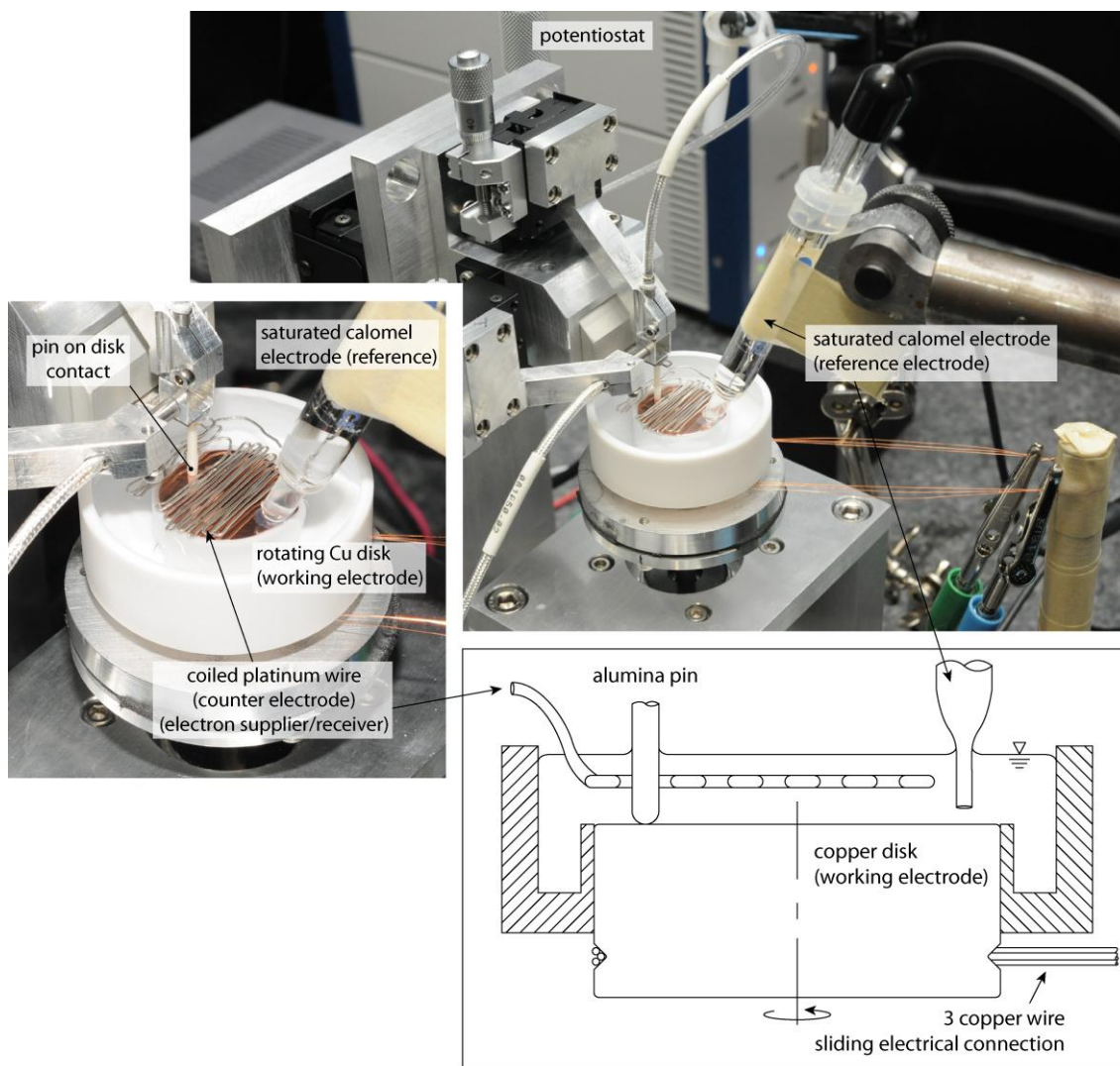


Figure 3-3. Photographs showing experimental setup and a cross-sectional illustration of the tribometer configured for friction experiments with in situ voltammetry; visible are the components of the potentiostat controlled electrolytic cell: a working electrode (the copper disk), a counter electrode (a coiled platinum wire), and a reference electrode (saturated calomel electrode). The current path for charge carriers between the copper disk and potentiostat was a 3-copper wire slip ring. Photographs courtesy of Nicolas Argibay.

The electrical connection between the potentiostat and working electrode was achieved using a three copper wire bundle sliding on a V-notch groove machined on the copper cylinder. The submerged portion of the platinum wire acting as counter electrode had a 0.50 mm diameter and 400 mm length, equivalent to an approximate nominal surface area of 628 mm². The

nominal surface area of the platinum counter electrode was 2x greater than that of the copper working electrode. A potentiostat (Gamry Instruments, Reference 600 model) was used to control the three-electrode cell. The potentiostat was set to acquire measurements of cell potential at rate of 100 Hz, and was used to both sustain constant voltages and perform cyclic voltammetry at a constant rate of 0.010 V/s.

Electrical Current Transport Experiments

In some experiments a direct (DC) electrical current was applied through the sliding contact, where the contact consisted of a single metal fiber sliding on the rotating copper counterface. Figure 3-4 shows the tribometer configured for current transport experiments.

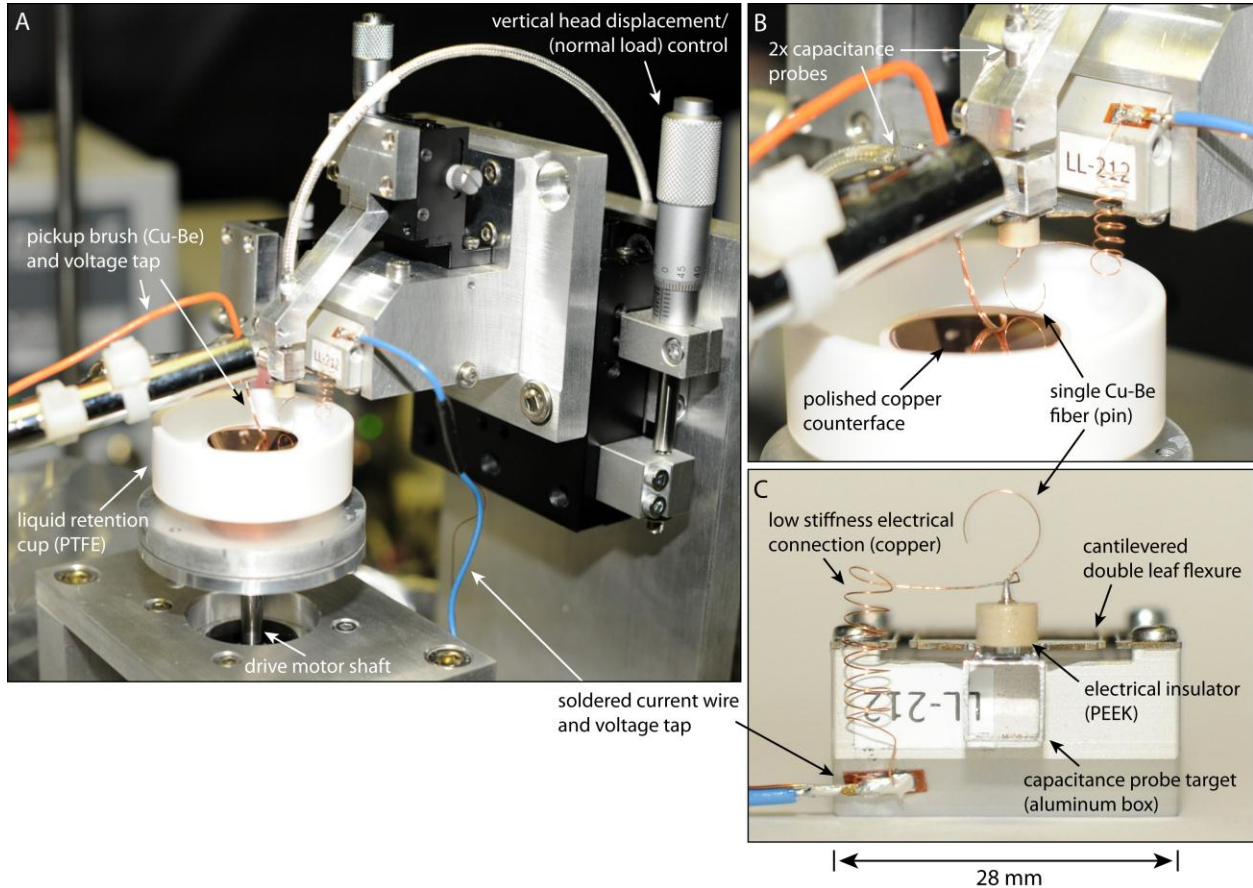


Figure 3-4. Photographs showing the tribometer configured for sliding experiments with electrical current transport illustrating (A) the major components of the tribometer, (B) a close-up of the copper-beryllium fiber, copper counterface, fluid retention cup, pickup brush (multi-fiber Cu-Be brush at a relatively high contact load), and two capacitance probes used to measure deflection of the flexure based cantilever and rigidly attached fiber (visible in C) as a calibrated

response to frictional and normal components of force; (C) also illustrates the electrical connection to the single fiber (pin). Photographs courtesy of Nicolas Argibay.

The metal fiber was always configured as the positive element (anode) as this is the configuration of exacerbated wear on the fiber [11]. Current was supplied using a digital multimeter and power supply (Keithley 2400 Sourcemeter) using a controlled voltage output. The line resistance was calibrated to be approximately 100 Ω . Reported contact resistance values are calculated using Ohm's Law, based on the measured current flow and measured voltage drop from fiber to pick-up brush. The voltage drop is measured at the two soldered connections near the contact, one near the end of the pick-up brush and one near the metal fiber (visible in Figure 3-1 C where the current delivery wire and voltage tap wire are soldered to the coiled copper wire connecting to the metal fiber). This setup implies that a part of the contact resistance will be due to the bulk resistance of the copper wire coil, the length of bent copper-beryllium fiber, and the bent length of the multi-fiber copper pick-up brush. The contribution to contact resistance is estimated to be less than about 0.5 Ω , a negligible fraction of the reported values.

Quantifying the Wear Rate of a Toroidal Metal Fiber

Pin wear rates were calculated only for the experimental configuration where a copper-beryllium fiber was bent into a toroidal geometry, as shown in Figure 3-4. Due to the low contact pressures and sliding distances observed throughout the matrix of experiments, wear of the copper disks was always below the measurement threshold and was not reported. The element of interest in sliding electrical contacts is the metal fiber brush, as this is the component continuously in contact and observing wear, justifying a focus on wear of the fiber brush.

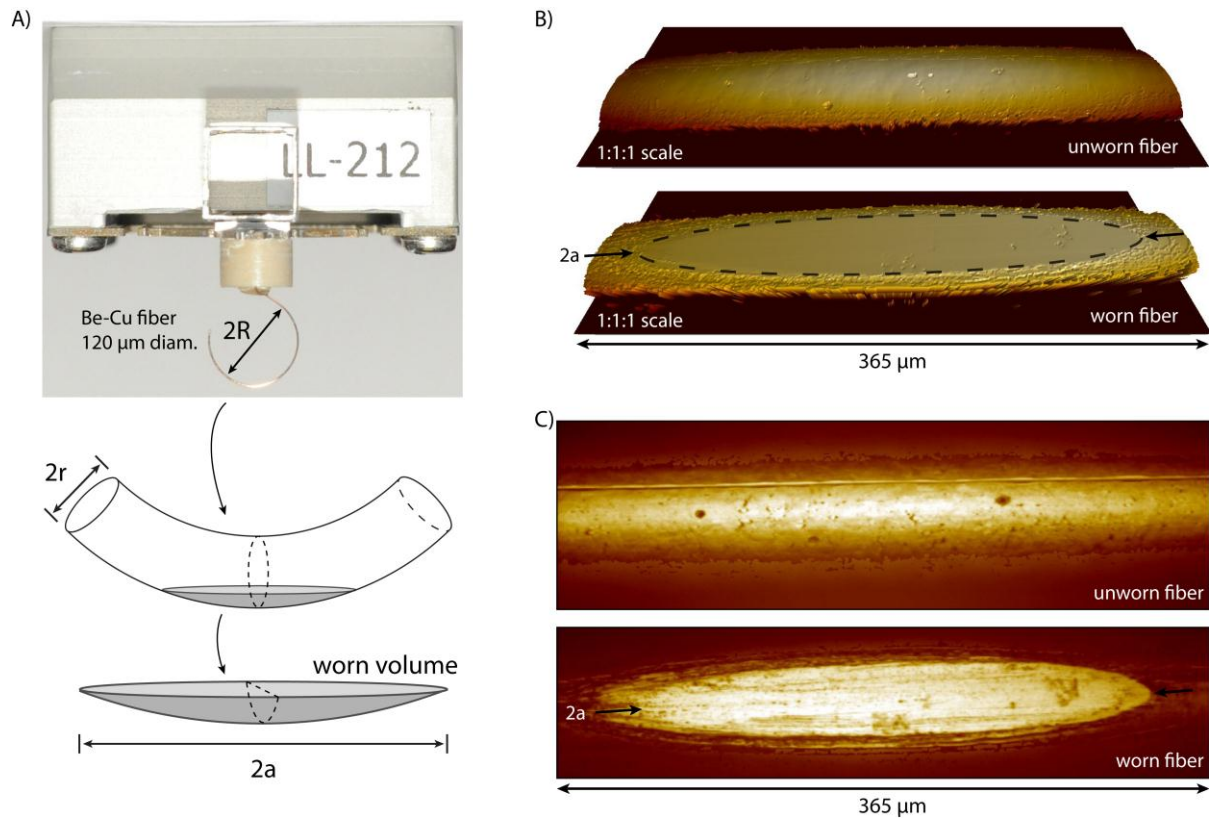


Figure 3-5. Illustrations and SWLI images of wear volume measurement for a single metal fiber. (A) A photograph of the front view of the metal fiber mounted to the cantilever and an illustration of the fiber geometry and wear volume, an example of (B) 3D micrographs and (C) 2D micrographs acquired by SWLI microscopy used to quantify the semi-major diameter ($2a$) of the elliptical wear scar, used in the calculation of the wear volume. Photographs courtesy of Nicolas Argibay.

Pin wear was assessed by measuring the volume removal rate on the metal fiber as a function of sliding distance. The specific wear rate (K_{vol} in $\text{mm}^3/\text{N}\cdot\text{m}$, as explained in Chapter 2) is reported for these experiments. Reiterating, the specific wear rate is the ratio of volume loss (V_{loss}) and the product of sliding distance (s) and applied normal force (F_n). The average normal force value of 0.5 mN was used for all experiments. The sliding distance is calculated based on the calibrated RPM and wear track radius (a wear track radius of 8 mm and a linear sliding speed of 10 mm/s were used, upon a freshly prepared copper counterface, for all experiments). The measurement of wear volume on the toroid fiber is based on the surface geometry of the wear

scar, evaluated using a scanning white light interferometer (SWLI). Micrographs showing worn and unworn fiber surfaces and illustrating the wear scar geometry appear in Figure 3-5.

An expression was derived for calculating the approximate volume of a worn toroidal cap for a high aspect ratio (fiber diameter to radius of curvature) for a fiber with diameter ($2r$) bent into a circular arc (a toroid) of radius (R). The worn volume is effectively the cap of a toroid, producing an elliptical flat spot on the side of the metal fiber with a measured semi-major radius (a). The detailed derivation of the expression for the approximate volume of a toroid segment, Equation 3-1, is provided in Appendix A.

$$V_{loss} \cong \frac{\pi a^4}{4R} \sqrt{\frac{r}{R}} \quad (3-1)$$

The metal fibers had a variation in bend radius (R) between 2.95 and 3.05 mm which was recorded for each experiment, and the nominal fiber radius (r) of 60 μm .

The uncertainty in wear rate $u(K_{vol})$ is a function of the uncertainties in measured volume loss $u(V_{loss})$, normal force $u(F_n)$, and sliding distance $u(s)$. As described in greater detail by Burris et al. [71] and Argibay et al. [43] the uncertainty in volume is typically the primary source of the uncertainty in calculation of specific wear rate. Equation 3-2 is an expression of the uncertainty in the wear volume of a toroidal segment. The derivation is similar to that appearing in Burris et al. [71], Schmitz et al. [72], and assumes negligible uncertainty in the measurement of radii r and R .

$$u(V_{loss}) \cong \left[\frac{\pi a^3}{R} \sqrt{\frac{r}{R}} \right] u(a) \quad (3-2)$$

A conservative approximation of the uncertainty in measurement of the wear scar semi-major radius $u(a) \sim 5 \mu\text{m}$ is assumed for all measurements. This approximation is based on the error in estimating the boundary of the wear scar on an optical micrograph. For the metal fiber

under consideration ($r = 60 \mu\text{m}$, $R = 3.0 \text{ mm}$) and a value for a of $100 \mu\text{m}$, the volume loss based on Equation 3-1 is $V_{loss} \sim 3.7 \times 10^{-6} \text{ mm}^3$ and the uncertainty in volume loss based on Equation 3-2 is $u(V_{loss}) \sim 0.74 \times 10^{-6} \text{ mm}^3$.

Data Acquisition

Data was acquired using a desktop PC with custom LabVIEW software and a National Instruments DAQ card (PCI-6229). Analog voltages are supplied by the capacitance probe controller as inputs and are supplied to the stepper motor controller as output via an NI SCB-68 connector block. The analog signals sent from the capacitance probe controller for each probe is acquired at 10 kHz and averaged into a single data point per second. Each data point is plotted and saved to a tab delimited text file, and corresponds to the average of 10,000 discrete measurements. The resolution of the acquisition card is 16-bit, so for a $\pm 10 \text{ V}$ range of input there is a maximum theoretical resolution of $0.3 \mu\text{V}$. For the known stiffness of the cantilevers used in this study this corresponds to an effective normal force resolution limit of 61 nN , or several orders of magnitude smaller than the measured values. The custom software calculates friction coefficient based on the capacitance probe signals, plots and saves data, and communicates with the motor to set RPM and start/stop motion.

Experimental Setup and Procedures

Sample Preparation: Polishing and Cleaning

The following is a description of the procedures implemented in preparing the various types of pins and disks prior to an experiment, including surface finish and cleaning. The high-alumina ceramic posts and machined polycrystalline copper disks were wet polished and cleaned, while the metal fibers and sapphire balls were simply cleaned and run as received.

The running surface of the polycrystalline copper disks was wet sanded with progressively finer sandpaper down to 1000 grit, followed by wet lapping with $1 \mu\text{m Al}_2\text{O}_3$ -

water slurry on a lapping felt pad. The polished cylinders were promptly rinsed with laboratory grade isopropyl alcohol and imaged using a scanning white light interferometer (ZYGO NewView 5032) to evaluate the surface finish. The average (R_a) and root-mean-square (R_q) surface roughness were calculated based on measured values for three arbitrarily chosen representative scans ($365 \times 365 \mu\text{m}^2$ areas) of the running surface for each counterface, and were in all cases $R_a \sim 15 \text{ nm}$ and $R_q \sim 20 \text{ nm} \pm 10 \text{ nm}$, respectively. After imaging the copper disks were cleaned using laboratory grade solvents in the following order: acetone, methanol, and isopropyl alcohol. Cleaning consisted of laying a dry lint-free cloth on the running surface, saturating the cloth with a solvent causing the cloth to adhere to the surface through surface tension, then dragging the cloth out of contact. This process was repeated three times for each solvent.

The spherical ends ($\sim 1.75 \text{ mm}$ radius tip) of the non-porous high-alumina ceramic cylindrical pins were wet polished with increasingly finer silicon carbide paper and finished by lapping with $1 \mu\text{m}$ alumina slurry. The pins were also promptly rinsed with three laboratory grade solvents in the following order: acetone, methanol, and isopropyl alcohol. The rinsing procedure was implemented to clean the as received copper-beryllium fibers prior to an experiment.

For experiments with a single crystal copper disk it was desirable to have the least amount of oxide and surface contaminants prior to running a sliding test where the disk and pin were submerged in an oxidation inhibiting liquid (a hydrofluoroether). The disks were shipped from the manufacturer in a vacuum sealed container. The disks were only exposed to ambient laboratory air for approximately 30 seconds while the disk was inserted into the polymer liquid retention cup. The disk was initially and immediately submerged in a 10% by volume solution

of acetic acid to remove native oxides, a well-documented method for copper oxide etching [73], and allowed to sit for 30 seconds. The etching solution was then replaced by with the hydrofluoroether solution by dilution. Dilution of the etching solution to less than 1 ppm was achieved by steadily pouring hydrofluoroether into the cup so as to replace the initial solution fifteen-fold times (amounting to pouring about 150 mL of hydrofluoroether into the approximately 10 mL liquid retention cup volume). The liquid covered disk was promptly placed in an inert gas cover in the tribometer enclosure and upon achieving < 100 ppm O_2 inside the chamber the experiment was begun.

Alumina on Copper Sliding Contacts Submerged in Oxidation Dissolving (2M Acetic Acid Solution) and Promoting (3wt% Hydrogen Peroxide) Liquid Mediums

Sliding experiments performed by sliding an alumina pin on a copper counterface were intended as a baseline measurement of friction for this material pair as a precursor to experiments with *in situ* voltammetry where the composition of the surface films on the copper substrate were potentiostatically varied. The contact was operated in a passive chemical cell; sliding took place while submerged in prescribed liquid solutions. Passive implies that oxidation was not actively influenced electrochemically. The objective of this experiment matrix was to establish the friction response of alumina on copper where the copper substrate in both the absence of a protective surface oxide layer and in the presence of a relatively thick protective surface oxide layer of known composition. Two solutions were chosen which fulfilled these requirements, the first a solution of 2M acetic acid and 1M sodium chloride, and the second a 3wt% hydrogen peroxide solution.

Sliding experiments were performed at 10 mm/s linear sliding speed, with a wear track radius of 7 mm (corresponding to approximately 13.6 RPM or 4.4 seconds per revolution), and with an applied normal force of 350 +/- 50 μ N. The polished alumina pins had a tip radius of

curvature in the range 1.6 to 1.9 mm, corresponding to a maximum Hertzian contact pressure of about 65MPa. Prior to applying a normal load and commencing sliding the polished and cleaned copper disk and alumina post were submerged in the corresponding solution for a period of 5 minutes.

Acetic acid (CH_3COOH) may be used to etch copper oxide [73] and was used to achieve a nominally oxide free surface by removing the native oxide present on the copper counterface. The chemical reaction path involves reaction of acetic acid with copper oxide to form copper acetate, which dissolves into the solution. The addition of sodium chloride (NaCl) may be used to enhance the reaction rate. An acetic acid solution was prepared by diluting glacial acetic acid (Acros Organics, 99.8%) with DI water, then adding laboratory grade sodium chloride (Fisher Chemicals, > 99.5% NaCl).

Hydrogen peroxide (H_2O_2) is used as a surfactant in chemical mechanical planarization (CMP) slurries for polishing of copper surfaces [74], where it is desirable to remove a continuously reforming copper oxide layer by mechanical abrasion rather than have an instance where mechanical abrasion occurs on exposed bulk copper. The hydrogen peroxide was purchased as a 3wt% solution from a local pharmacy and used as received. At this concentration, following the work of DeNardis, et al. [74], there was an expected transition in surface film composition during the friction experiment from cuprous oxide (Cu_2O) to cupric oxide (CuO) and cupric hydroxide ($\text{Cu}(\text{OH})_2$) over a period of about 10 minutes, adding a valuable friction response reference measurement.

Alumina on Copper Sliding Contacts with In Situ Voltammetry (in 0.1M Sodium Carbonate)

Sliding experiments with *in situ* voltammetry were performed by sliding an alumina pin on a polished copper counterface submerged in a prescribed electrolytic solution, where

oxidation of the copper disk was actively varied using a potentiostat. A nominally uniform electric field was applied through the sliding surface of the copper substrate while in sliding in order to vary the rate of electro-formation/reduction and composition of surface films and oxides. The prescribed electric field was achieved using a potentiostat controlled three-electrode cell consisting of a working electrode (the copper substrate), counter electrode (a coiled platinum wire), and reference electrode (a saturated calomel electrode, SCE). The purpose of these experiments was to correlate the tribological response of the system to the driving electrochemical potential, and therefore indirectly to the prevalent species on the surface of the copper substrate.

The liquid solution for these experiments consisted of a 0.1M solution of sodium carbonate (Na_2CO_3) prepared using anhydrous soda ash (Colorado Scientific) and DI water. A sodium carbonate solution was selected based on the following criteria: (1) one of the potential byproducts are copper carbonate species which offered the chance to study a system similar in byproduct composition to the macroscopic brush systems operating in humidified carbon dioxide, and (2) due to the fortuitous availability of published data on the cyclic voltammetry behavior of copper systems in 0.1M sodium carbonate solutions [75]. The approximate system pH was monitored throughout the experiment using litmus paper.

Sliding experiments were performed at 10 mm/s linear sliding speed, with a wear track radius of 7 mm (corresponding to approximately 13.6 RPM or 4.4 seconds per revolution), and with an applied normal force of 450 +/- 50 μN . The polished alumina pins had a tip radius of curvature in the range 1.6 to 1.9 mm, corresponding to a maximum Hertzian contact pressure of about 70MPa. Prior to applying a normal load and commencing sliding the polished and cleaned

copper disk and alumina post were submerged in the corresponding solution for a period of 5 minutes.

Sliding Experiments with Sapphire on Single Crystal Copper: Surface Deformation and the Origin of Low Friction and Wear Behavior of Sliding Metal Contacts in the Absence of Oxides/Surface Films

Sliding experiments were performed using a sapphire ball on a copper single crystal submerged in an oxidation inhibiting liquid medium, a hydrofluoroether (HFE; Novec™ 7500 manufactured by 3M™), followed by characterization of the surface and near surface regions of wear tracks after progressively greater sliding distances. Details of HFE are discussed in the next section. Electron microscopy was used to observe and characterize changes in grain structure at the interface of the alumina-copper contact in the absence of a protective oxide after prolonged sliding. Following the procedure first outlined by Prasad, Michael, and Christenson [76], focused ion beam (FIB) milling was used to prepare wear track cross-sections. It was then possible to obtain high spatial resolution images of subsurface deformation by transmission electron microscopy (TEM), revealing the recrystallization and grain refinement at the surface of the copper single crystal.

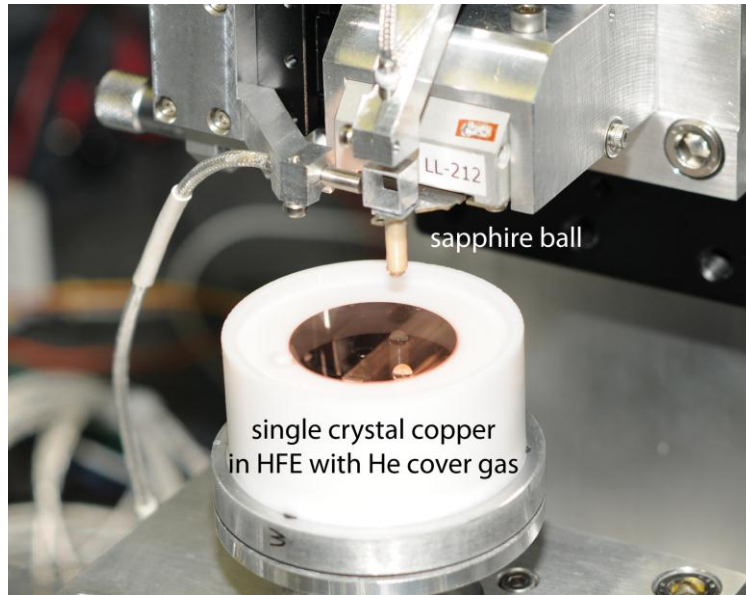


Figure 3-6. Experimental setup showing the sapphire ball and single crystal copper disk immediately prior to sealing the tribometer in the chamber and commencing the helium purge. Photograph courtesy of Nicolas Argibay.

Figure 3-6 shows the setup for these sliding experiments. The sapphire ball was epoxied onto a PEEK standoff to prevent contact between the liquid medium and the bottom of the cantilever. Details of polishing and sample preparations are discussed in the previous section. Sliding experiments were performed at 10 mm/s linear sliding speed, with wear track radii in the range 7 to 9.5 mm in 0.5 mm intervals. Multiple wear tracks were made on one single crystal copper disk so as to avoid oxygen exposure. Each wear track was exposed to a progressively longer sliding distance, enabling a comparison of the grain refinement observed with TEM as a function of sliding distance. An applied normal force of $500 \pm 50 \mu\text{N}$ was applied for all sliding runs.

Experimental Investigation of the Role of Electrochemically Enhanced Oxidation on the Wear Rate of Copper Sliding Electrical Contacts at High Current Density

Sliding experiments were performed to investigate the role of electrochemical oxidation on the wear behavior of copper sliding electrical contacts at high current density. These

experiments were designed to test the hypothesis that it is the localized electric field generated by high enough current density across surface films or oxides on the positively biased surface of a sliding copper contact that exhibits enhanced wear due to enhanced oxidation. In the absence of a mechanism for oxide formation the wear of a positive brush is not expected to be sensitive to transport of high current density across the sliding contact. A hydrofluoroether (HFE; Novec™ 7500 by 3M™) was selected as an ideal fluid capable of acting both as an oxidation inhibitor (by removing the oxygen source) and a thermal conductor to dissipate thermal energy generated due to frictional and Joule heating. Novec™ 7500 is a non-toxic, non-volatile, non-flammable liquid at room temperature, similar to perfluorinated fluids in chemical inertness and dielectric properties, and having a kinematic viscosity (~ 0.77 cSt at 20°C) similar to water over a broad temperature range (~ 5.5cSt at – 50°C and 0.26 at +120°C). Laboratory grade helium (99.999%) was used as a cover gas due to a low but non-negligible solubility of oxygen in HFE. Helium was chosen over other inert gases to maximize the rate of diffusion and displacement of oxygen already dissolved in the HFE prior to purging of the chamber with helium. An oxygen detector was used to ensure < 100 ppm O₂ inside the chamber prior to commencing a sliding experiment.

Table 3-1. Properties of a commercially available hydrofluoroether (Novec™ 7500 manufactured by 3M™)

Physical Property	HFE	Water	
Boiling Point	128	100	°C
Freezing Point	-100	0	°C
Liquid Density	1,614	1,000	kg/m ³
Kinematic Viscosity (STP)	0.77	1	cSt
Thermal Conductivity	0.07		W/m-K
Dielectric Strength	35,000 V for 2.5 mm gap		
Solubility in Water	< 3 ppm by weight		

As a comparison of the tribological performance of sliding copper contacts in HFE experiments were conducted with and without electric current (DC) transport in water, to

demonstrate the propensity for enhanced, voltage sensitive oxidation in an oxygenated medium, and without electric current in a 3wt% hydrogen peroxide solution to verify that the rate of oxidation alone (independent of electric current) enhances wear of copper sliding contacts.

The experimental setup is shown in Figure 3-4 and sliding pairs consisted of a circularly bent (toroidal) copper-beryllium metal fiber (UNS C17200, full hard) with a nominal fiber diameter of 120 μm and a bend radius of 3.0 mm sliding on a polished copper disk (UNS C10000). Details of polishing and sample preparations are discussed in the previous section. Sliding experiments were performed at 10 mm/s linear sliding speed, with a wear track radius of 7 mm (corresponding to approximately 13.6 RPM or 4.4 seconds per revolution), and with an applied normal force of 500 +/- 50 μN . An estimate of the maximum contact pressure for a toroidal metal fiber loaded on its side onto a flat counterface was found using the Hamrock-Brewe contact mechanics solution for elliptical geometry (found in K.L. Johnson's textbook [61]); the approximate max contact pressure was 200 MPa. Friction and contact resistance are reported as a function of sliding distance and time, as well as interrupted *ex situ* measurements of pin (fiber) wear using SWLI microscopy.

CHAPTER 4 EXPERIMENTAL RESULTS

Chapter Summary

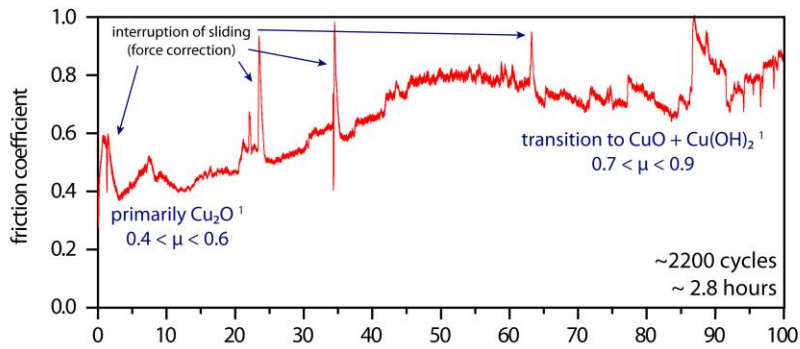
This chapter is broken into subsections, each presenting corresponding friction, wear, and contact resistance results for the various experimental conditions and material pairs described in Chapter 3. Sections 4.1 to 4.3 present experimental results for pin on disk experiments with amorphous and single crystal alumina pins sliding on rotating polished copper counterfaces in varying liquid mediums (including solutions of 3wt% hydrogen peroxide, 2M acetic acid + 1M NaCl, and 0.1M sodium carbonate), with and without potentiostat controlled electrochemical oxidation of the copper substrates. Section 4.4 presents results for single copper-beryllium fibers sliding on poly- and single-crystal copper substrates immersed in varying liquid mediums (including deionized water, a solution of 3wt% hydrogen peroxide, and hydrofluoroether) with and without (DC) electrical current transport.

Alumina on Copper Sliding Contacts in Oxidation Enhancing (3wt% Hydrogen Peroxide) and Inhibiting (2M Acetic Acid Solution) Liquid Mediums

Summary of Results

Figure 4-1 shows plots of friction data for an alumina pin sliding on a polished copper disk as a function of sliding distance. Friction coefficient is reported for an alumina on copper sliding contact submerged in two different solutions. These experiments provide a baseline measurement of friction for a low contact pressure (max Hertzian contact stress ~ 65 MPa) spherical and polished alumina pin on polished copper substrate for the case of immersion in either an oxidation enhancing (3wt% hydrogen peroxide) or reducing (2M acetic acid + 1M NaCl) liquid solutions.

Solution: 3 wt % H₂O₂ (hydrogen peroxide)

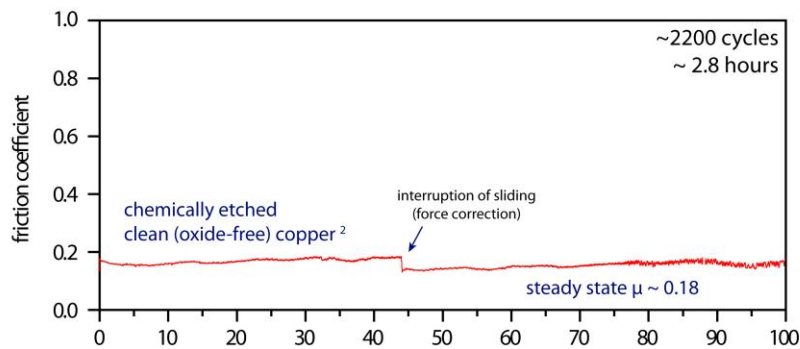


normal load = 300 - 400 μN
sliding speed = 10 mm/s



¹ref: DeNardis *et al*, Thin Solid Films 513 (2006) pp 311-318

Solution: 2M CH₃COOH (acetic acid) and 1M NaCl (sodium chloride)



²ref: Chavez *et al*, Journal of the Electrochem. Society 148 (2001) G640-G643

Figure 4-1. Plots of friction coefficient vs sliding distance for a spherically polished alumina pin (~ 1.75 mm radius) sliding on a polished copper substrate (initial R_a ~ 20 nm) at relatively low contact pressure (~ 65 MPa max Hertzian contact pressure) and at relatively low linear sliding speed of 10 mm/s immersed in two different solutions: 3wt% hydrogen peroxide and 2M acetic acid + 1M NaCl. Photographs courtesy of Nicolas Argibay.

Friction Coefficient of Alumina on Copper in 3wt% Hydrogen Peroxide

There is an apparent trend in friction response over time for the case of contact immersion in 3wt% hydrogen peroxide. It is important to remember that the pin and disk were immersed in the solution for approximately 5 minutes prior to applying a contact load and commencing sliding. In the initial 15 minutes (corresponding to approximately the first 10 m of sliding) the measured friction coefficient fluctuates from about μ ~ 0.6 down to 0.4. This is

followed by a gradual, nearly hour long increase to an apparent steady-state value fluctuating in the range $\mu \sim 0.8$ to 0.9 .

DeNardis, et al. [74] published a study in 2006 on the oxidation growth kinetics of clean copper surfaces exposed to varying solution concentrations of hydrogen peroxide in the range 0.25 to 4wt%. Using XPS and coupled quartz crystal microbalance (QCM) and ellipsometry measurements they were able to show a clear trend in the composition and growth rate of copper species as a function of time and concentration of hydrogen peroxide. They showed that there is an immediate growth of a cuprous oxide (Cu_2O) passivating film followed by the continued non-uniform growth and dissolution of crystals of cupric oxide (CuO) and cupric hydroxide ($\text{Cu}(\text{OH})_2$), with as much as 10 to 20 minutes required to achieve relatively full coverage of the Cu_2O film by CuO and $\text{Cu}(\text{OH})_2$.

It is possible that due to the initial 5 minute immersion period prior to commencing sliding there was a patchy film of CuO and $\text{Cu}(\text{OH})_2$ on the surface of the Cu_2O passivated copper substrate. As the pin began to wear through the growing but still patchy cupric oxide/cupric hydroxide film friction initially decreased to $\mu \sim 0.4$ while contact was mostly with cuprous oxide, followed by a gradual saturation of the copper surface with cupric oxide/cupric hydroxide corresponding to the gradual increase of friction coefficient to relatively higher values in the range $\mu \sim 0.8$ to 0.9 . During the experiment the disk became visibly darker everywhere except inside the wear track, possibly due to the competing oxide film wear/growth. Figure 4-2 shows a reproduction of ellipsometry data published by DeNardis et al. in [74] reporting the growth rate of copper oxides/hydroxide on the surface of a copper substrate in 1wt% hydrogen peroxide. In the same publication they also show that the growth rate of the oxide film is equivalent for 1wt% and 4wt% hydrogen peroxide for approximately one hour, followed by a

slight deviation between their respective growth rates, with a higher growth rate for the case of 4wt%. Also shown in Figure 4-2 are three images of the copper disk at different stages of sliding illustrating the visible change in color of the polished copper disk surface due to an increasingly thicker oxide film.

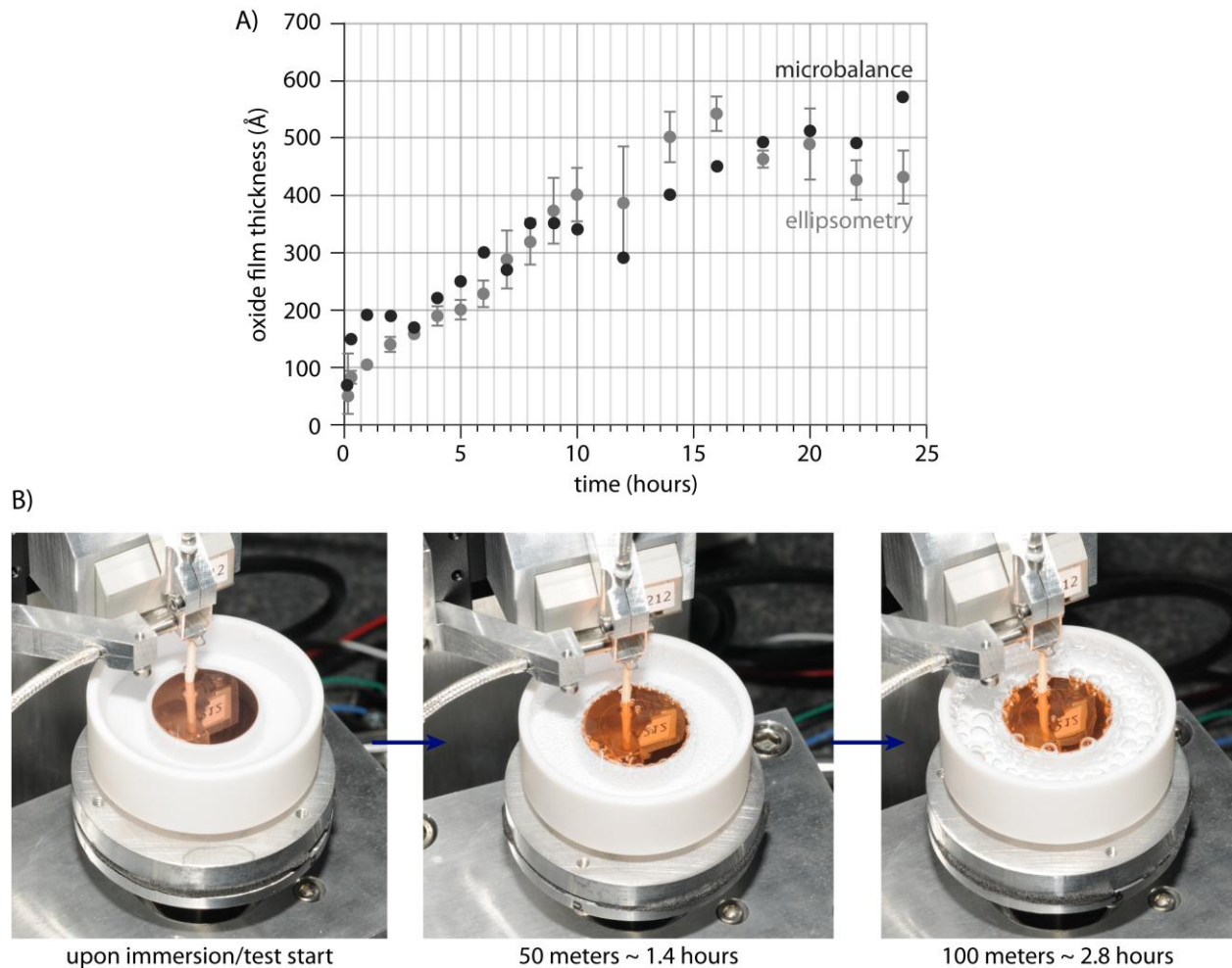


Figure 4-2. Graph of copper oxide film growth kinetics in 1wt% hydrogen peroxide and photographs of copper substrates from experiments in 3wt% H₂O₂. (A) Plot of oxide film growth rate adapted from DeNardis et al. [74] for a copper substrate in 1wt% hydrogen peroxide as measured using ellipsometry and a QCM, and (B) images of the alumina on copper sliding contact in 3wt% H₂O₂ friction experiment data reported in Figure 4-1 as observed at three different stages in the test: immediately after immersion, at the mid-point, and at the end of the experiment. Photographs courtesy of Nicolas Argibay.

Friction Coefficient of Alumina on Copper in 2M Acetic Acid and 1M Sodium Chloride

Friction data for the alumina on copper sliding contact immersed in a 2M acetic acid (CH_3COOH) and 1M sodium chloride (NaCl) solution is shown in Figure 4-1. The friction behavior reveals is effectively constant throughout the experiment, with a steady-state friction coefficient $\mu \sim 0.18$. It is important to note that prior to applying a contact load and commencing sliding the copper disk was immersed in the solution for a period of 5 minutes, providing ample time for reaction and dissolution of the native oxide.

An observed feature in the friction data is the increasing amplitude of fluctuation about the steady-state value of $\mu \sim 0.18$ as the experiment progressed. This feature is attributed to the continued oxidation and etching of the oxide resulting in increasing roughness of the initially polished copper substrate. The continued oxide growth and etching is due to the solubility of oxygen in the approximately 10/90 volume percent acetic acid/water solution. The water and oxygen continue to oxidize the substrate while the acetic acid and sodium chloride react with the oxide to form soluble compounds such as copper acetate and copper chloride.

Alumina on Copper Sliding Contacts with In Situ Voltammetry (in 0.1M Sodium Carbonate)

Summary of Results

Figure 4-3 A shows a plot of friction coefficient versus time/sliding distance/revolutions for pin-on-disk sliding of a high-alumina ceramic pin on a copper substrate. The friction coefficient response was observed to vary as a function of the prescribed electrochemical potential. At the onset of sliding with a strongly reducing potential (- 0.75 V) the friction coefficient was in the range of 0.4 to 0.5. At a sliding distance of 2 m (~ 34 revolutions), with a continued reducing potential, the friction coefficient began to vary between 0.2 and 0.5 possibly due to intermittent exposure of nascent copper along the wear track. When a positive potential

of + 0.25 V was applied the friction coefficient sharply increased to the range 0.7 to 0.9. After each change in prescribed steady-state potential from electroreducing to electroforming and from electroforming to electroreducing extremes there was a transient in current density lasting approximately 55 s (or 12 revolutions), after which current density was constant with no apparent fluctuation in current density with continued sliding (variation < 0.01 mA/cm²). The current density (mA/cm²) reached steady-state values of - 0.40 and + 0.02 mA/cm² after sustained potentials of - 0.75 V and + 0.25 V, respectively. Cyclic voltammetry revealed that the transition between relatively lower friction (0.4 to 0.5) to higher friction (0.7 to 0.9) occurred at the onset of electroformation and electroreduction of the species CuO, Cu(OH)₂ and CuCO₃.

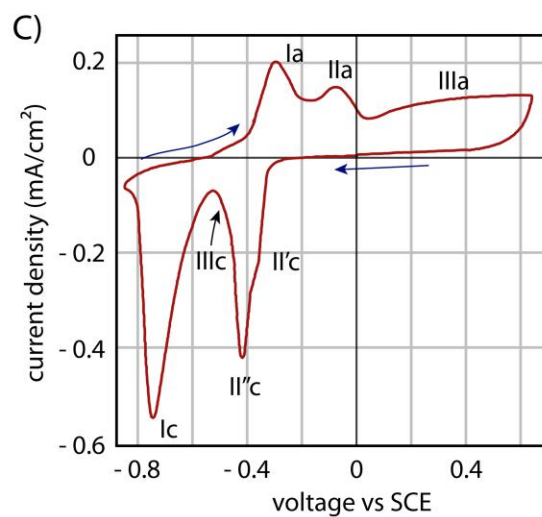
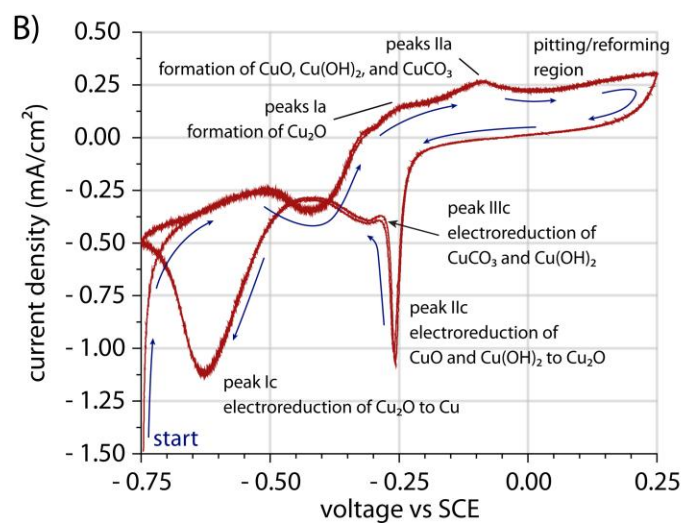
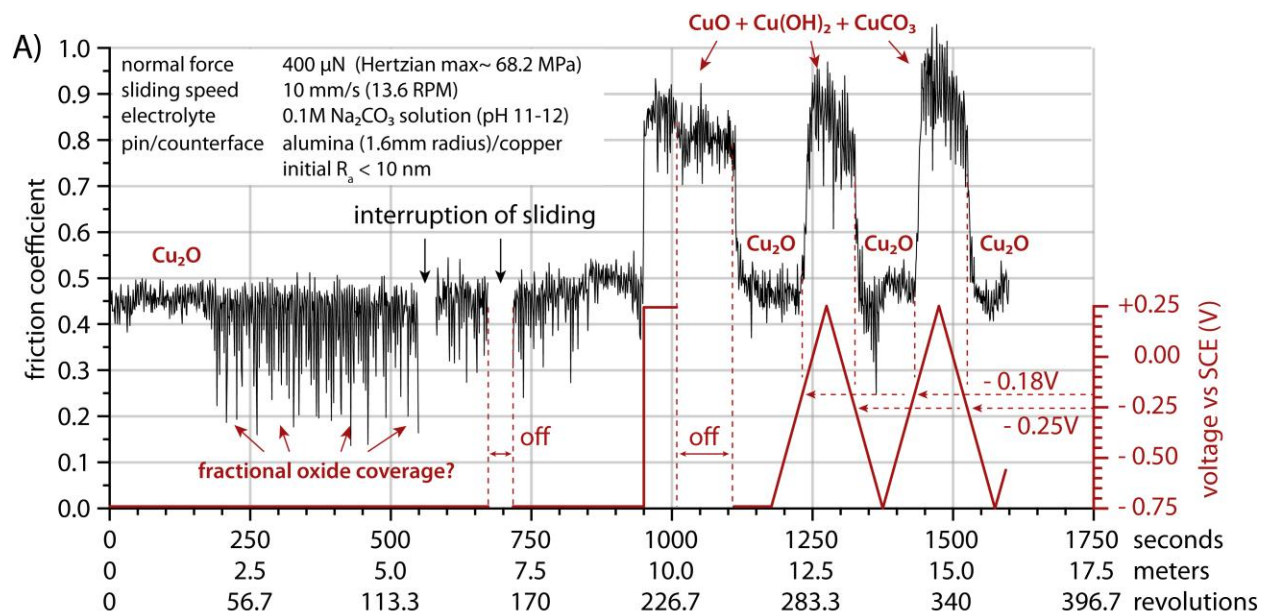


Figure 4-3. Friction and voltammetry data from alumina on copper sliding experiments with in situ voltammetry. (A) Plot of friction coefficient vs sliding distance/time/revolutions, and an overlaid plot of the prescribed driving voltage vs SCE showing the friction response to the potential driving electro-formation/reduction of copper oxides and hydroxides; (B) plot of cyclic voltammetry corresponding to the time interval between 1,175 and 1,600 s in (A); (C) plot of cyclic voltammetry data for a rotating copper disk electrode submerged in a 0.1M sodium carbonate solution (pH 11.1, 25°C) adapted from Sánchez et al. [77].

Friction Behavior at Varying Electric Potential

This paragraph provides discusses friction behavior for the experimental data presented in Figure 4-3 A prior to the period of cyclic voltammetry, the time interval from the beginning of the experiment and through approximately 1,175 s. Initially the driving electrochemical potential was set to a strongly reducing - 0.75 V so as to promote electro-reduction of the native surface oxide. An interruption of sliding occurred at 550 s lasting 60 s. An interruption in sliding and voltage was performed at 675 s lasting 40 s, after which both sliding and a voltage of - 0.75 V were resumed simultaneously. At 950 s the voltage was set to + 0.25 V for 60 s, followed by a 120 s period where potentiostatic control was again interrupted. A sharp increase in friction coefficient to about 0.8 to 0.9 occurred immediately after applying + 0.25 V and remained high during the period of interrupted voltage. At about 1,110 s potentiostatic control was restored with a voltage of - 0.75 V for a period of 75 s, followed by a sharp drop in friction coefficient to a range of 0.4 to 0.5.

Friction Coefficient and Cyclic Voltammetry

Figure 4-3 B shows a plot of cyclic voltammetry (current density vs electric potential) corresponding to the time period from 1,175 to 1,600 s of the experimental friction data presented in Figure 4-3 A. Voltage was cycled linearly from strongly electro-reducing - 0.75 V to strongly electro-forming (passivating) + 0.25 V potentials at a constant rate of 10 mV/s. Figure 4-3 C shows a reproduction of cyclic voltammetry data published by Sánchez, et al. in 1993 [77] also for copper in an equivalent electrochemical environment (0.1M Na₂CO₃ at room temperature and a pH ~ 11.1). Figure 4-3 C is intended to serve both as a reference for and a validation of the experiments described in this manuscript. Peak assignments presented in Figures 4-3 B and 4-3 C were reported by Sánchez, et al. in [75, 77] based on electron microprobe analysis and Gennero De Chialvo, et al. [78], based on ellipsometry.

Figure 4-4 shows a plot correlating friction coefficient to varying electrochemical potential for the data presented in Figure 4-3. The data is also temporally correlated; the spacing between data points corresponds to a 1 second time interval. This plot illustrates the friction response of the alumina/copper pair as a function of the varying surface film/oxide species. Along with the peak assignments from Figure 4-3 C, Figure 4-4 highlights the transition from relatively high to low and low to high friction coefficient occurring at the onset of electroformation or electroreduction of the copper species CuO, Cu(OH)₂ and CuCO₃.

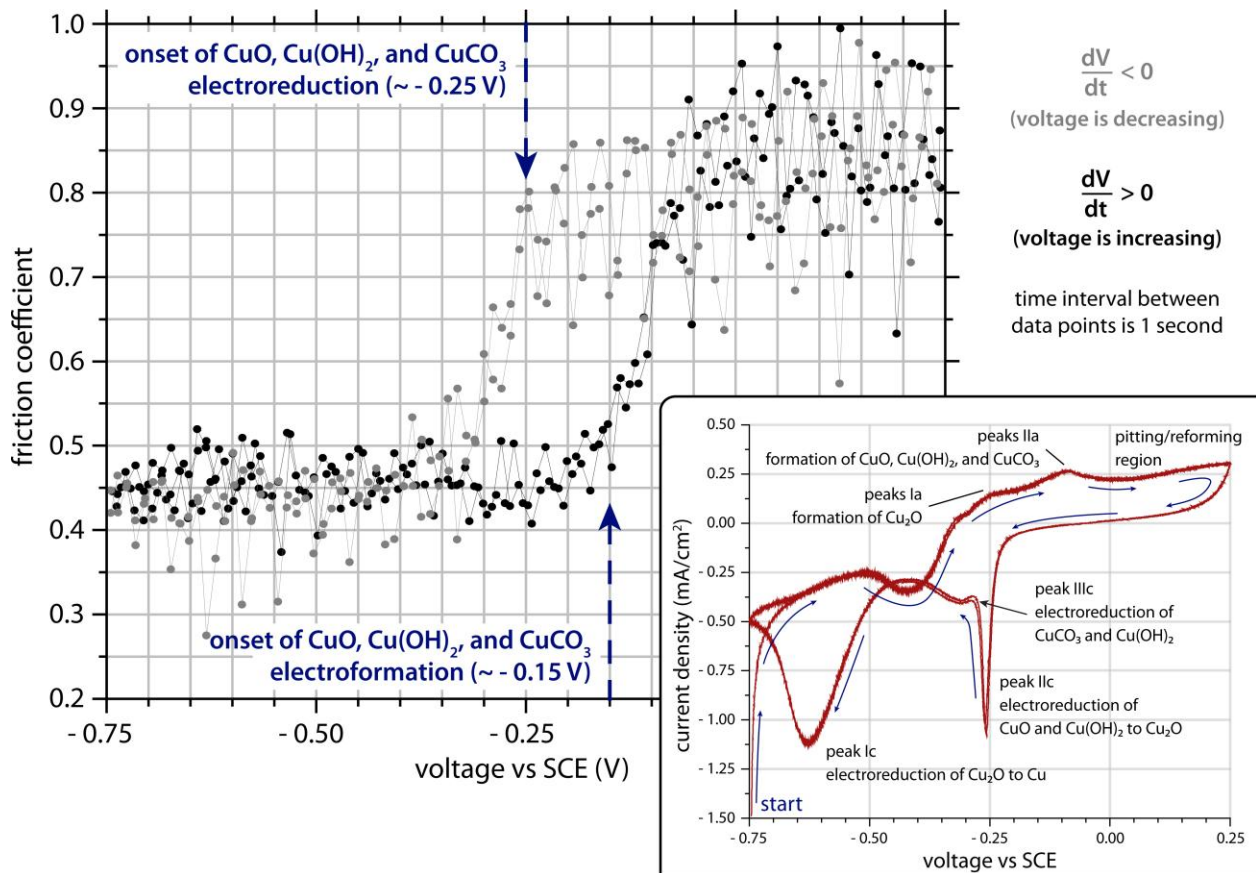


Figure 4-4. Plot of friction coefficient as a function of prescribed potential (versus SCE); the temporal spacing between data points is approximately 1 second (approximately a 1/4 revolution of the rotating copper substrate) and the rate of change of voltage was 10 mV/s. Note the transition to relatively high friction coefficient at the onset of electroformation of cupric oxide (CuO), copper hydroxide (Cu(OH)₂) and copper carbonate (CuCO₃) [75, 77], in contrast to a transition to relatively lower friction at the onset of electroreduction of the same species; based on measured steady-state friction

coefficients in the range of 0.4 to 0.5 and the relatively weak Ia peak it is possible that the complete reduction of cuprous oxide was not achieved.

Sliding Experiments with Sapphire on Single Crystal Copper: A Possible Correlation between Surface Grain Refinement and the Low Friction Behavior of Observed for Sliding Metal Contacts in the Absence of Passivating Films

Figure 4-5 shows measured friction coefficient as a function of sliding distance and revolutions of the copper disk for pin-on-disk experiments for a sapphire ball sliding on single crystal copper. Raw data is shown in black and filtered data in red. Filtering consisted of FFT low-pass smoothing with a cutoff frequency $F_{cutoff} \sim 0.05$ Hz. There is an initial period of relatively higher friction ($\mu \sim 0.5$ to 0.6), transitioning to $\mu \sim 0.2$ in a period of about 10 revolutions of the disk (equivalent to 0.5 m or about 50 seconds of sliding). There is a gradual transition to a friction coefficient $\mu \sim 0.3$ over the length of the test, amounting to 100 m of sliding (or 2000 revolutions). There is a brief pause in sliding after the initial friction transition to verify that load cell drift was negligible.

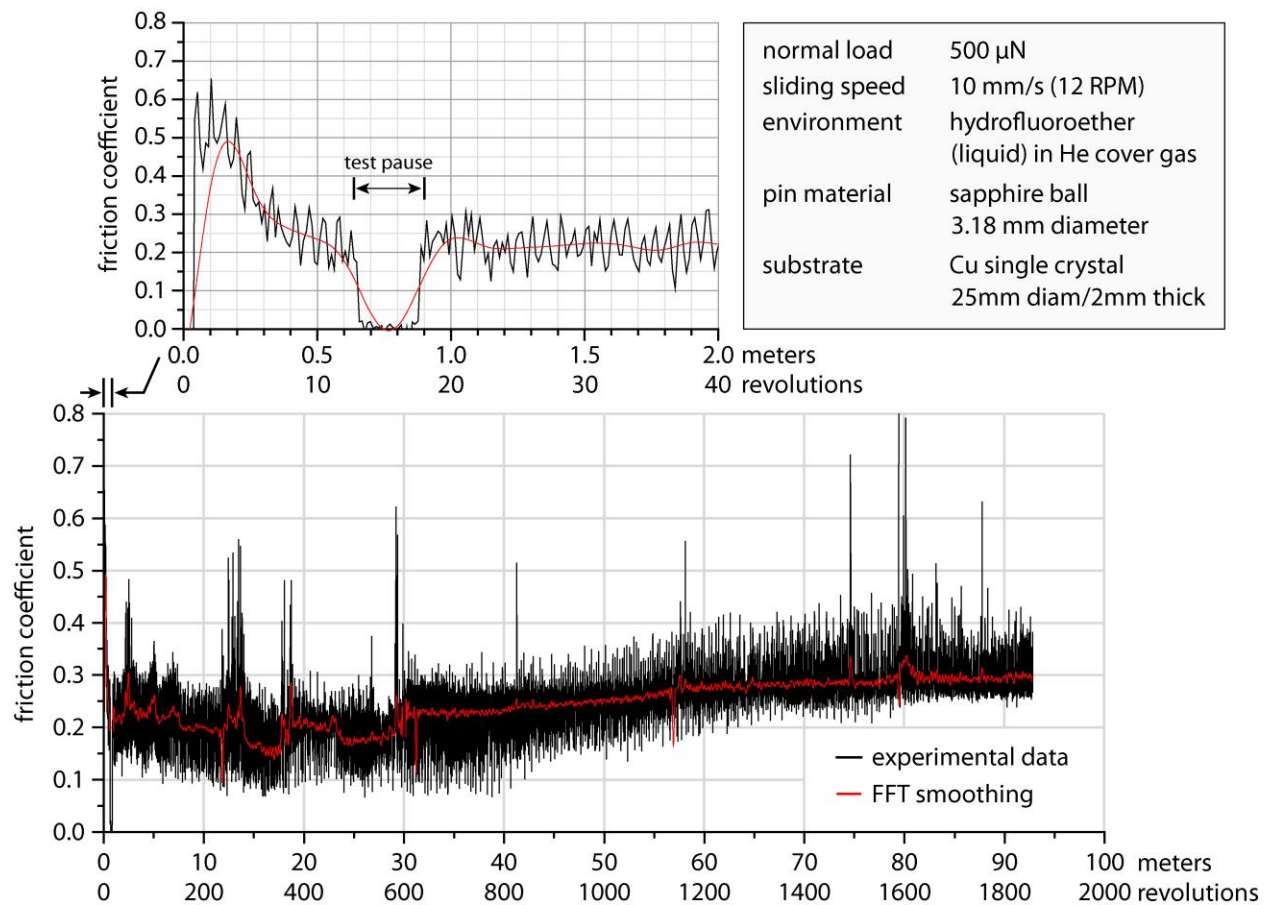


Figure 4-5. Friction coefficient data (raw data in black and FFT low-pass filtered data with a 0.05 Hz cutoff in red) as a function of sliding distance and disk revolutions; the bottom plot shows the full length of the experiment (92 m of sliding) and the top plot shows the initial 2 m or 40 revolutions of data highlighting an initial period of relatively high friction lasting approximately 10 revolutions, possibly due to the presence of a native cuprous oxide.

The initial period of relatively high friction may be due to the presence of a native oxide layer which is worn in the initial 10 cycles of sliding, followed by a prolonged period of relatively lower friction of $\mu \sim 0.2$ possibly corresponding to contact between the alumina pin and the bulk copper substrate. This hypothesis appears to be in agreement with the data reported in the previous sections of this chapter for amorphous alumina sliding on polycrystalline copper substrates in various oxide enhancing and reducing/dissolving agents; the initial higher friction

period is comparable to friction data in 0.1M sodium carbonate and the initial period of sliding in 3wt% H₂O₂.

Figure 4-6 presents scanning electron microscope (SEM) micrographs of the worn single crystal copper substrate surface and bright-field transmission electron microscope (TEM) micrographs showing subsurface deformation along the centerline of the wear track. The cross-sectional lift-out presents near surface deformation due to sliding contact at the conclusion of the experiment shown in Figure 4-5, and reveals regions of dislocation pile-up and step surface features, and no recrystallization. Also visible is what appears to be a layer of residue between the carbon coating applied to protect from ion beam damage during ion milling and the bulk copper material, possibly a residue remaining from immersion in the HFE liquid medium.

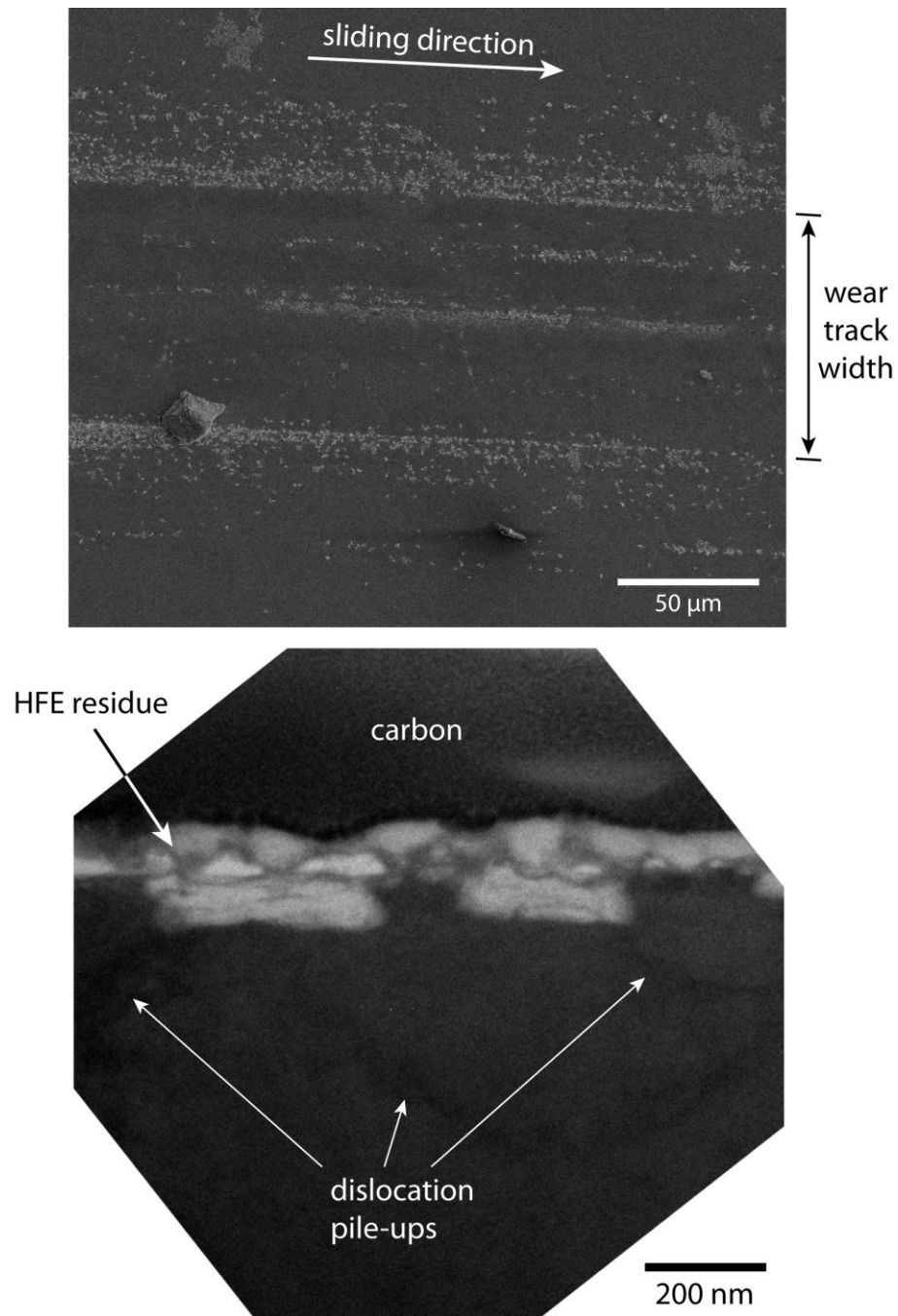


Figure 4-6. SEM micrograph of subsurface friction damage on a single crystal copper substrate sliding against alumina in HFE. (A) SEM micrograph of wear track surface on the single crystal copper substrate after 100 m of sliding. (B) Bright field TEM micrograph of a cross-sectional liftout along the centerline of the wear track; the TEM cross-section is orthogonal to the sliding direction so that sliding is into the plane of the image.

Experimental Investigation of the Role of Electrochemically Enhanced Oxidation on the Wear Rate of Copper Sliding Electrical Contacts at High Current Density

Metal Fiber Wear Rates

The wear rate of the copper fiber sliding submerged in hydrofluoroether was approximately $2 \times 10^{-5} \text{ mm}^3/\text{N}\cdot\text{m}$ and was insensitive to the sustained passage of DC electrical current through the junction up to a density of $442 \text{ A}/\text{cm}^2$ based on the $120 \text{ }\mu\text{m}$ diameter copper fiber cross-sectional area (or more than $2,300 \text{ A}/\text{cm}^2$ based on the worn contact area periodically measured *ex situ* with SWLI). The wear rate of the metal fiber sliding submerged in 3wt% H_2O_2 was an order of magnitude greater, at approximately $3 \times 10^{-4} \text{ mm}^3/\text{N}\cdot\text{m}$. The wear rate of the metal fiber sliding submerged in ultrapure water without electric current flow was also an order of magnitude higher than the case of hydrofluoroether, and was sensitive to the addition of an electrical current load through the contact. A 5 V voltage applied to the sliding contact (with a line resistance of $100 \text{ }\Omega$) caused a 2x increase in wear rate and a gradual increase in contact resistance from about $10 \text{ }\Omega$ to $68 \text{ }\Omega$. The wear rate returned to its original value after a period of sliding without current.

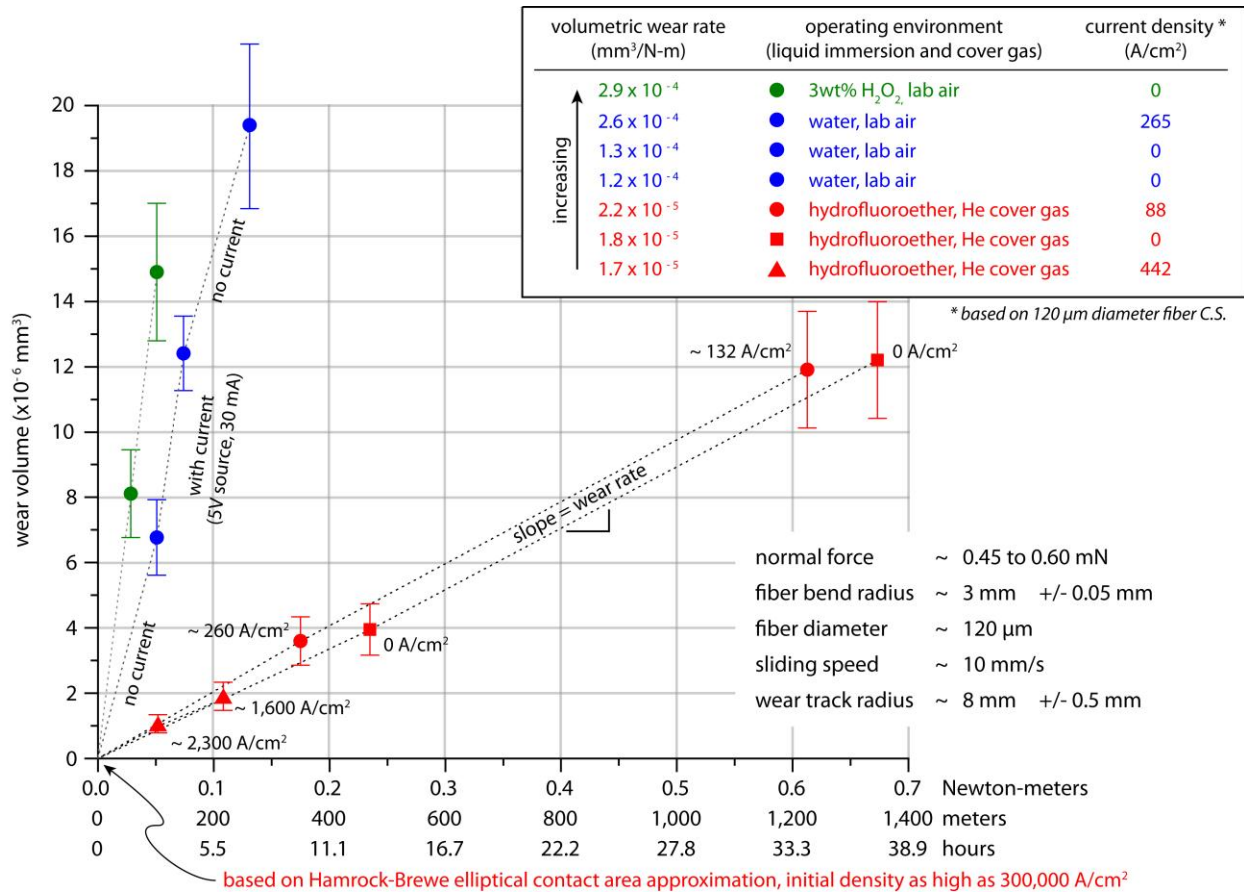


Figure 4-7. Plot of volume loss of the toroid metal fiber (the plot ordinate) as a function of the product of applied normal load and sliding distance, the sliding distance, and the sliding time for seven experiments; the table on the bottom right of the plot shows operating parameters in common for all experiments (note that where a range of values is shown it represents measured variation of the parameter and not the measurement error); the table on the top right summarizes the specific wear rates for the various environments and current densities (based on the nominal fiber cross-section); the current density values shown next to each data point for the hydrofluoroether experiments were based on the measured area of the wear scar on the fiber at that instance in the experiment.

Friction and Contact Resistance

Friction coefficient and contact resistance results are shown in Figure 4-8; the plots comprise full data sets. For a linear sliding speed of 10 mm/s the total duration of a test lasting 100/200/1,000 meters of sliding corresponds to 2.8/5.5/27.8 hours of test duration. Average

friction coefficient and contact resistance values are calculated for periods of relatively steady-state operation, each of which is demarked with arrows in Figure 4-8.

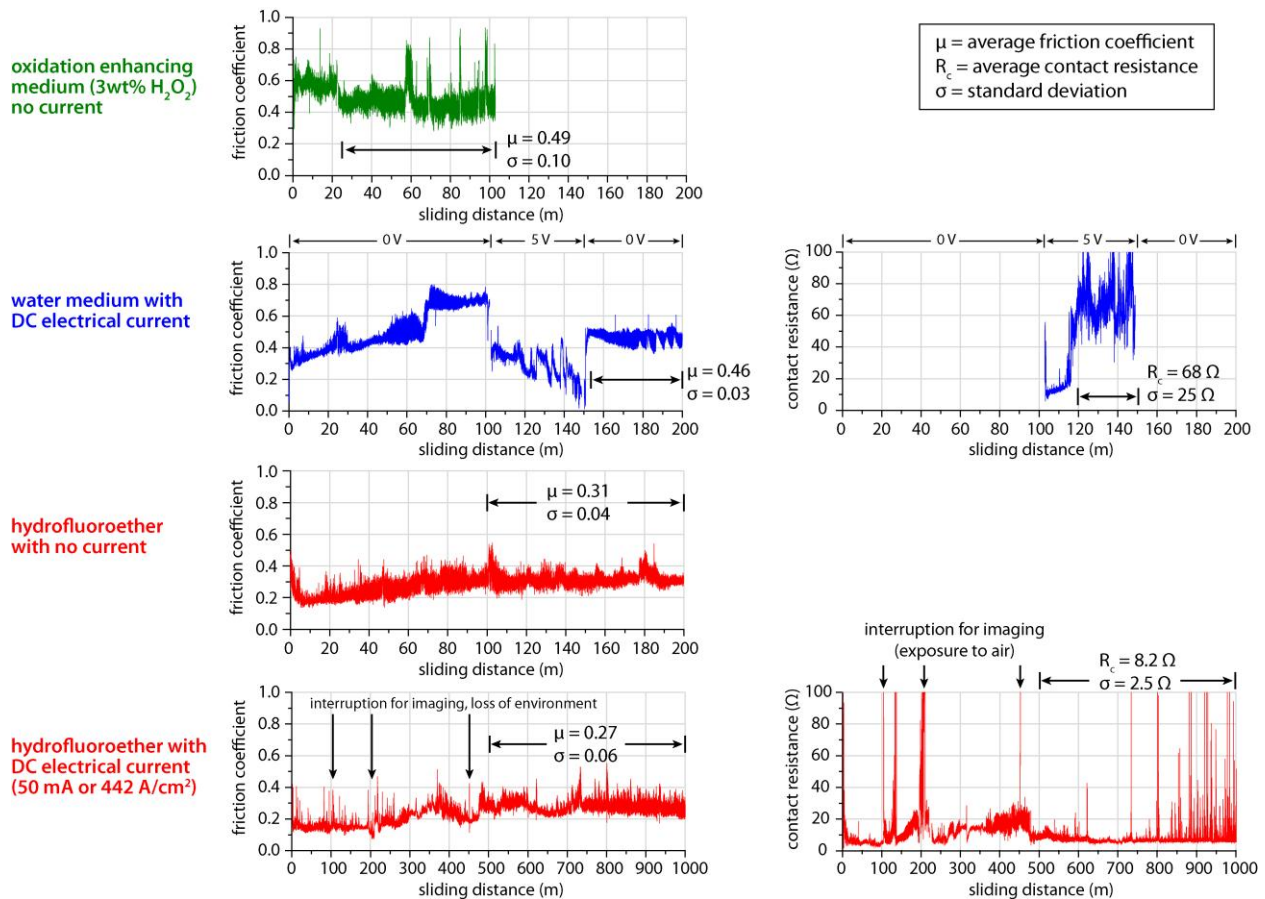


Figure 4-8. Full data sets for friction coefficient and contact resistance (Ohms) vs sliding distance (meters) for four experiments with the common theme of using a single toroid shaped Cu-Be fiber as the pin (120 μm diameter, ~ 3 mm bend radius) sliding on a polished rotating Cu counterface (average roughness ~ 15 nm), with a linear sliding speed of 10 mm/s (wear track radius ~ 8 mm, counterface rotation speed 12 RPM), and an average normal load of 0.53 mN; the sliding contact was submerged in the liquid medium stated above each plot, and where indicated an DC electrical current was passed through the contact using an applied constant voltage of 5 V through a total circuit resistance consisting of a 100 Ω line resistance + contact resistance (R_c).

For the case of sliding while submerged in ultrapure water the friction coefficient gradually increases during the first 100 m of sliding (~ 2.8 hours). Upon applying DC current through the contact there is a sharp drop in friction coefficient that appears to correlate to the

increasing contact resistance, likely due to an electrochemical interaction at the contact. Contact resistance at the onset of electrical current flow was similar in magnitude to the steady-state value observed for the case of hydrofluoroether particularly following the brief exposure of the pin and counterface to lab air during imaging (allowing natural oxidation to occur on otherwise oxide free surfaces operating in hydrofluoroether). A nearly order of magnitude higher contact resistance was observed after prolonged operation in water. This is in contrast to operation in hydrofluoroether. Friction coefficients in hydrofluoroether were $\mu \sim 0.3$, and in oxidative mediums (ultrapure water and 3wt% H_2O_2) $\mu \sim 0.5$.

CHAPTER 5 DISCUSSIONS

Chapter Summary

This chapter is divided into three major sections. The first section is a discussion of the tribological measurements presented in Chapter 4, providing comparisons to other published experimental data for similar tribological systems. The second section presents a conceptual model for what is hypothetically the dominant mechanism of wear for low wear non-noble metal sliding contacts. A discussion of some limitations and the boundary of applicability are also provided. The third section provides a discussion of developments that have been the topic of recent publications and provide further insight as to the atomistic mechanisms governing the wear of non-noble metal sliding contacts, including discussions on grain boundary sliding, dislocation trapping near a sliding interface and the correlation to increased subsurface stress, and the inverse Hall-Petch effect.

Interpretation of Measured Data and Remarks

Sliding Experiments with Alumina on Copper

Takadom [79] observed steady-state friction coefficients for alumina spheres sliding on polycrystalline copper disks in 20 to 90% relative humidity in the range $\mu \sim 0.3$ to 0.4, consistent with experimental results reported in this manuscript for sliding of alumina on copper where a native Cu_2O was the primary composition of the reacted surface layer (a $\mu \sim 0.4$ to 0.5 was observed for the potentiostat controlled experiments, also similar to the initial period of sliding in the electrically unassisted 3wt% hydrogen peroxide sliding experiments). However, Takadom performed sliding experiments at a four-fold greater contact pressure than the experiments described in Chapter 4, arguably the reason for the relatively lower friction coefficient values as a result of gross plastic deformation and consequent fracturing of the surface oxide leading to

partial exposure of bulk copper. Hiratsuka et al. [80] reported a friction coefficient for sapphire on polished polycrystalline copper of $\mu \sim 0.05$ in vacuum (in the absence of an oxide) and $\mu \sim 0.8$ in a cover gas mixture of 20/80% oxygen/argon, also at relatively high contact pressure; they observed a transfer film of oxidized copper on the alumina pin for the case of sliding in an 20% oxygen cover gas not present after sliding on copper in vacuum.

For the same experiments with alumina on copper Hiratsuka et al. [80] also found that wear of the copper substrates in vacuum was below their measurement threshold, but with the addition of 20/80 percent oxygen/argon cover gas the specific wear was at least one order of magnitude higher at $K_{vol} \sim 5 \times 10^{-6} \text{ mm}^3/\text{N}\cdot\text{m}$. The order of magnitude disparity in wear of copper substrates in sliding contact was not sensitive to a change in pin composition (such as ZrO_2 and SiO_2), providing indirect evidence that the variation in wear rate is primarily a function of oxide formation and subsequent wear.

An attempt to measure volumetric wear of the copper disks after sliding against alumina pins was made using a scanning white light interferometer (SWLI), though measurements revealed only a roughened surface inside the wear tracks after as much as 100 m of sliding distance (2000 revolutions) at the relatively low contact pressures implemented. It was not possible to make a statistically significant measurement of disk wear using SWLI.

In summary, friction studies of alumina on polycrystalline copper as a function of oxide composition at relatively low contact pressures and sliding speed reveal three general friction coefficient regimes which are a function of the prevalent surface layer species. Alumina on bare copper exhibited a friction coefficient $\mu \sim 0.2$, alumina on copper with a predominately native oxide composition of Cu_2O exhibited a friction coefficient in the range $\mu \sim 0.4$ to 0.5 , and alumina on copper with a surface layer composition including the high temperature oxide (CuO)

and copper hydroxide/copper carbonate ($\text{Cu}(\text{OH})_2$ and CuCO_3) species exhibited a friction coefficient in the range $\mu \sim 0.8$ to 0.9 . These reference friction values aided in the interpretation of friction behavior of sliding experiments with sapphire on single crystal copper immersed in the oxidation inhibiting HFE liquid medium. Based on the transition in measured friction coefficient from $\mu \sim 0.5$ to $\mu \sim 0.2$ it is argued that (1) contact between the sapphire ball and the copper substrate was achieved and that the HFE lubricant was effectively displaced by the slider at the point of contact and (2) that oxidation was effectively inhibited by the HFE liquid with helium cover gas as evidenced by the immediate drop in friction coefficient in the first four cycles of sliding, attributed to the removal of the native oxide through wear.

Subsurface Frictional Deformation of the Copper Single Crystal Counterface

A representative cross-sectional lift out of the worn single crystal copper substrate was imaged using TEM and presented in Figure 4-6. The micrograph reveals two interesting features: the apparent pile-up of dislocations and the presence of stepped features on the worn surface. This result is consistent with the work presented by Shen et al. [25] and Nazarenko et al. [62] where they observed the appearance of steps on the worn surface of single metal crystal specimens after sliding contact. In 1967 Barquins et al. [81] published results of friction experiments with an alumina ball on a single crystal of copper where they applied a relatively large contact pressure (approximately 3 N on a 1 mm diameter, corresponding to a maximum Hertzian contact pressure of $p_{max} \sim 3$ GPa) and laterally displaced the ball in contact by 100 μm . They subsequently cross-sectioned the copper substrate and observed the emergence of slip bands and voids in the subsurface; an adapted reproduction is presented in Figure 5-1.

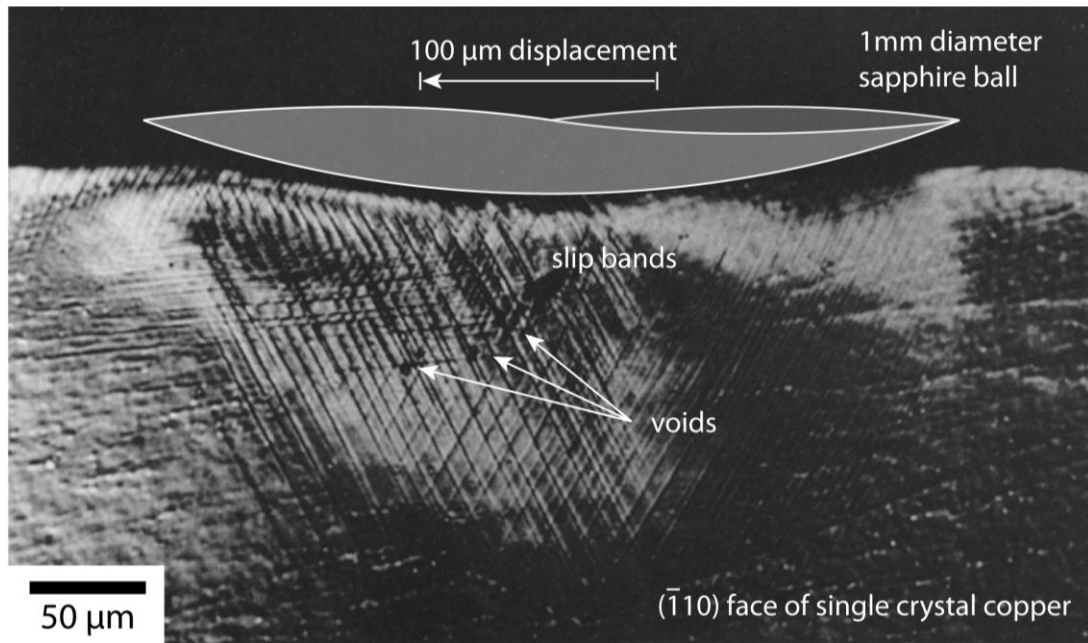


Figure 5-1. Cross-section of a copper single crystal specimen after a single uni-directional pass with a 1 mm diameter sapphire ball (right to left) showing subsurface deformation due to frictional sliding adapted from Barquins et al. [81]; voids and slip bands are observed near surface where sliding contact occurred. Reprinted from Wear, Vol. 11, Issue 2, Barquins, M., Kennel, M., Courtel, R., *Comportement de Monocristaux de Cuivre sous l'action de Contact d'un Frotteur Hemispherique*, pp 87-110, © 1968, with permission from Elsevier.

The subsurface damage shown in Figure 5-1 agrees with the hypothesis that the absence of a hard passivation film on the sliding surface allows dislocations to propagate to the surface and relieve strain energy due to plastic deformation as a result of frictional sliding. The approximately 20 nm thick steps observed in Figure 4-6 may correspond to slip planes in the bulk copper as a result of cyclic sliding against a lightly loaded sapphire ball. This evidence, along with the discussion provided in Section 5.3, provides evidence of the detrimental role of passivation films on the surface fatigue strength of a metal surface due to trapping of dislocations. A more elaborate discussion of this mechanism is provided in the ensuing sections.

Sliding Experiments with a Beryllium Copper Single Fiber on Copper Substrates

It was demonstrated that copper sliding electrical contacts operated immersed in oxidation inhibiting hydrofluoroether (where the metal fiber was in an anode configuration, the case of enhanced wear) did not exhibit a strong correlation between current density, oxide growth rate, and wear rate. In contrast, it was also shown that in otherwise equivalent experimental conditions where the oxidation inhibiting medium was replaced with an oxidative medium (water exposed to lab air), there was a strong correlation between current density, oxide growth rate, and wear rate. Further evidence of the interdependence between wear rate and oxidation rate was shown by substituting enhanced electrochemical oxidation by simple chemically enhanced oxidation. It was shown that copper sliding contacts sliding in a weak solution of hydrogen peroxide exhibit a greater wear rate than the same contacts in water, and approximately the same wear rate as in water with the addition of a relatively large electrical potential driving current transport.

Measured wear rates for the copper-beryllium fiber were more than an order of magnitude greater than the wear rate of a comparable macroscopic system, the first being approximately $2 \times 10^{-5} \text{ mm}^3/\text{N-m}$ and the latter on the order $7 \times 10^{-7} \text{ mm}^3/\text{N-m}$ [64]. The discrepancy is likely due to a difference of scaling; the points of contact on a multi-fiber sliding metal brush are continuously changing and are distributed over a relatively larger contact area as the fibers move and come into and out of contact with the slip-ring, consequently spreading wear damage over a larger area. The ratio of real to apparent area of contact for the single metal fiber experiment is arguably closer to one by more than an order of magnitude [36], practically approaching a Hertzian type contact.

Steady-state contact resistance values for a single beryllium copper fiber sliding on a copper disk immersed in HFE were approximately $R_c \sim 8.2 \Omega$. In order to facilitate a

comparison with macro-scale multi-fiber brush systems [2, 11, 14, 43, 64, 82] a simple parallel resistor calculation may be implemented. Assuming that many such fibers are in contact in parallel all with a contact resistance of 8.2Ω , and given that the loading conditions for the single fiber experiments were proportional to the macro-scale conditions in [43, 64], the approximate contact resistance of a multi-fiber brush with 1,000 fibers in contact would be $R_{eq} \sim 8.2 \text{ m}\Omega$. It should be noted that the calculated line resistance contribution to the measured contact resistance, for a $120 \mu\text{m}$ diameter copper beryllium fiber ($\rho \sim 10.1 \mu\Omega\text{-m}$) about 0.2 m in length, was $R_{line} \sim 1.8 \Omega$ and on the order of the measured contact resistance. It was not possible to measure the fraction of measured contact resistance originating from the pick-up brush sliding contact. The pick-up brush was made up of five fibers in contact with the rotating copper disk. Assuming that each of the five pick-up brush fibers and the single beryllium-copper fiber all contributed equally to the total measured contact resistance, the individual resistance of the single fiber brush contact is $5/6$ of the measured contact resistance. This calculation was based on parallel and series resistance and implies that the actual contact resistance between the beryllium-copper fiber and the copper disk is an additional 16.7% lower than the measured and reported contact resistance. Even after accounting for these contributions, and estimating the contact resistance of the single fiber brush to be $\sim 5.3 \Omega$, it is difficult to argue that the contact is a perfectly metal-metal contact. An order of magnitude assessment of the constriction resistance [41] for a perfectly clean copper on copper contact suggests that the contact resistance should be on the order of $10^{-3} \Omega$. A possible explanation, and on that was previously discussed by Holm [10] and Kuhlmann-Wilsdorf [2], is that the contacting asperities may be separated by a few monolayers of water (or HFE). For separation distances below about 10 nm the primary form of electron transport across the film would then be through electron tunneling rather than

conduction. On a similar thread, as the roughness of the surfaces in contact is typically more than an order of magnitude greater than the proposed contact separation due to adhesion or trapping of liquid molecules between the asperities as they come into and out of contact, macroscopic hydroplaning is not taking place. That is, interlocking of asperities likely remains the dominant contact mechanism, with occasional metal-metal contact. Indirect evidence exists in the measured friction coefficient of $\mu \sim 0.2$. Friction coefficients due to boundary lubrication would be an order of magnitude lower. At the same time, a perfect metal-metal contact (in the absence of a passivating oxide film) would exhibit a two order of magnitude lower contact resistance.

Electrochemically Enhanced Delamination Wear

Proposed Conceptual Model

It is proposed that for lightly loaded (low contact energy) non-noble metal sliding electrical contacts at elevated current densities there is a correlation between surface fatigue wear (delamination) and electrochemical oxidation; more specifically, that the rate of delamination wear is exacerbated by the presence of thicker oxides, and that the electrochemically enhanced/inhibited rate of oxide growth may be coupled to the rate of delamination by a process of dislocation trapping. A proposed conceptual model is presented in Figure 5-2. The model suggests a correlation between the modified oxidation rate mechanism proposed by Boyer et al. [11], the fatigue strength of surfaces in contact, and Suh's delamination wear [58] at high current density in an oxidative medium.

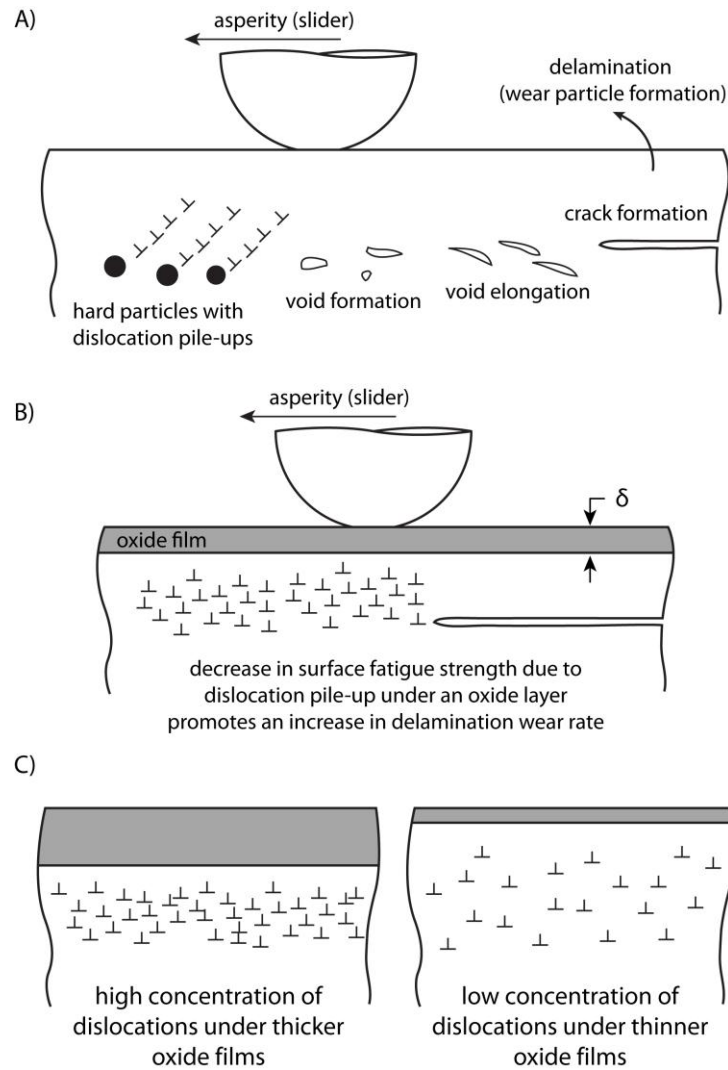


Figure 5-2. Illustration of a proposed conceptual model describing wear of lightly loaded metal sliding electrical contacts correlating (A) the model of delamination wear (adapted from Suh [21, 58]), (B) a reduction in surface fatigue strength due to surface films or oxides as observed by Buckley [29] and Duquette [28], and (C) the phenomenon of dislocation trapping under increasingly thicker surface films or oxides as proposed by Shen et al. [25] and Nazarenko et al. [62], which are correlated to the enhanced/inhibited electrochemical oxidation model proposed by Boyer et al.[11].

The proposed conceptual model is based in large part on the observations of various researchers investigating the mechanisms of metal fatigue, wear, and oxidation in tribo-mechanical systems. In a 1973 publication Nazarenko et al. [62] provided experimental evidence of what they referred to as dislocation trapping under an increasingly thicker oxide film

on a zinc single crystal due to cyclic frictional stress. Using chemical etching and optical microscopy they observed an increase in dislocation density under the friction surface with increasingly thicker oxide films. Buckley [29] observed that relatively ductile gold substrates exhibited surface fatigue cracks due to cyclic frictional stress with the addition of a halide surface film. Duquette [28] performed fatigue tests on nickel single crystals in vacuum, dry air, and humid air and reported a substantial decrease in fatigue strength for specimens exposed to oxidation. Duquette attributes the observed phenomenon to a dislocation trapping model proposed by Shen et al. [25], wherein he proposed that dislocations nucleating near a metal surface due to cyclic stress are inhibited from propagating and relieving at the surface, more so under increasingly thicker oxide films, and that these dislocations would then become trapped and form voids near the metal-oxide interface. An increase in dislocation density near the surface may correlate to a greater rate of sub-surface crack nucleation and propagation. Shen's model was based in part on his own experimental work on fatigue testing of aluminum specimens with varying degrees of prescribed surface film thicknesses. The link between dislocation trapping and wear may exist in the theory of delamination wear proposed and developed by Suh [21, 58], Fleming et al. [22, 59], and Jahanmir et al. [23, 60] in the 1970s. The delamination theory of wear provides a mechanism for the nucleation of subsurface dislocations as a function of frictional stress near a metal friction surface. As a corollary, the depth of maximum shear stress due to contact stress in sliding tends to occur at a depth typically an order of magnitude greater than the thickness of a metal oxide layer, which may explain the observed thickness of wear debris formed from a fatigue process during sliding, exacerbated or alleviated by the electrochemical rate of oxide formation.

Regime of Applicability, Limitations, and Implications

There are numerous competing mechanisms at the interface of a metal sliding electrical contact including abrasive wear [49], adhesive wear [49, 83], delamination wear [21, 84], and electrochemical oxidation [11, 47]. The proposed conceptual model describes what appears to be the dominant mechanism of wear in what could be labeled as high performance non-noble metal sliding electrical contacts, systems operating at current densities high enough to have a detrimental effect on the rate of formation of passivating oxides. The term high performance refers to the condition where nominal contact pressures are more than an order of magnitude below the yield stress of the bulk materials in contact, where the lubricating mechanism does not create a barrier to uninterrupted low contact resistance electrical current transport (i.e. sub-nanometer thick solid lubricant films and/or low viscosity liquid lubricants), and while brush wear rates remain below 1×10^{-6} mm³/N-m for multi-fiber brush contacts.

In cases of high contact stress it is likely that bulk plastic deformation would prevent the buildup of cyclic fatigue damage leading to delamination; wear would likely consist primarily of ploughing and brittle fracture of the oxide film leading to regions of metal-metal contact.

As was shown for the case of copper, when the formation of a passivation film is inhibited by removing the agents necessary for their formation (such as oxygen) it is possible to transport extreme amounts of current density through a metal sliding contact. In this instance the limit of current density may simply be a function of the ability to dissipate thermal energy due to resistive heating of the bulk metal conducting circuit.

Discussions of Interaction Mechanisms and Interfacial Phenomena

Dislocations, Passivation Films, and Cyclic Stresses

In two recent publications by Nicola, one with Van der Giessen and Needleman in 2003 [30] and one also including Xiang and Vlassak in 2006 [31], the group provided experimental

and computational evidence that the presence of a surface passivation layer on copper thin films resulted in the pile up of dislocations and a hardening of the bulk material near the bulk/passivation layer interface. This section provides a summary of their findings and a discussion of the relevance to the tribological behavior of low wear copper sliding electrical contacts.

The authors (Nicola et al. in [30, 31]) limited the scope of their investigation and modeling to thin freestanding copper films of varying thickness with and without passivation layers on one or both side. The thin film specimens were deformed using hydrostatic pressure (bulge test) and were effectively in plane strain (the strips used for experimental work were only thin in the height dimension). The copper films were prepared by sputtering or electroplating, with a thickness in the range 0.5 to 4 μm and grain sizes of 0.5 to 1.5 μm . Titanium films were electroplated on one or both sides in the instances where a passivation film was desired. Figure 5-3 shows an example of an unpassivated copper specimen, and one with a Ti passivation layer after deformation showing a large density of dislocations piled up near the copper/titanium interface.

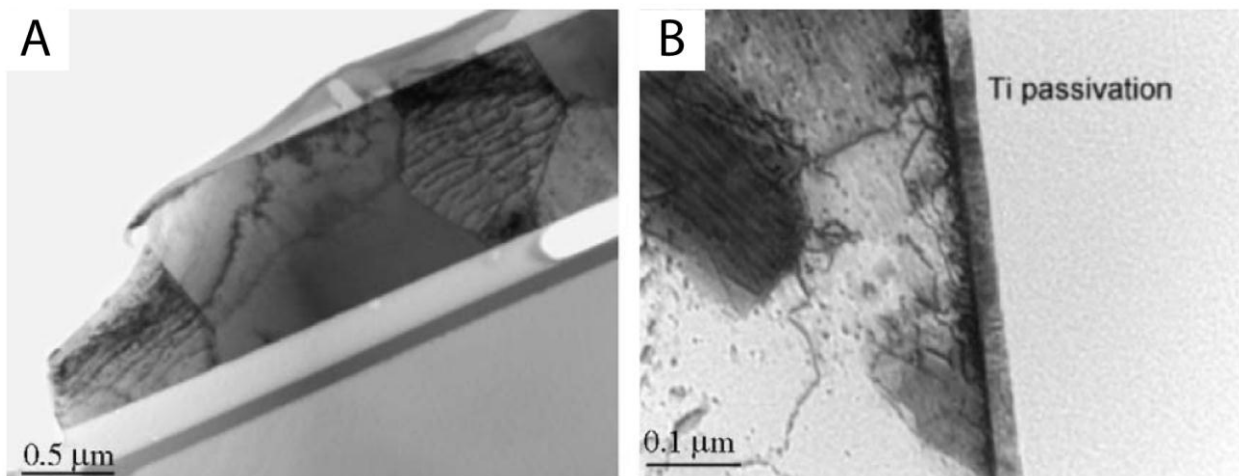


Figure 5-3. TEM cross-sectional micrographs of fatigued freestanding copper thin films showing (A) the typical grain morphology of an unpassivated test specimen, and (B) the

pile up of dislocations in the bulk copper material near a titanium passivated film; figures are reproduced from Nicola et al. [31] (Figure 2). Reprinted from Journal of the Mechanics and Physics of Solids, Vol. 54, Issue 10, Nicola, L., Xiang, Y., Vlassak, J.J., Van der Giessen, E., Needleman, A., *Plastic Deformation of Freestanding Thin Films: Experiments and Modeling*, pp 2089-2110, © 2006, with permission from Elsevier.

The system used in the computational model consisted of an eight grain wide array of planar rectangular grains in plane strain. The numerical results accurately predict the trend in hardening and dislocation pile up for passivated films. Figure 5-4 shows the numerical results [31]. Neither the dislocation pile up nor bulk material hardening were observed in the absence of a passivation film in both the experimental and numerical data. The model also shows that, for the case of an unpassivated film, dislocations do nucleate but are able to exit the grains through the unpassivated surfaces. Consequently, passivation layers restrict dislocation motion (or glide) creating a back stress that inhibits further nucleation of dislocations and results in higher stress values upon re-loading, interpreted as an increase in yield strength or hardening of the material.

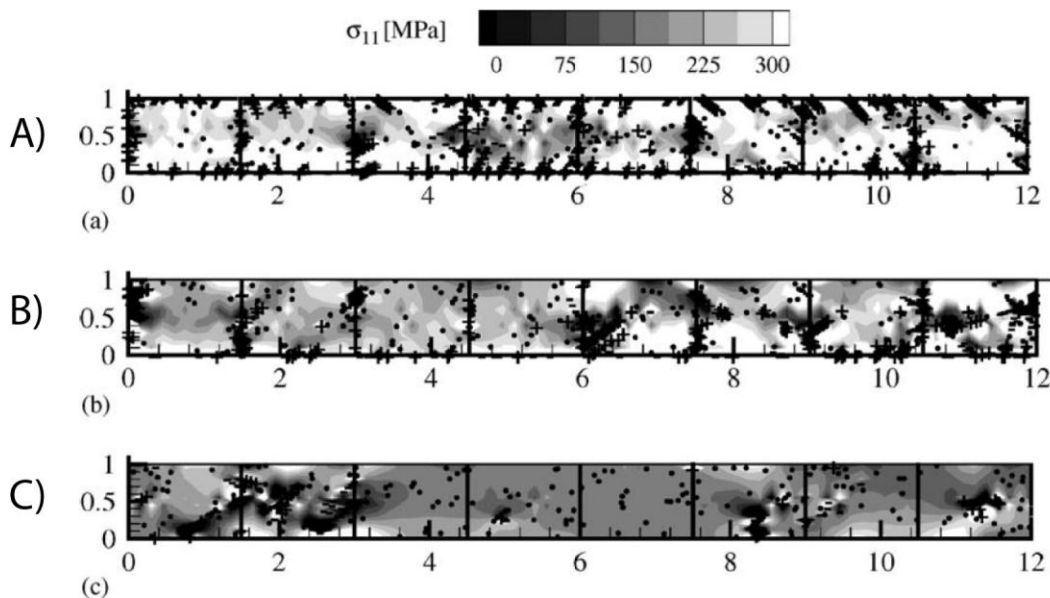


Figure 5-4. Numerical results of principal stress and dislocation distribution for three films of 1 μm thickness consisting of eight grains each, (A) passivated on both sides, (B) passivated on one side, and (C) unpassivated. The figure, reproduced from Nicola et al.

[31] (Figure 8), shows dislocation trapping and internal strain build up due to the presence of passivation films. Solid circles represent Frank-Read sources and +/- symbols represent dislocations. Reprinted from Journal of the Mechanics and Physics of Solids, Vol. 54, Issue 10, Nicola, L., Xiang, Y., Vlassak, J.J., Van der Giessen, E., Needleman, A., *Plastic Deformation of Freestanding Thin Films: Experiments and Modeling*, pp 2089-2110, © 2006, with permission from Elsevier.

The phenomenon of dislocation pile up and consequent buildup of strain energy near a metal/passivation layer (such as an oxide film) observed by Nicola et al. [30, 31], and the computational prediction of strain energy buildup due to inhibition of dislocation gliding, are in remarkable agreement with the Roscoe effect described by Buckley [29]. These observations also provide compelling evidence that, in the absence of a surface film or oxide, a copper sliding electrical contact should be less susceptible to delamination wear as there is a mechanism of energy dissipation through the uninhibited dislocation motion and ability to relieve at a free surface. This mechanism would conceivably be the primary wear mechanism in low pressure sliding metal contacts where oxidation is prevalent and the interface is not undergoing gross deformation during sliding.

Low Friction Metal Contacts, Surface Grain Refinement, and the Inverse Hall-Petch Effect

There are numerous studies investigating subsurface damage due to sliding contact of metals [34, 49, 83, 85-89]. It is evident that the mechanisms of wear are many and their relevance in describing wear of a given system is dependent on the loading conditions and environmental parameters. For example, at high enough contact stresses the surfaces experience gross material deformation and frictional heating, possibly leading to metal-metal contact and subsequent welding of the junction. In this extreme regime of wear the mechanisms of oxidation and fatigue may be irrelevant to a description of wear. For the case of a non-noble metal sliding electrical contact in an oxidative media where typical wear rates are low the processes of oxide formation and fatigue wear (delamination) evidently play a primary, if not dominant, role. The

work described in this section focuses on three interfacial phenomena which may provide greater insight as to the nature of low friction behavior observed in sliding of self-mated copper contacts; these are, near-surface grain refinement, grain boundary sliding, and the inverse Hall-Petch effect.

In a recent publication Prasad et al. [90] investigated the formation of an ultrafine nanocrystalline layer near the surface of worn nickel substrates. They observed a sharp contrast in the friction behavior of nickel substrates (sliding against silicon nitride balls) which appears correlated to the formation of an ultrafine nanocrystalline layer at the surface of the wearing nickel substrate. The formation of this ultrafine grained layer was only observed below a threshold of contact stress and sliding speed. Figure 5-5 shows friction data from experiments with silicon nitride sliding on electrodeposited nickel films, adapted from Prasad et al. [90]. These experiments were performed in a carefully controlled nitrogen cover gas. The transition in friction occurring in the first 50 to 100 cycles is attributed by the authors to wearing through the native oxide film.

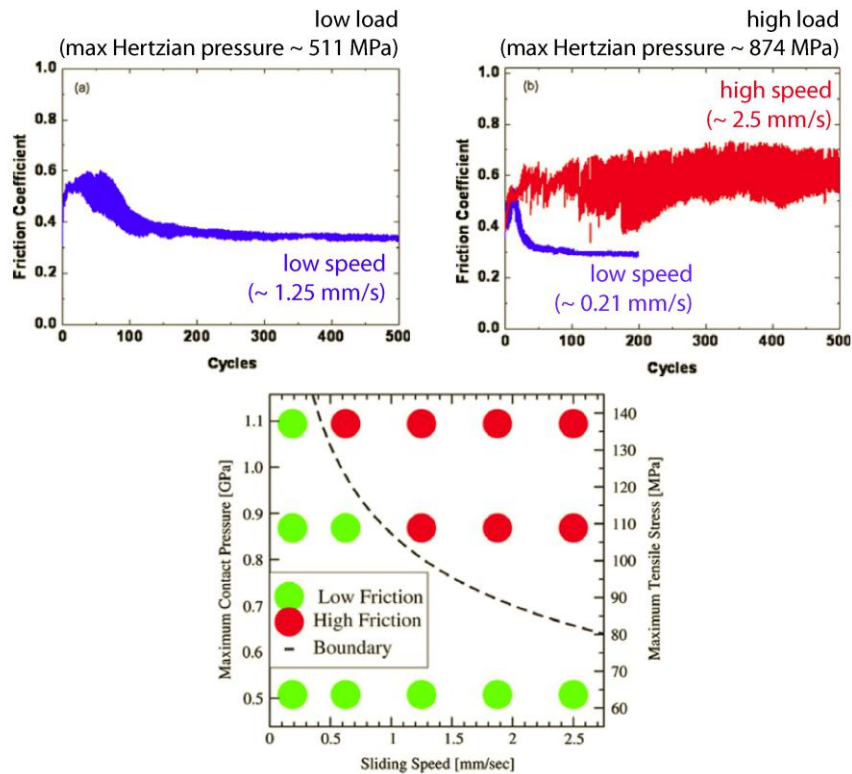


Figure 5-5. Friction data plots from silicon nitride balls sliding on electrodeposited nickel films at varying load and sliding speed, all in a nitrogen cover gas, and friction map showing the load and sliding speed threshold between high friction ($\mu \sim 0.6$) and low friction ($\mu \sim 0.3$); the figures are reproduced from Prasad et al. [90]. Reprinted from Scripta Materialia, Vol. 64, Issue 8, Prasad, S.V., Battaile, C.C., Kotula, P.G., *Friction Transitions in Nanocrystalline Nickel*, pp 729-732, © 2011, with permission from Elsevier.

The cases of low wear were shown to coincide with the formation of an ultrafine nanocrystalline layer with a grain size less than ~ 10 nm. Figure 5-6 presents subsurface cross-sections of worn nickel substrates reproduced from Prasad et al. [90], one example showing the presence of an ultrafine grain layer at the sliding surface (labeled Zone 1) and one showing the absence of Zone 1 from an experiment performed at a sliding speed above the threshold. As an explanation of the observed trend the authors provided the hypothesis that the formation of an ultrafine nanocrystalline layer due to friction induced deformation changes the way the metal surface continues to deform; upon the formation of the observed ultrafine layer the system

switches from dislocation-mediated deformation to grain boundary gliding. They further hypothesize that the observed threshold for the formation of an ultrafine nanocrystalline layer as a function of contact pressure and sliding speed may be a result of high wear, such that the surface layer is removed as wear debris before it can reach a fine enough grain structure to allow the transition to grain boundary sliding.

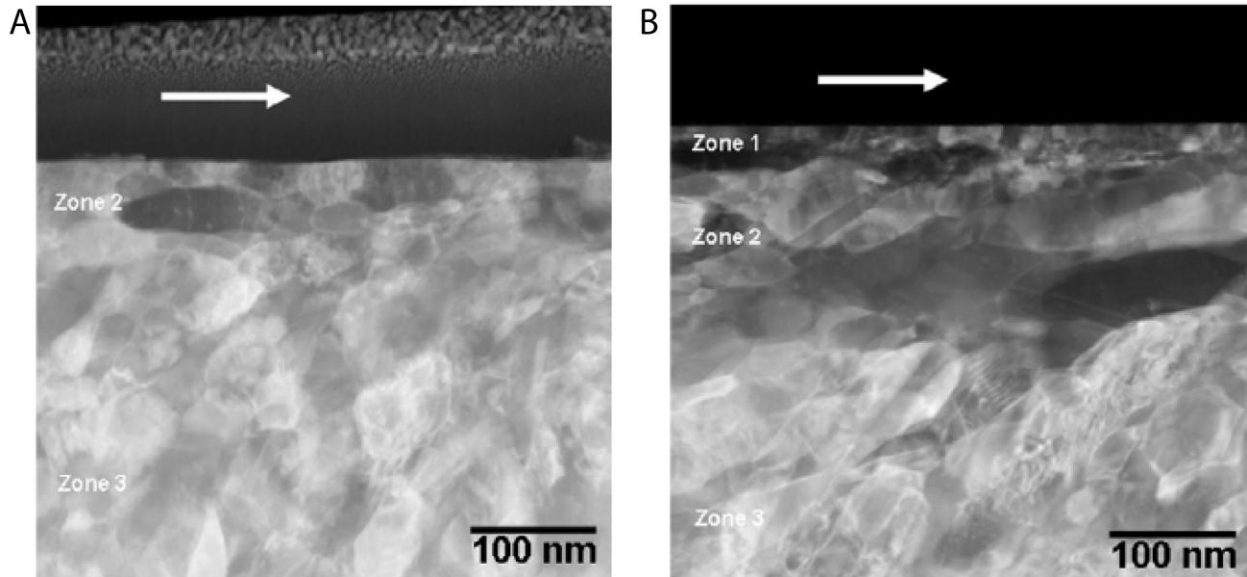


Figure 5-6. Annular dark-field STEM micrographs showing a sub-surface cross-section of worn nickel substrates from sliding contact experiments performed at 874 MPa max Hertzian contact pressure at (A) high sliding speed, ~ 2.5 mm/s, and (B) low sliding speed, ~ 0.21 mm/s; reproduced from Prasad et al. [90]. The zone of ultrafine nanocrystalline grains (Zone 1) is only present in the low speed specimen. Reprinted from Scripta Materialia, Vol. 64, Issue 8, Prasad, S.V., Battaile, C.C., Kotula, P.G., *Friction Transitions in Nanocrystalline Nickel*, pp 729-732, © 2011, with permission from Elsevier.

The hypothesis of a transition to grain boundary sliding in low wear metal sliding systems may explain the low friction behavior observed for copper sliding contacts in the absence of a passivation layer, such as the metal fiber experiments in hydrofluoroether. Raj and Ashby [91] formulated the constitutive equation shown in Equation 5-1 to approximate the shear

rate that can be accommodated by diffusional sliding and creep of grains in a polycrystalline material.

$$\dot{\gamma} = \frac{40 \tau \Omega}{d^2 k T} \left(1 + \frac{\pi \delta}{2d} \frac{D_{gb}}{D_{bk}} \right) D_{bk} \quad (5-1)$$

The engineering shear strain rate ($\dot{\gamma}$) is a function of the local shear stress (τ), Boltzmann's constant (k), temperature (T), the atomic volume (Ω), grain size (d), self-diffusivity at the grain boundaries (D_{gb}), self-diffusivity in the bulk (D_{bk}), and the width of the grain boundary diffusion pathway (δ).

Equation 5-1 implies that the amount of plastic deformation that can be accommodated by grain boundary sliding increases with increasingly finer grain size. Although not readily apparent, an increase in temperature also causes an increase in the ability to accommodate deformation due to the exponential dependence of the diffusivity coefficients to temperature; an increase in temperature causes an increase in D_{bk} and D_{gb} , resulting in a net increase in the max shear rate. Raj and Ashby [91] observed that Equation 5-1 can be interpreted as a shear stress/strain relationship typical of a Newtonian fluid, where the shear rate response of the polycrystalline system is linearly proportional to the applied shear stress and the inverse of viscosity (Equation 5-2). In this case, the viscosity of the polycrystalline film describing grain boundary sliding (η_{gbs}) can be split into two components describing deformation due to diffusion of bulk material within the grains and diffusion of material along grain boundaries.

$$\dot{\gamma} = \frac{1}{\eta_{gbs}} \tau_a$$

where, $\eta_{gbs} = \eta_{bk} + \eta_{gb}$

$$\eta_{bk} = \frac{1}{42} \frac{d^2 kT}{D_{bk} \Omega}$$

$$\eta_{gb} = \frac{1}{132} \frac{d^3 kT}{\delta D_{gb} \Omega}$$
(5-2)

An order of magnitude approximation of the maximum plastic deformation that can be accommodated by a polycrystalline copper substrate through grain boundary sliding was made with values for the self-diffusivity of copper published by Dickenscheid et al. [92], a grain diameter in the inverse Hall-Petch regime of $d \sim 10$ nm, a grain boundary separation on the order $\delta \sim 1$ nm, and an applied shear stress of $\tau_a \sim 100$ MPa at room temperature $T \sim 300$ K. Details of the calculation are shown in an appendix section. The approximate calculated maximum shear strain was $\dot{\gamma} \sim 5.9 \times 10^{-3} s^{-1}$. The ratio of the applied shear stress to strain rate is then a measure of the viscosity of the fine grain film, giving a value of $\eta_{gbs} \sim 17$ GPa-s (as a reference, the viscosity of water at STP is ~ 1 mPa-s). Treating a sliding contact as a 2D laminar flow problem where an ultrafine grained region developed at the interface as shown by Prasad et al. [90], illustrated in Figure 5-7, it is possible to approximate the order of magnitude of interfacial velocity that can be accommodated through grain boundary sliding. For an 50 nm thick ultrafine nanocrystalline layer at the interface of a copper substrate in sliding contact with a slider under the same stress conditions as above the value of max sliding velocity accommodated by grain boundary sliding is approximately $u_{max} \sim 1.3 \times 10^{-14}$ m/s. This result suggests that the role of grain boundary sliding on the friction behavior of polycrystalline metal systems is negligible with respect to macroscopic sliding and the observed transition to low friction behavior. That is, the first order estimate suggests that in the absence of a surface passivation film and with a

consequent grain refinement it is not likely that the sliding contact is gliding as a result of grain boundary sliding. The theory does exhibit strong temperature dependence, such that for the system analyzed here, at temperatures above 600 K grain boundary sliding may fully accommodate sliding speeds on the order of 1 mm/s. A localized increase in temperature on this order may be possible in a sliding electrical contact as a result of resistive heating at high enough current density, plastic deformation due to sliding, and frictional heating at high enough sliding speed/contact pressure. However, these are not applicable factors in the experiments with polycrystalline nickel described by Prasad et al. or the single crystal copper experiments described in this manuscript [90]. It is worth noting that relatively low friction behavior was observed in the case of single crystal copper even though TEM microscopy revealed a single crystal structure at the worn surface. That is, relatively low friction was achieved in the absence of an ultrafine recrystallized layer (Zone 1).

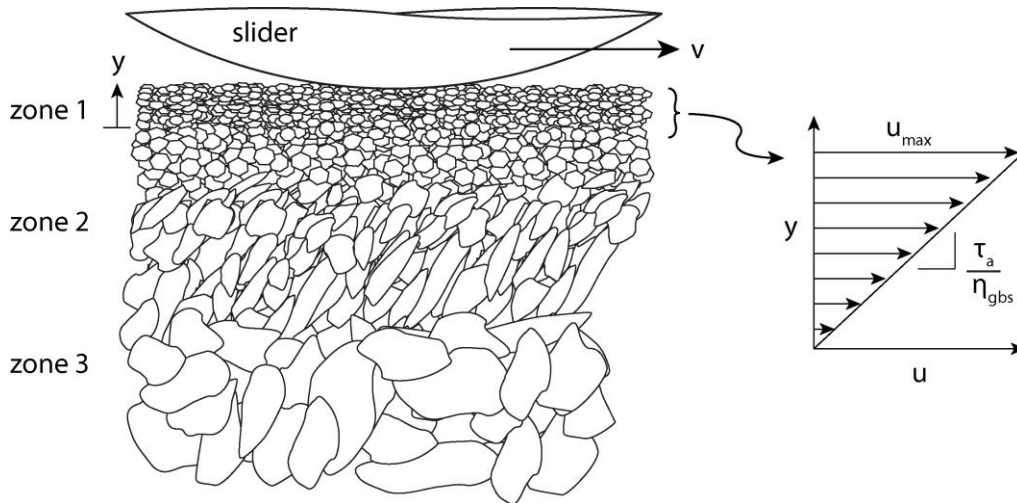


Figure 5-7. Illustration of a 2D cross-section of a sliding contact showing the multi-zone grain recrystallization behavior observed by Prasad et al. [90], and a plot of the velocity gradient as a function of the thickness of Zone 1.

The relatively lower friction coefficient regime ($\mu \sim 0.3$) observed for both nickel and copper is consistent with the calculated resistance to plastic deformation of an unpassivated bulk

metal surface where, as described in Chapter 2, the coefficient of friction is theoretically equal to the ratio of the yield stress to hardness $\mu \cong \frac{\sigma_y}{H}$. For a sphere on plane contact in the absence of hard surface films and accounting for work hardening, as described by Tabor in [39], the hardness is approximately in the range $H \cong 3\sigma_y$ to $5\sigma_y$, corresponding to a friction coefficient in the range $\mu \cong \frac{1}{3}$ to $\frac{1}{5}$ ($\mu \sim 0.2$ to 0.33), consistent with the friction transition observed in the sapphire on single crystal copper experiment reported herein. It is then possible that the higher friction coefficient observed for alumina on nickel may in fact be due to the development of a passivating oxide film at low enough contact pressure and sliding speed (i.e. wear rate vs oxidation kinetics at very low concentration of oxygen in a nominally nitrogen cover gas). High friction in the presence of an oxide film is consistent with the relatively high friction behavior observed for alumina on copper oxide/hydroxide/carbonate.

There is indirect evidence that the presence of an ultrafine nanocrystalline layer at the sliding interface may be correlated to a reduction in friction and possibly wear, although the role of grain refinement is not yet clear. The well documented phenomenon of localized softening of surface material as a result of grain refinement below about 10 nm, known as the inverse Hall-Petch effect, may play a role in localized reduction of contact stress at contacting asperities resulting in an apparent reduction in friction. Schiötz et al. [93] performed 100 million atom molecular dynamics simulations of plastic deformation of nanocrystalline copper and found a cross-over point in the Hall-Petch behavior at a grain size of ~ 12 nm. Below a nominal grain size of 12 nm Schiötz et al. [93] predicts a transition into grain boundary sliding for a polycrystalline copper system, consistent with the friction behavior transition and the presence of an ultrafine crystalline layer observed by Prasad et al. [90]. A second predicted side effect of

grain refinement of copper polycrystalline surfaces to sub 10 nm sizes, as described by Yue et al. in [94], is an increase in electrical resistivity due to electron scattering in the region of high density grain boundaries. This effect may potentially be used as indirect evidence of the formation of a nanocrystalline surface layer in investigations of the phenomenon of surface grain refinement.

CHAPTER 6 CONCLUSIONS AND REMARKS ON CONTINUING RESEARCH

Sliding electrical contact research lies at the intersection of several scientific disciplines and requires considerable fundamental understanding of each to achieve meaningful insight. These systems are typically governed by a complex set of mutually dependent and often antagonistic phenomena including mechanical wear, oxidation (thermally activated diffusion), electrocorrosion, electrostatic adhesion and contact separation by lubricating agents, and electron tunneling. An attempt was made to narrow the field and perform experimental investigations focusing on the phenomenological mechanisms deemed most relevant to the design of more effective metal sliding electrical contacts. Typical design challenges focus on the life of a metal brush (the wear rate) and the ability to transport the largest possible DC electric current density with minimal energy loss at the highest possible sliding speed. Although brushless electrical actuators and generators (both DC and AC) provide remarkably efficient solutions in many engineering applications there are numerous applications for brushed components that could benefit from this research, particularly if it becomes possible to design robust sliding metal contacts capable of continuous transport of 100s or 1,000s A/cm^2 while maintaining wear rates in the same regime as boundary lubricated contacts. The operational simplicity and robustness of brushed DC motors are ideal for large scale power generation applications. Brushed communication slip-rings for satellites and wind turbines, large scale electric motors for ship propulsion, and state-of-the-art commutator design are three examples where design of metal sliding electrical contacts plays a critical role and is often the principal design challenge. The following paragraphs summarize each major result and presented in this manuscript.

Perhaps the most notable conclusion derived from the data is the observed insensitivity to current density (in the range 0 to 442 A/cm^2) on the wear rate of a single fiber beryllium copper

brush sliding electrical contact ($K_{vol} \sim 2 \times 10^{-5} \text{ mm}^3/\text{N}\cdot\text{m}$) when operating in an oxygen free, unreactive liquid medium (hydrofluoroether). This is in contrast to the previously established correlation between the wear and corrosion rates of copper and other oxidation prone materials in oxygenated environments (humid CO_2 , humid N_2 , etc.) at high enough current density.

The friction response of alumina on copper was measured as a response to a prescribed change in passivation film composition using an *in situ* electric potential controlled three electrode cell and a 0.1M sodium carbonate solution. A steady-state friction coefficient $\mu \sim 0.9$ was observed for alumina on copper where the predominate species formed were CuO , $\text{Cu}(\text{OH})_2$, and CuCO_3 . A steady-state friction coefficient $\mu \sim 0.45$ was observed when sliding on predominately Cu_2O .

The nature of low friction ($\mu \sim 0.2$) in low wear copper sliding contacts was investigated. Sliding experiments with sapphire on single crystal copper immersed in hydrofluoroether were followed by characterization of subsurface wear damage on the copper specimens using SEM and TEM. This analysis was used to verify the hypothesis that the formation of an ultrafine polycrystalline zone near the sliding surface, at low enough contact pressures, coincides with low friction. Upon commencing sliding the measured friction coefficient transitioned from $\mu \sim 0.45$ to $\mu \sim 0.2$ in approximately 4 revolutions, with a gradual increase to 0.3 over 1800 revolutions.

Friction experiments with alumina on polycrystalline copper in a chemical cell were performed to both verify the results of the electrochemical experiments and provide additional evidence of the low friction behavior of alumina on copper in the absence of a surface passivating film. Sliding experiments were performed in 3wt% H_2O_2 revealing a transition in friction coefficient from $\mu \sim 0.4$ to 0.9, consistent with the transition from primarily Cu_2O to CuO and $\text{Cu}(\text{OH})_2$ formation found in the literature. Sliding experiments in a 2M acetic acid

solution exhibit a steady-state friction coefficient $\mu \sim 0.18$, also consistent with the continued dissolution of the passivating oxide film and exposure of softer, oxide free bulk copper.

The role of grain boundary sliding as a result of the formation of an ultrafine polycrystalline layer (< 10 nm grain size) near the sliding surface of a low wear metal contact was discussed. Preliminary calculations based on established theoretical models were performed and indicate that the mechanism of grain boundary sliding plays a negligible role in describing observed low friction behavior.

APPENDIX A
DERIVATION OF AN APPROXIMATE EXPRESSION FOR THE VOLUME OF A
TOROIDAL CAP

This section presents a derivation of an approximate (small-angle assumption) solution for the volume of a toroidal cap used to quantify the volumetric wear of sliding metal fibers. Figure A-1 illustrates the geometry, variables, and coordinate axes considered.

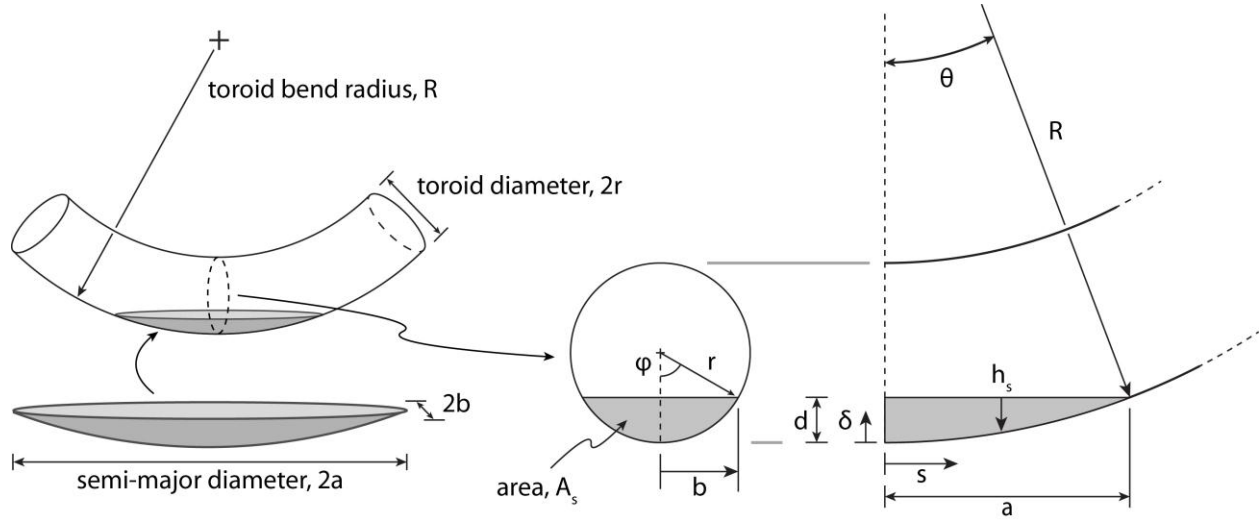


Figure A-1. Geometry of a toroid segment or cap (the shaded volume) corresponding to the wear geometry observed on the metal fibers; the image illustrates coordinate axes and variable definitions implemented in the derivation of an approximate expression for the volume of a toroid section.

Beginning with the trigonometry identities, Equations A-1 (shorthand is used in the remaining derivation to refer to equations, such as A-1 for Equation A-1),

$$R^2 = (R - d)^2 + a^2 \quad R - d = R \cos \theta \quad (\text{A-1})$$

Implementing a Taylor series expansion of the cosine term limited to two terms (based on the *assumption of small angles*),

$$\cos \theta \cong 1 - \frac{\theta^2}{2!} \quad (\text{A-2})$$

Applying A-2 to the right expression in A-1 gives the approximation of A-3.

$$R - d \cong R \left(1 - \frac{\theta^2}{2!} \right)$$

$$d \cong \frac{R\theta^2}{2}$$
(A-3)

Combining the left expression of A-1 with A-3 gives expression A-4.

$$R^2 = (R \cos \theta)^2 + a^2$$

$$R^2 = R^2 \left(1 - \frac{\theta^2}{2!} \right)^2 + a^2$$

$$R^2 = R^2 \left(1 - \theta^2 + \frac{\theta^4}{4} \right) + a^2$$
(A-4)

The fourth order term is dropped by again invoking the assumption of small angles. By combining A-3 and A-4 and simplifying the expressions A-5 are derived.

$$\theta \cong \frac{a}{R} \quad d \cong \frac{a^2}{2R}$$
(A-5)

Now considering the geometry created by the plane cutting a fiber cross-section, the previous steps are repeated to derive A-6 for the range of values $0 \leq s \leq a$.

$$\theta \cong \frac{s}{R} \quad \delta_s \cong \frac{s^2}{2R}$$
(A-6)

The following equality is implemented to arrive at the expression correlating h_s and the parameters a , s , and R , shown in A-7.

$$h_s + \delta_s = d \quad \rightarrow \quad h_s = \frac{a^2 - s^2}{2R}$$
(A-7)

Referring to the circular cross-section illustrated in Figure A-1 B, expression A-8 is derived for the cross-sectional area A_s corresponding to a slice of the worn toroidal segment. Note that the small angle approximation is once again invoked, such that the cross-section is

assumed to be circular for all values of s , neglecting the fact that with increasing s the circular cross-section will become an ellipse.

$$\frac{A_s}{2} = \pi r^2 \frac{\varphi}{2\pi} - \frac{1}{2} h_s r \cos \varphi \quad (\text{A-8})$$

Similar to the derivation for A-5, the expressions of A-9 are derived again assuming small angles for the values of φ .

$$\varphi \cong \frac{b}{r} \quad h_s \cong \frac{b^2}{2r} \quad (\text{A-9})$$

A-8 is reduced using A-9, arriving at A-10.

$$\begin{aligned} \frac{A_s}{2} = \frac{br}{2}(1 - \cos \varphi) &\rightarrow \frac{A_s}{2} \cong \frac{br}{2} \left(1 - 1 + \frac{b^2}{2r}\right) \\ \text{or } \frac{A_s}{2} &\cong \frac{b^3}{4r} \end{aligned} \quad (\text{A-10})$$

Combining A-9 and A-10 and simplifying, the expression A-11 is derived, which is notably not a function of b .

$$\frac{A_s}{2} \cong \frac{h_s}{2} \sqrt{2rh_s r} \quad (\text{A-11})$$

The approximate volume of the segment is then calculated by integration of A-11, arriving at A-12.

$$\begin{aligned} V_{loss} &= 2 \int_{s=0}^a 2 \left(\frac{A_s}{2} \right) ds \rightarrow V_{loss} \cong 2 \int_{s=0}^a h_s \sqrt{2rh_s} ds \\ V_{loss} &\cong \frac{1}{R} \sqrt{\frac{r}{R}} \int_{s=0}^a (a^2 - s^2) ds \\ \text{or } V_{loss} &\cong \frac{3\pi}{16} \frac{a^4}{R} \sqrt{\frac{r}{R}} \end{aligned} \quad (\text{A-12})$$

The small angle approximation results in an under-estimation of the volume calculation of A-12. This error is quantifiable for the special case of A-12 where $r = R$ (a spherical cap).

The adjusted expression A-13 provides greater accuracy.

$$V_{loss} \cong \frac{\pi a^4}{4 R} \sqrt{\frac{r}{R}} \quad (\text{A-13})$$

The accuracy of A-13 increases with increasingly smaller values for the ratio a/R , a characteristic of the toroidal geometry (e.g. for $R = 3.0$ mm, $a = 100$ μm , $r = 60$ μm , $a/R = 0.033$ and $r/R = 0.02$). For the special case of a spherical cap where $r/R = 1$ and $a/R = 0.1$, the error due to a small angle assumption is quantifiable and equal to 0.3%.

APPENDIX B GRAIN BOUNDARY SLIDING

This section provides a description of grain boundary sliding and the calculations of accommodation by diffusion based on the constitutive equations and analysis published by Raj and Ashby in [91]. Equation B-1 provides a constitutive equation correlating shear rate accommodation by grain boundary sliding to system and material specific parameters.

$$\dot{\gamma} = \frac{40 \tau \Omega}{d^2 k T} \left(1 + \frac{\pi \delta D_{gb}}{2d D_{bk}} \right) D_{bk} \quad (\text{B-1})$$

The equation defines the engineering shear strain rate ($\dot{\gamma}$ in s^{-1}) as a function of the local shear stress (τ in Pa), Boltzmann's constant ($k \sim 1.380 \times 10^{-23}$ J/K), temperature (T in K), the atomic volume (Ω in m^3), grain size (d in m), self-diffusivity at the grain boundaries (D_{gb} in m^2/s), self-diffusivity in the bulk (D_{bk} m^2/s), and the width of the grain boundary diffusion pathway ($\delta \sim 1$ nm).

The atomic volume (Equation B-2) is the volume defined by the van der Waals radius, a material property.

$$\Omega = \frac{4}{3} \pi r_{vdw}^3 \quad (\text{m}^3) \quad (\text{B-2})$$

For copper, with a van der Waals radius $r_{vdw} \sim 0.140$ nm [95], the atomic volume is $\Omega \sim 0.0115$ nm^3 . The diffusion coefficient is a measure of the mobility of a particle through a medium and has units of m^2/s . For the special case of a particle moving through a medium composed of the same particles the coefficient of diffusion is referred to as the coefficient of self-diffusion, such as for copper moving through a bulk copper lattice (D_{bk} , Equation B-3) or copper moving along the surface of a grain boundary (D_{gb}).

$$D_{bk} = v_o \lambda^2 A \exp\left(-\frac{\Delta H_d}{kT}\right) \quad (\text{m}^2/\text{s}) \quad (\text{B-3})$$

The bulk diffusion coefficient in a solid is then linearly a function of the characteristic vibration frequency ($\nu_o \sim 10^{13}$ Hz), the distance between adjacent jump or interstitial sites (λ), a configurational entropy term (A), and inverse exponentially a function of thermal energy (kT) and the activation enthalpy for diffusion (either ΔH_d in J or Q in eV). The inverse exponential temperature dependence plays a dominant role in the shear rate calculation due to grain boundary sliding. Typically the pre-exponential terms are lumped into a relatively unvarying system specific coefficient ($D_o = \nu_o \lambda^2 A$) sensitive to whether diffusion occurs in the bulk, along a grain boundary, or at a free surface. Table B-1 provides measured values for copper and is a reproduction from a publication by Dickenscheid et al. [92].

Table B-1. Values of pre-exponential factor D_o and activation enthalpy Q for copper self-diffusion through a nanocrystalline volume, a bulk lattice, along a grain boundary, and along a free surface; the data is reproduced from Dickenscheid et al. [92].

System	D_o (m ² /s)	Q (eV) ^a
Nanocrystalline	3×10^{-9}	0.69
Lattice	2×10^{-5}	2.04
Grain Boundary	1×10^{-5}	1.08
Free Surface	1×10^{-7}	0.69

^a The activation enthalpy in joules is $\Delta H_d \sim \left(1.602 \times 10^{-19} \frac{\text{J}}{\text{eV}}\right) \cdot Q$

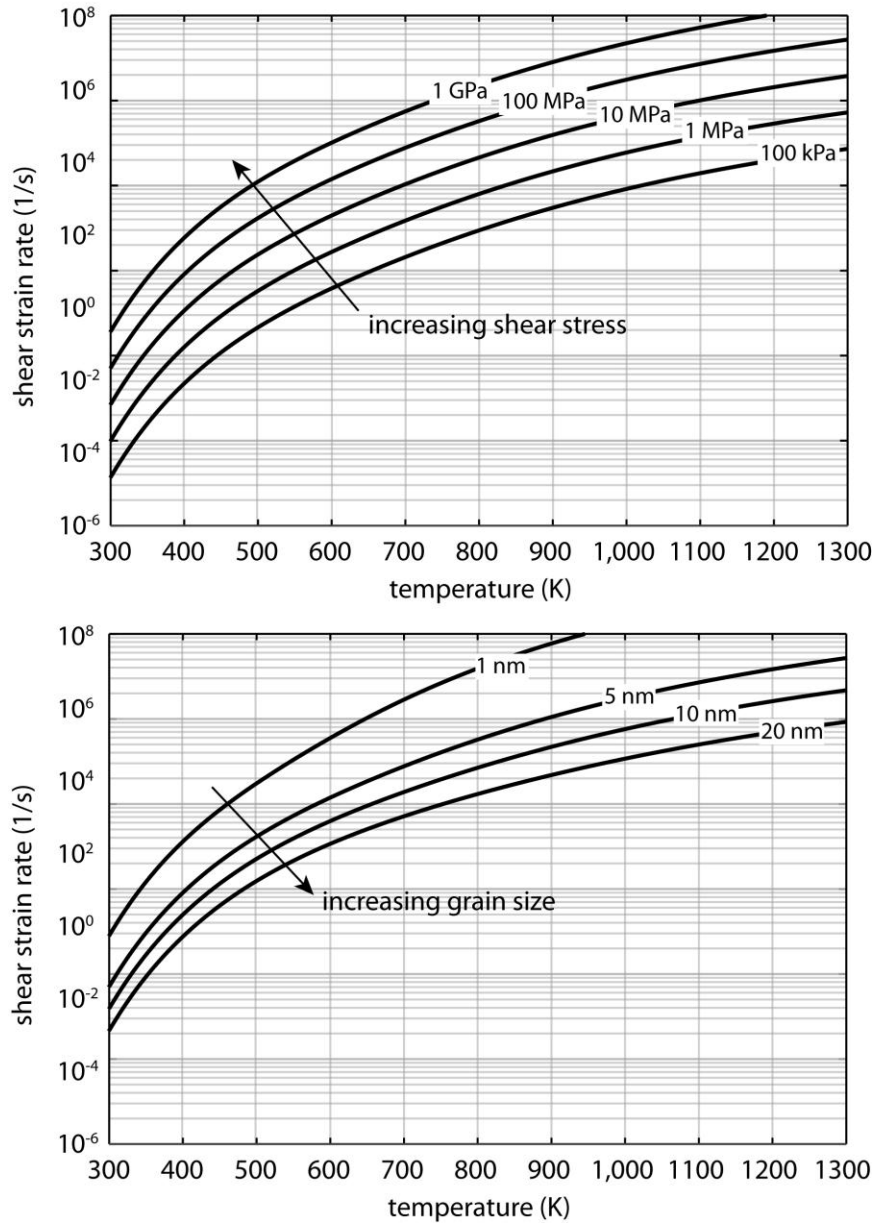


Figure B-1. Plots of strain rate accommodation by grain boundary sliding as a function of temperature for varying shear stress values at a constant grain size of 5 nm, and varying grain size at a constant shear stress of 100 MPa.

Figure B-1 shows the shear strain accommodation rates as a function of temperature for varying shear stress and grain size values, from room temperature to near the melting point of copper (~ 1350 K).

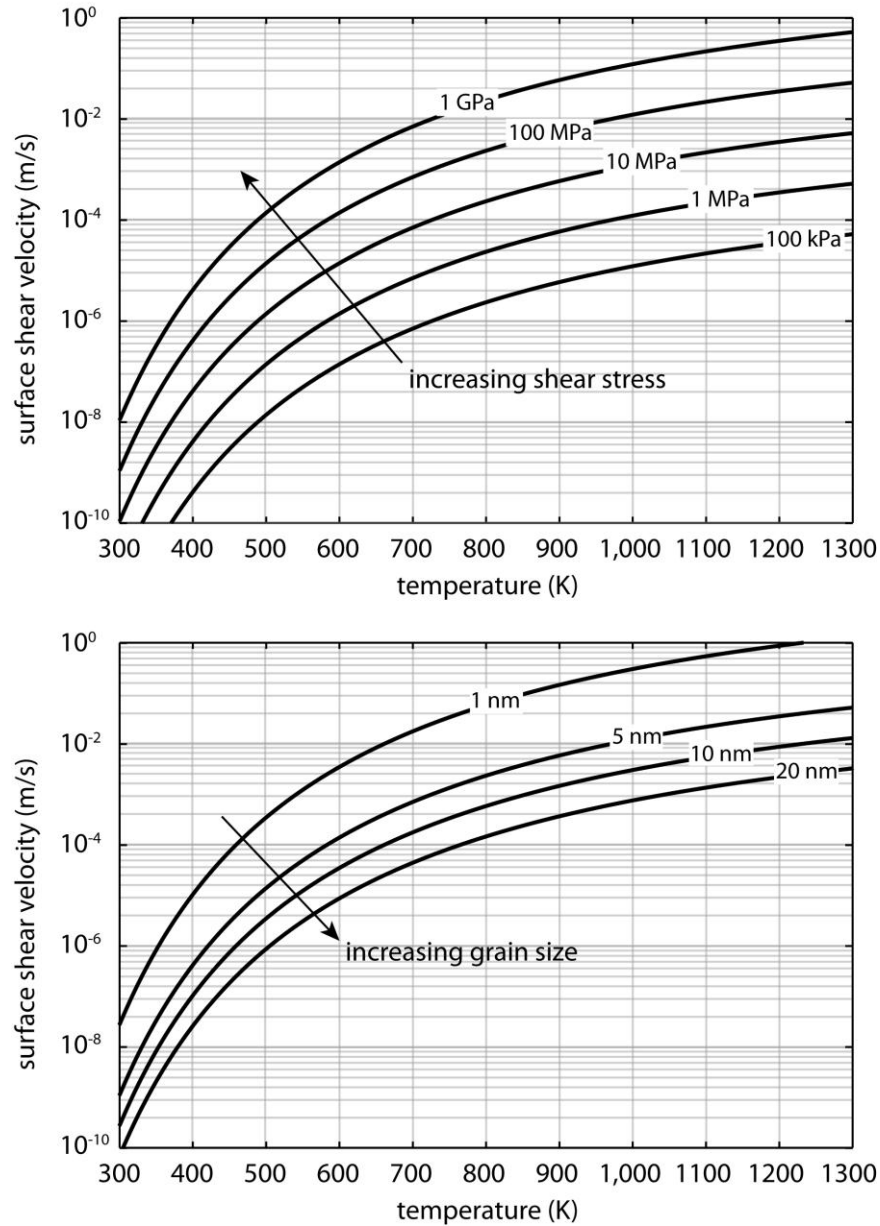


Figure B-2. Plots of the maximum theoretical surface speed that can be accommodated by a 50 nm thick layer of ultrafine grained nanocrystalline copper ($d \sim 5$ nm) by grain boundary sliding for a 100 MPa surface shear stress if the film is treated as a Newtonian fluid with laminar flow.

As described in Chapter 5, it is possible to make an approximate calculation of the maximum interfacial shear speed that can be accommodated by grain boundary sliding for a sliding contact by treating the ultrafine nanocrystalline layer (labeled Zone 1, Figure 5-6) as a

Newtonian fluid with a viscosity calculated from Equations 5-2, which are derived from the constitutive Equation B-3.

The analysis presented based on the model proposed by Raj and Ashby [91], although by no means exhaustive or experimentally verified, indicates that grain boundary sliding likely accounts for only a negligible part of the bulk plastic deformation at the surface of a sliding metal contact at the sliding speeds and contact pressures characteristic of the experimental systems discussed in this manuscript.

APPENDIX C
DESCRIBING A METAL FIBER SLIDING ELECTRICAL
CONTACT AS A PERIODICALLY DISCHARGING CAPACITOR

An order of magnitude comparison of the drift velocity of electrical current in a metal conductor, the rate of change in the location of contacting asperities as a function of sliding speed, and the localized increase in electrical resistance due to constriction of current through asperities at the interface of a macroscopic metal sliding electrical contact, such as a metal fiber brush on a slip-ring [14, 43, 64, 82], provides insightful discussion and is the theme of this appendix.

Although individual charge carriers exhibit Brownian motion at the Fermi speed in the solid ($v_F \sim 1.6 \times 10^6$ m/s in copper which is about 0.5% the speed of light in a vacuum) the ensemble average *drift velocity* of electrons in a conductor (v_d) is effectively the rate of diffusion of charge carriers as a response to an externally applied driving potential bias (a voltage). The drift velocity in a metal conductor is then a function of the volumetric density of charge carriers in the conductor (a material property, n_q in C/m^3) and the current density in the conductor (J , the current in amps divided by the cross-sectional area of the conductor in m^2).

$$v_d = \frac{J}{n_q} \quad (C-1)$$

For a copper wire ($n_q \sim 1.4 \times 10^{10}$ C/m³) carrying a DC electrical current of $I \sim 30$ mA in a 100 μ m diameter fiber cross-sectional area ($J \cong 380 A/cm^2$), the drift velocity is calculated to be $v_d \sim 280 \mu$ m/s. As an order of magnitude approximation based on the concept covered in Chapter 2 that the real area of contact is comprised of a handful of asperities the sum of which is approximately equal to 0.01% of the apparent area of contact, the current density (J) and consequently the drift velocity through the real area of contact will be proportionately higher. For a real area of contact $A_{real} \cong 0.0001 \cdot A_{nom} \cong 0.8 \mu m^2$ ($J \cong 3.8 MA/cm^2$) the drift velocity $v_d \sim 2.8$ m/s.

Assuming that each fiber in contact carries a fraction of the metal brush mechanical and electrical load through an approximately circular asperity contact area equal to $0.8 \mu\text{m}^2$, a conservative estimate for a multi-fiber brush, and that the brush is sliding on a relatively rough slip-ring, then the location where this asperity contact exists on the surface of a given metal fiber will continue to change as the fiber orientation changes and the slip-ring topography evolves. For simplicity it is assumed that the asperity contact is circular, so that a $0.8 \mu\text{m}^2$ area corresponds to a contact diameter of $2a \sim 1 \mu\text{m}$. Then the time it takes for an asperity to transition through a contact event (τ) can be estimated as the time it takes for the brush to translate the length of the contact diameter, Equation C-2.

$$\tau = \frac{2a}{v} \quad (\text{C-2})$$

In this equation v is the sliding speed of the brush. For a sliding speed of 1 m/s the time required to transition through a single asperity contact event is $\tau \sim 1 \mu\text{s}$, giving bulk electrons in the metal fiber relatively far from the surface only time to move toward the asperity contact by a distance of $v_d \cdot \tau \sim (280 \mu\text{m} / \text{s}) \cdot (1 \mu\text{s}) = 2.8 \text{ \AA}$. As a limiting case, an electron that happens to lie on the surface near the contact will move a distance $v_d \cdot \tau \sim (2.8 \text{ m} / \text{s}) \cdot (1 \mu\text{s}) = 2.8 \mu\text{m}$.

Timsit (pages 2-4 in Slade [42]) describes how constriction of current flow between two conductors in contact at a circular asperity may be analytically modeled, to a first approximation, following the work of Smythe [96] (pages 89-91). Figure C-1 presents a visual aid of this conceptual model. The mathematical calculation of the steady-state surfaces of equipotential approaching an asperity was based on the contact between two semi-infinite half-spaces where conduction. Given the relative magnitude difference between an asperity contact diameter and a metal fiber diameter ($\sim 1:1000$) and typical average roughness values below $R_a \sim 1 \mu\text{m}$, this

model is arguably a sufficiently accurate representation of the electric field distortion near an asperity contact, and consequently a useful reference in estimating the velocity gradient of charge carriers as a function of their proximity to the asperity contact.

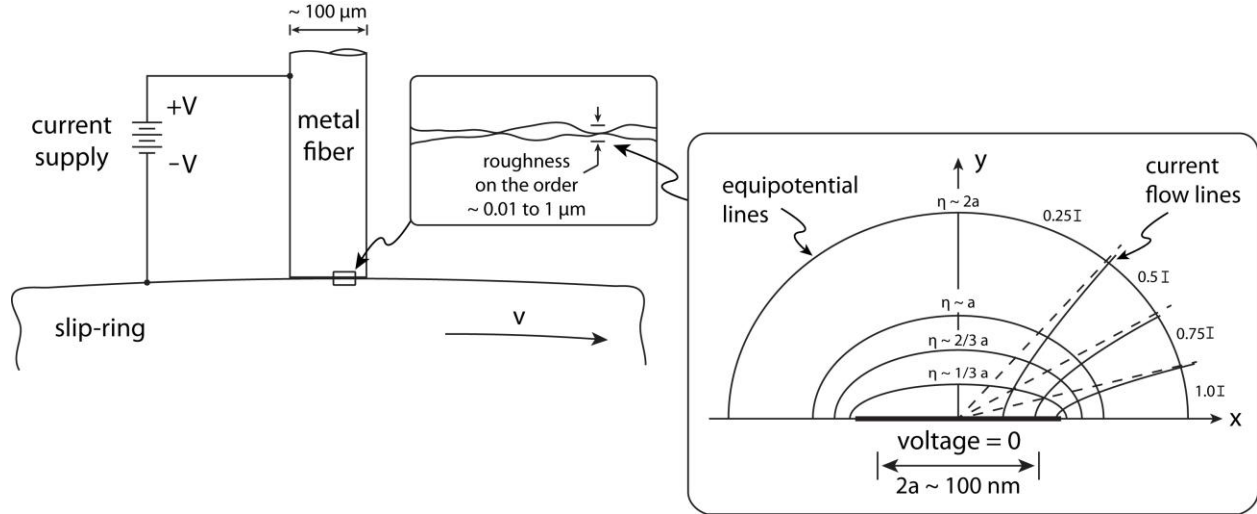


Figure C-1. Visual representation of a metal fiber sliding electrical contact at increasingly magnified scale; the diagram to the right shows the 2D representation of equipotential lines as a function of the distance from asperity contact area assuming an axisymmetric circular contact geometry adapted from Holm [10] and Smythe [96].

Following the mathematical derivation provided by Smythe [96] (pages 89-91) the lines of current flow will orthogonally traverse ellipses of increasing eccentricity with increasing proximity to the asperity contact boundary, as described by Equation C-3 (a simplified version of Smythe's results, presented by Holm on pages 15-17 in [10]).

$$\frac{x^2}{a^2 + \eta^2} + \frac{y^2}{\eta^2} = 1 \quad (\text{C-3})$$

Following the argument that the drift velocity is proportional to the conduction area, the drift velocity near a constriction increases as a function of the surface area of the ellipsoid generated by revolving the equipotential lines (forming concentric oblate spheroids radiating from the constriction). The surface area of the oblate spheroids (A_{os}) is expressed as Equation C-

5 from Fogiel [97], where η is the radial distance from the center of the circular area of the asperity contact.

$$A_{os} = 2\pi(a^2 + \eta^2) + \pi \frac{\eta^2}{\varepsilon} \cdot \ln\left(\frac{1+\varepsilon}{1-\varepsilon}\right) , \quad \varepsilon = \sqrt{1 - \left(\frac{\eta^2}{a^2 + \eta^2}\right)} \quad (C-4)$$

Then the current density is calculated as a function of the area expressed by Equation C-4, and the drift velocity is calculated using Equation C-1, both as a function of radial distance from the center of the constriction; the results are presented in Figure C-2.

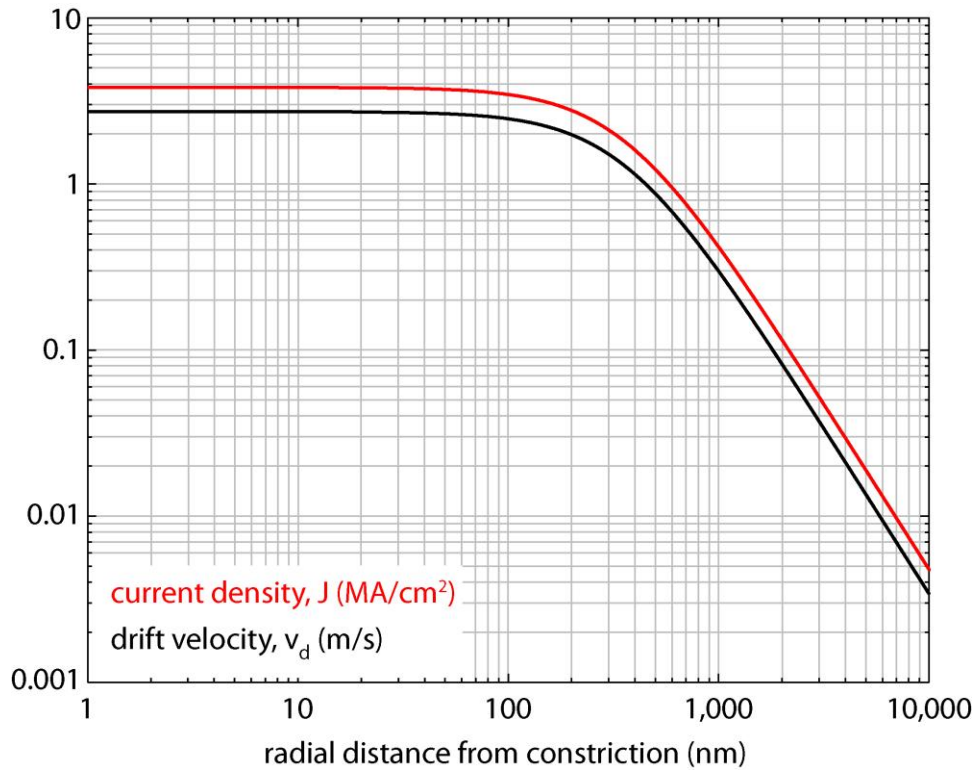


Figure C-2. Drift velocity as a function of radial distance from the center of a circular asperity contact area for a contact diameter $2a \sim 1 \mu\text{m}$ and a current of $I \sim 30 \text{ mA}$.

Continuing the example, for a circular asperity with contact diameter $2a \sim 1 \mu\text{m}$, charge carriers at a distance of about $5 \mu\text{m}$ or greater from the constriction will only move a small fraction of the distance toward the asperity contact over the life of a single contact event ($\sim 1 \mu\text{s}$). Moreover, the role of film resistance was neglected from this analysis. Film resistance causes a

barrier to conduction across the asperity contact, enhancing the build-up of charge on the fiber surface and producing a more even distribution of charge along the surface of the fiber and slip-ring. This analysis suggests that charge carriers tend to move relatively slowly toward the sliding interface of a metal fiber such that the time averaged effect of the varying location of asperity contact events may result in a charge distribution on the surface of a typical 100 μm diameter metal fiber similar to a flat plate capacitor. That is, the nominally flat end of a metal fiber sliding on a metal slip-ring may be described as a parallel plate capacitor with localized discharges through relatively short-lived asperity contact events.

This analysis is important when considering the enhanced oxidation of nominally flat sliding electrical contacts. A first order analysis was presented showing that the distribution of charge over the nominally flat surface area of a metal fiber brush may be a function of sliding speed, current density, and contact force (area of contact). For a sliding contact where sliding speed is low or contact force/current density are high it is hypothesized that the distribution of charge on the surface of the moving contact will be able to adjust to the change in location of an asperity contact in the time duration of a contact event, causing a more dense electric field localized about the contacting asperity. In contrast, for a sliding contact at high sliding speed and low contact force/current density the charge distribution may not adjust to the changing location of an asperity contact, creating a more even distribution of charge on the surface of the fiber. The enhancement of oxidation as a result of an external voltage across a contact not only hinges on the build-up of charge on the surface of the sliding contact, enhancing/inhibiting oxidation by affecting the rate of ion diffusion through a surface film or oxide, but it also depends on the availability of ions on the surface near the location of charge buildup. A practical conclusion from this analysis is that a rougher surface finish (separation of the sliding surfaces

away from the location of contact and thus reducing the capacitance of the fiber surface not in contact with the slip-ring), the addition of an insulating medium to minimize charge distribution away from the asperity contact (such as HFE, again resulting in a reduction in capacitance of the surfaces away from contact by increasing the permittivity of the medium between the surfaces), and the absence of surface films that prevent high drift velocity conduction through asperity contacts should all minimize the effect of enhanced oxidation by concentrating the electric field across a sliding contact at the location of asperity contact where, avoiding boundary lubrication by a chemically reactive species such as water, there will be an absence of ions to drive into the bulk and cause enhanced oxidation. Simple experiments and computer simulations should be performed to test the validity of this hypothesis. Although other factors should be considered, this analysis indicates that a rolling element bearing sliding electrical contact with an electrically insulating thin film of lubrication (such as HFE) may be capable of high current density, low wear operation.

LIST OF REFERENCES

- [1] M. Faraday, *The Bakerian Lecture: Experimental Researches in Electricity. Second Series*, Philosophical Transactions of the Royal Society of London 122 (1832) 163-194.
- [2] D. Kuhlmann-Wilsdorf, *Metal Fiber Brushes in Electrical Contacts Principles and Applications*, ed. P. G. Slade, Marcel Dekker, New York, 1999, p.943 - 1017.
- [3] I. R. McNab, *Recent advances in electrical current collection*, Wear 59 (1980) 259-276.
- [4] P. W. Kendall, I. R. McNab, G. A. Wilkin, *Recent developments in current collection*, Physics in Technology 6 (1975) 117.
- [5] W. H. Bragg, *An Introduction to Crystal Analysis*, Bell, London (1928) 64.
- [6] D. Ramadanoff, S. W. Glass, *High-altitude brush problem*, Tans. Am. Inst. Electr. Eng. 63 (1944) 825.
- [7] R. H. Savage, *Graphite lubrication*, Journal of Applied Physics 19 (1948) 1-10.
- [8] R. F. Deacon, J. F. Goodman, *Lubrication by Lamellar Solids*, Proceedings of the Royal Society of London. Series A, Mathematical and Physical Sciences 243 (1958) 464-482.
- [9] E. I. Shobert, *Sliding Electrical Contacts (Graphitic Type Lubrication)* in Electrical Contacts Principles and Applications, ed. P. G. Slade, Marcel Dekker, New York, 1999, p.839-872.
- [10] R. Holm, *Electric Contacts: Theory and Application, 4th Ed.*, Springer-Verlag, New York, 1967.
- [11] L. Boyer, S. Noel, J. P. Chabrierie, *Electrochemically activated wear of metal fibre brushes*, Wear 116 (1987) 43-57.
- [12] S. Dillich, D. Kuhlmann-Wilsdorf, *Effects of Surface Films on the Performance of Silver-Graphite (75 wt% Ag, 25 wt% C) Electric Brushes*, Components, Hybrids, and Manufacturing Technology, IEEE Transactions on 3 (1980) 37-41.
- [13] I. R. McNab, J. L. Johnson, *High-Current Brushes, Part III: Performance Evaluation for Sintered Silver-Graphite Grades*, IEEE Transactions on Components, Hybrids, and Manufacturing Technology CHMT-2 (1979) 84 - 89.
- [14] P. Reichner, *High Current Tests of Metal Fiber Brushes*, IEEE Transactions on Components, Hybrids, and Manufacturing Technology CHMT-4 (1981) 2 - 4.
- [15] J. A. Bares, N. Argibay, N. Mauntler, G. J. Dudder, S. S. Perry, G. R. Bourne, W. G. Sawyer, *High current density copper-on-copper sliding electrical contacts at low sliding velocities*, Wear 267 (2009) 417-424.

- [16] X. Deng, A. Verdaguer, T. Herranz, C. Weis, H. Bluhm, M. Salmeron, *Surface Chemistry of Cu in the Presence of CO₂ and H₂O*, *Langmuir* 24 (2008) 9474-9478.
- [17] J. A. Bares, *Lubrication of High Current Density Metallic Sliding Electrical Contacts*, Ph.D. Thesis, University of Florida (2009).
- [18] J. L. Johnson, J. Schreurs, *High-Current Brushes, Part VIII: Effect of Electrical Load*, *Wear* 78 (1982) 219 - 232.
- [19] D. Paulmier, H. Zaidi, H. Salliot, E. Hounkponou, *Effects of electrical current and its polarity on the surfaces of copper and carbon in contact*, *Surface Science* 251-252 (1991) 769-772.
- [20] N. Cabrera, N. F. Mott, *Theory of the Oxidation of Metals*, *Rep. Prog. Physics* 12 (1949) 163-184.
- [21] N. P. Suh, *An overview of the delamination theory of wear*, *Wear* 44 (1977) 1-16.
- [22] J. R. Fleming, N. P. Suh, *Mechanics of crack propagation in delamination wear*, *Wear* 44 (1977) 39-56.
- [23] S. Jahanmir, N. P. Suh, *Mechanics of subsurface void nucleation in delamination wear*, *Wear* 44 (1977) 17-38.
- [24] N. P. Suh, *The delamination theory of wear*, *Wear* 25 (1973) 111-124.
- [25] H. Shen, S. E. Podlaseck, I. R. Kramer, *Effect of vacuum on the fatigue life of aluminum*, *Acta Metallurgica* 14 (1966) 341-346.
- [26] W. A. Wood, S. M. Cousland, K. R. Sargant, *Systematic microstructural changes peculiar to fatigue deformation*, *Acta Metallurgica* 11 (1963) 643-652.
- [27] P. V. Nazarenko, Y. I. Korolenko, *Effect of oxide films on the variation in dislocation structures and friction forces*, *Fiziko-Khimicheskaya Mekhanika Materialov* 6 (1970) 75-77.
- [28] D. Duquette, M. Gell, *The effect of environment on the mechanism of Stage I fatigue fracture*, *Metallurgical and Materials Transactions B* 2 (1971) 1325-1331.
- [29] D. H. Buckley, *Surface Effects in Adhesion, Friction, Wear, and Lubrication*, *Tribology Series 5*, Elsevier, 1981.
- [30] L. Nicola, E. Van der Giessen, A. Needleman, *Discrete dislocation analysis of size effects in thin films*, *Journal of Applied Physics* 93 (2003) 5920-5928.

- [31] L. Nicola, Y. Xiang, J. J. Vlassak, E. Van der Giessen, A. Needleman, *Plastic deformation of freestanding thin films: Experiments and modeling*, Journal of the Mechanics and Physics of Solids 54 (2006) 2089-2110.
- [32] H. Hertz, *Über die Berührung fester elastischer Körper (On Contact Between Elastic Bodies)*, Journal für die reine und angewandte Mathematik 92 (1882) 156-171.
- [33] N. K. Adam, *The Physics and Chemistry of Surfaces*, pg. 232, Oxford University Press, 1938.
- [34] J. F. Archard, W. Hirst, *An Examination of a Mild Wear Process*, Proceedings of the Royal Society of London. Series A, Mathematical and Physical Sciences 238 (1957) 515-528.
- [35] J. F. Archard, *Elastic Deformation and the Laws of Friction*, Proceedings of the Royal Society of London. Series A, Mathematical and Physical Sciences 243 (1957) 190-205.
- [36] F. P. Bowden, D. Tabor, *The Area of Contact between Stationary and between Moving Surfaces*, Proceedings of the Royal Society of London. Series A, Mathematical and Physical Sciences 169 (1939) 391-413.
- [37] J. Dyson, W. Hirst, *The True Contact Area Between Solids*, Proceedings of the Physical Society. Section B 67 (1954) 309.
- [38] J. A. Greenwood, J. B. P. Williamson, *Contact of Nominally Flat Surfaces*, Proceedings of the Royal Society of London. Series A, Mathematical and Physical Sciences 295 (1966) 300-319.
- [39] D. Tabor, *The hardness of metals*, Clarendon Press, Oxford, 1951.
- [40] L. Binder, *Elektrotech. u. Maschinenb.*, 38 (1912) 781-788.
- [41] R. S. Timsit, *Electrical Contact Resistance* in Electrical Contacts Principles and Applications, ed. P. G. Slade, Marcel Dekker, New York, 1999, p.943 - 1017.
- [42] P. G. Slade (ed.), *Electrical Contacts: Principles and Applications*, Marcel Dekker, New York, 1999.
- [43] N. Argibay, J. A. Bares, W. G. Sawyer, *Asymmetric wear behavior of self-mated copper fiber brush and slip-ring sliding electrical contacts in a humid carbon dioxide environment*, Wear 268 (2009) 455-463.
- [44] J. A. Greenwood, *Constriction resistance and the real area of contact*, British Journal of Applied Physics 17 (1966) 1621.
- [45] R. Holm, *Wiss. Veroff*, Siemens-Werken 7 (1929) 217-258.

- [46] J. S. Anderson, N. N. Greenwood, *The Semiconducting Properties of Cuprous Oxide*, Proceedings of the Royal Society of London. Series A, Mathematical and Physical Sciences 215 (1952) 353-370.
- [47] N. F. Mott, *The theory of the formation of protective oxide films on metals. -III*, Transactions of the Faraday Society 43 (1947) 429-434.
- [48] F. W. Young Jr, J. V. Cathcart, A. T. Gwathmey, *The rates of oxidation of several faces of a single crystal of copper as determined with elliptically polarized light*, Acta Metallurgica 4 (1956) 145-152.
- [49] M. Antler, *Sliding wear of metallic contacts*, Electrical Contacts 1980: Proc. 26th Holm Conference on Electrical Contacts (1980) 3-24.
- [50] G. W. Stachowiak, A. W. Batchelor, *Engineering Tribology*, Elsevier Butterworth-Heinemann, Oxford, UK, 2005.
- [51] W. Hartweck, H. J. Grabke, *Effect of adsorbed atoms on the adhesion of iron surfaces*, Surface Science 89 (1979) 174-181.
- [52] W. H. Lupton, P. Reichner, *Ultra-high speed fiber brush design and tests*, Wear 78 (1982) 139-149.
- [53] P. Reichner, *Metallic Brushes for Extreme High Current Applications*, IEEE Transactions on Components, Hybrids, and Manufacturing Technology CHMT-3 (1980) 21 - 25.
- [54] J. F. Archard, *Single Contacts and Multiple Encounters*, Journal of Applied Physics 32 (1961) 1420-1425.
- [55] E. I. Shobert, *Carbon Brushes: The Physics and Chemistry of Sliding Contacts*, Chemical Publishing Company, Inc., New York, 1965.
- [56] N. Cabrera, N. F. Mott, *Theory of the Oxidation of Metals*, Rep. Prog. Physics 12 (1947) 163-184.
- [57] J. Bardeen, W. H. Brattain, W. Shockley, *Investigation of Oxidation of Copper by Use of Radioactive Cu Tracer*, The Journal of Chemical Physics 14 (1946) 714-721.
- [58] N. P. Suh, *The delamination theory of wear*, Wear 25 (1973) 111-124.
- [59] J. R. Fleming, N. P. Suh, *The relationship between crack propagation rates and wear rates*, Wear 44 (1977) 57-64.
- [60] S. Jahanmir, N. P. Suh, E. P. Abrahamson, *Microscopic observations of the wear sheet formation by delamination*, Wear 28 (1974) 235-249.

- [61] K. L. Johnson, *Contact Mechanics*, Cambridge University Press, Cambridge, UK, 1985.
- [62] P. V. Nazarenko, Y. I. Korolenko, *Effect of oxide films on the variation in dislocation structures and friction forces*, *Materials Science* 6 (1973) 209-212.
- [63] L. Brown, D. Kuhlmann-Wilsdorf, W. Jesser, *Testing and Evaluation of Metal Fiber Brush Operation on Slip Rings and Commutators*, *Components and Packaging Technologies*, *IEEE Transactions on* 31 (2008) 485-494.
- [64] N. Argibay, J. A. Bares, J. H. Keith, G. R. Bourne, W. G. Sawyer, *Copper-beryllium metal fiber brushes in high current density sliding electrical contacts*, *Wear* 268 (2010) 1230-1236.
- [65] D. L. Burris, W. G. Sawyer, *Addressing Practical Challenges of Low Friction Coefficient Measurements*, *Tribology Letters* 35 (2009) 17-23.
- [66] O. Mollenhauer, S. I. U. Ahmed, F. Spiller, H. Haefke, *High-precision positioning and measurement systems for microtribotesting*, *Tribotest* 12 (2006) 189-199.
- [67] W. A. Bonin, *Multi-dimensional capacitive transducer*, (1997) patent no. 579,996.
- [68] P. L. Dickrell, S. B. Sinnott, D. W. Hahn, N. R. Raravikar, L. S. Schadler, P. M. Ajayan, W. G. Sawyer, *Frictional anisotropy of oriented carbon nanotube surfaces*, *Tribology Letters* 18 (2005) 59-62.
- [69] H. Liu, B. Bhushan, *Adhesion and friction studies of microelectromechanical systems/nanoelectromechanical systems materials using a novel microtriboapparatus*, *Papers from the 49th International Symposium of the American Vacuum Society* (2003).
- [70] A. C. Rennie, P. L. Dickrell, W. G. Sawyer, *Friction coefficient of soft contact lenses: measurements and modeling*, *Tribology Letters* 18 (2005) 499-504.
- [71] D. Burris, W. Sawyer, *Measurement Uncertainties in Wear Rates*, *Tribology Letters* 36 (2009) 81-87.
- [72] T. L. Schmitz, J. E. Action, J. C. Ziegert, W. G. Sawyer, *The difficulty of measuring low friction: Uncertainty analysis for friction coefficient measurements*, *Journal of Tribology-Transactions of the Asme* 127 (2005) 673-678.
- [73] K. L. Chavez, D. W. Hess, *A Novel Method of Etching Copper Oxide Using Acetic Acid*, *Journal of The Electrochemical Society* 148 (2001) G640-G643.
- [74] D. DeNardis, D. Rosales-Yeomans, L. Borucki, A. Philipossian, *Characterization of copper-hydrogen peroxide film growth kinetics*, *Thin Solid Films* 513 (2006) 311-318.

- [75] M. Pérez Sánchez, M. Barrera, S. González, R. M. Souto, R. C. Salvarezza, A. J. Arvia, *Electrochemical behaviour of copper in aqueous moderate alkaline media, containing sodium carbonate and bicarbonate, and sodium perchlorate*, *Electrochimica Acta* 35 (1990) 1337-1343.
- [76] S. V. Prasad, J. R. Michael, T. R. Christenson, *EBS D studies on wear-induced subsurface regions in LIGA nickel*, *Scripta Materialia* 48 (2003) 255-260.
- [77] M. Pérez Sánchez, R. M. Souto, M. Barrera, S. González, R. C. Salvarezza, A. J. Arvia, *A mechanistic approach to the electroformation of anodic layers on copper and their electroreduction in aqueous solutions containing NaHCO₃ and Na₂CO₃*, *Electrochimica Acta* 38 (1993) 703-715.
- [78] M. R. Gennero De Chialvo, J. O. Zerbino, S. L. Marchiano, A. J. Arvia, *Correlation of electrochemical and ellipsometric data in relation to the kinetics and mechanism of Cu₂O electroformation in alkaline solutions*, *Journal of Applied Electrochemistry* 16 (1986) 517-526.
- [79] J. Takadom, *Tribological behaviour of alumina sliding on several kinds of materials*, *Wear* 170 (1993) 285-290.
- [80] K. Hiratsuka, A. Enomoto, T. Sasada, *Friction and wear of Al₂O₃, ZrO₂ and SiO₂ rubbed against pure metals*, *Wear* 153 (1992) 361-373.
- [81] M. Barquins, M. Kennel, R. Courtel, *Comportement de monocristaux de cuivre sous l'action de contact d'un frotteur hemispherique*, *Wear* 11 (1968) 87-110.
- [82] L. Boyer, J. P. Chabrierie, J. Saint-Michel, *Low wear metallic fibre brushes*, *Wear* 78 (1982) 59-68.
- [83] M. Cocks, *Interaction of Sliding Metal Surfaces*, *Journal of Applied Physics* 33 (1962) 2152-2161.
- [84] S. L. Rice, H. Nowotny, S. F. Wayne, *Characteristics of metallic subsurface zones in sliding and impact wear*, *Wear* 74 (1981) 131-142.
- [85] M. Antler, *Processes of metal transfer and wear*, *Wear* 7 (1964) 181-203.
- [86] F. P. Bowden, A. J. W. Moore, D. Tabor, *The Ploughing and Adhesion of Sliding Metals*, *Journal of Applied Physics* 14 (1943) 80-91.
- [87] F. P. Bowden, G. W. Rowe, *The Adhesion of Clean Metals*, *Proceedings of the Royal Society of London. Series A, Mathematical and Physical Sciences* 233 (1956) 429-442.
- [88] E. I. Dobson, *The effect of humidity on brush operation*, *Electric J.* 32:527 (1954).

- [89] M. Kerridge, J. K. Lancaster, *The Stages in a Process of Severe Metallic Wear*, Proceedings of the Royal Society of London. Series A, Mathematical and Physical Sciences 236 (1956) 250-264.
- [90] S. V. Prasad, C. C. Battaile, P. G. Kotula, *Friction transitions in nanocrystalline nickel*, Scripta Materialia 64 (2010) 729-732.
- [91] R. Raj, M. Ashby, *On grain boundary sliding and diffusional creep*, Metallurgical and Materials Transactions B 2 (1971) 1113-1127.
- [92] W. Dickenscheid, R. Birringer, H. Gleiter, O. Kanert, B. Michel, B. Günther, *Investigation of self-diffusion in nanocrystalline copper by NMR*, Solid State Communications 79 (1991) 683-686.
- [93] J. Schiotz, K. W. Jacobsen, *A Maximum in the Strength of Nanocrystalline Copper*, Science 301 (2003) 1357-1359.
- [94] L. Yue, H. Zhang, D. Y. Li, *A closer look at the local responses of twin and grain boundaries in Cu to stress at the nanoscale with possible transition from the P-H to the inverse P-H relation*, Acta Materialia 58 2677-2684.
- [95] A. Bondi, *Van der Waals Volumes and Radii*, The Journal of Physical Chemistry 68 (1964) 441-451.
- [96] W. R. Smythe, *Static and Dynamic Electricity, 3rd Ed.*, Hemisphere Publishing, New York, NY, 1989.
- [97] M. Fogiel, Research, A. Education, *Handbook of mathematical, scientific, and engineering formulas, tables, functions, graphs, transforms*, Research and Education Association, 1992.

BIOGRAPHICAL SKETCH

Nicolas Argibay was born in 1982 in Montevideo, Uruguay. He immigrated to the United States at the age of ten and completed his primary education in 2011 at St. Brendan High School in Miami, Florida. He was accepted at the University of Florida with a full scholarship as a National Hispanic Scholar where he completed dual Bachelor of Science degrees in mechanical and aerospace engineering in 2006. He was then admitted to the graduate program at the University of Florida where he completed Master of Science (2009) and Doctor of Philosophy (2011) degrees in mechanical engineering. He was a researcher at the University of Florida Tribology Laboratory under the supervision of Prof. Dr. W. Gregory Sawyer from 2006 to 2011 where his research focus was on the study of interfaces, particularly the wear and friction behavior of sliding contacts under vapor phase lubrication. As a graduate student he was author and co-author of a number of peer reviewed publications with topics in a broad range of applications, including molybdenum disulfide coatings for cryogenic applications, low friction and wear ultra-high molecular weight polyethylene fibers, high temperature pyrolytic carbon lubrication, and his main research focus: high current density metal sliding electrical contacts. He was also a guest researcher during a three month summer internship in 2008 at the Eidgenössische Technische Hochschule (ETH) in Zurich, Switzerland under the supervision of Prof. Dr. Nicholas D. Spencer, performing research on the use of biologically inspired grafted copolymer brushes as a biocompatible self-healing lubricant.